# Band gap grading of a–SiO$_x$:H and its effect on the performance of thin film solar cells

Mario Rogelio Rodríguez Luna

Delft University of Technology

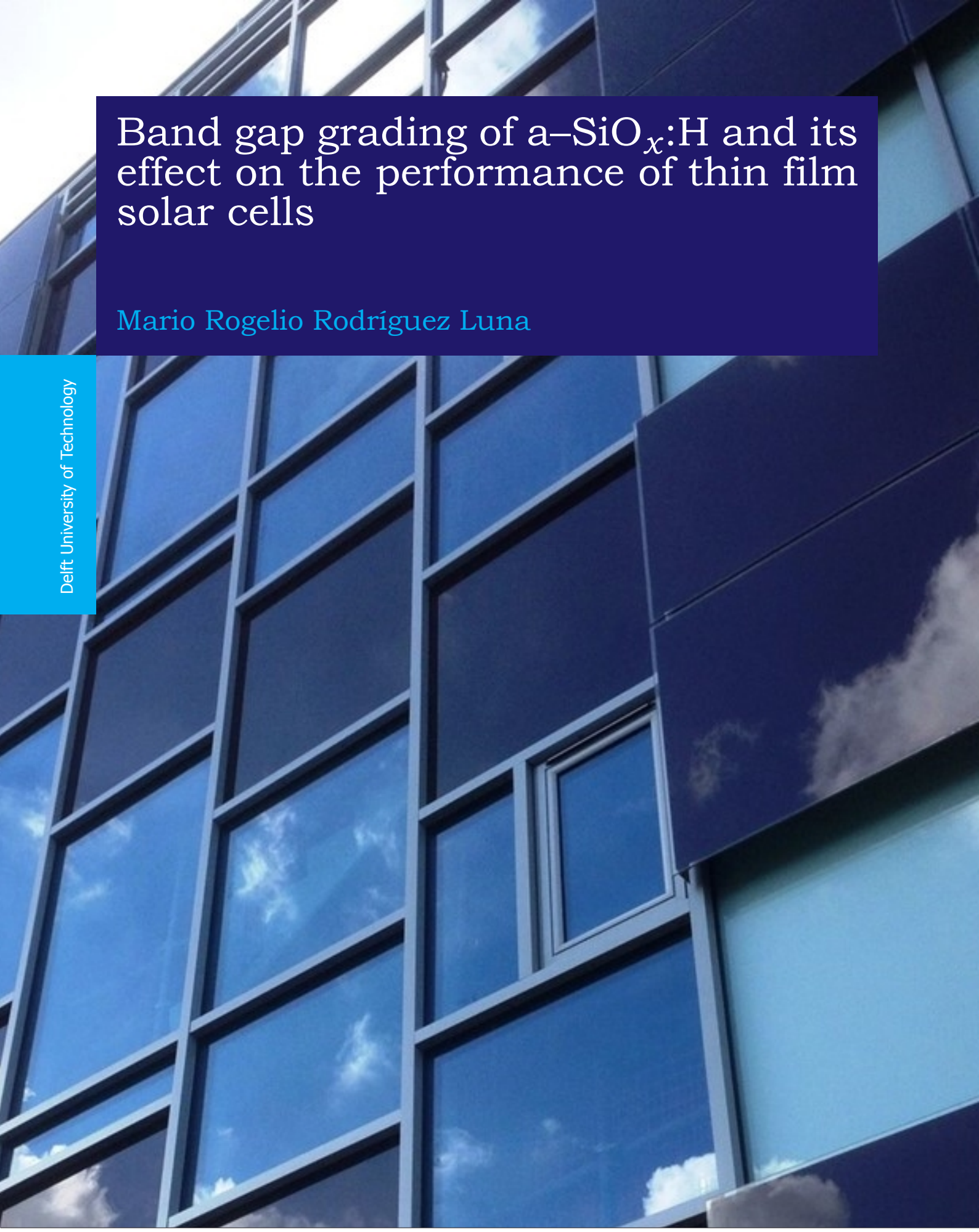

TU Delft Delft University of Technology

Challenge the future

Cover image obtained from http://www.polysolar.co.uk/BIPV-Solutions/facade%20cropped.jpg

# Band gap grading of a–SiO$_x$:H and its effect on the performance of thin film solar cells

by

**Mario Rogelio Rodríguez Luna**

in partial fulfillment of the requirements for the degree of

**Master of Science**

in Sustainable Energy Technology

at the Delft University of Technology, Department of Photovoltaic Material and Devices

to be defended publicly on Wednesday December 20, 2017 at 10:00 AM.

| | | |
|---|---|---|
| Supervisor: | Dr. R. A. C. M. M. van Swaaij | |
| Thesis committee: | Dr. R. A. C. M. M. van Swaaij, | TU Delft |
| | Prof. dr. ir. A. H. M. Smets, | TU Delft |
| | Dr. ir. M. Ghaffarian Niasar, | TU Delft |



TU Delft Delft University of Technology

# Acknowledgements

No man can say to have made himself from scratch. I received during the course of this work a great amount of help and support in many different ways. I wish to acknowledge and be grateful for the people who helped me. Since without them these words could not have been written. I would first like to thank my parents who were always believing in me, and showed me with their efforts that it was only fair to also pull forward to match their support. I would like to thank professor René van Swaaij, who gave me the opportunity to perform my work within the PVMD group; guided me with weekly meetings, and helped me to steer the research in the right direction. I would like to thank Aditya Chaudhary who as a fellow master student and friend, we helped each other during several steps of the experimental phase. Also i want to acknowledge academic counsellor Leonie Boortman for her continued support during my whole master. I want to thank the technicians Stefaan Heirman and Martijn Tijssen who helped me a lot with training to use the equipment and many valuable knowledge regarding measurement and deposition. It feels to me also important to thank my dear friend Alvaro Martin Mazorra who was consistently there at times when the solitude a foreign student experiences, can make it harder to look at the big picture. I want to give my thanks as well to the mexican national council of science and technology and mexican secretary of energy (CONACYT-SENER) for awarding me with the scholarship i relied on during my studies. Finally I would like to thank the thesis defense committee: Arno Smets; Mohamad Ghaffarian and once again René van Swaaij for their willingness to grade this thesis.

*Mario Rogelio Rodríguez Luna*
*Delft, December 2017*

# Abstract

Solar cells are showing significant promise to become the solution for the growing energy needs of our world. However for this to happen, new disruptive technologies with high efficiency and low cost are needed in the market. One possibility comes from multijunction thin film solar cells based on a-Si alloys and nc-Si. For this purpose a–$SiO_x$:H is an interesting material since it can have $V_{OC}$ values above 1 V and FF above 0.7. However when paired in a tandem structure with a material of an advantageous bandgap, like nc-Si:H. The performance of the tandem solar is limited in output current by the a–$SiO_x$:H layer.

Research to increase $J_{SC}$ by increasing thickness of the absorber layer show it is not practical to increase the thickness of i-a–$SiO_x$:H above 250 nm. Spillover knowledge from other thin film solar cells (GaAs, a-$SiGe_x$ and CIGS), showed bandgap grading was able to increase performance of the electrical parameters. Grading in a solar cell means that in one of the layers a material property is varied continuously in concentration in order to achieve a different performance.

Our aim was to experiment with bandgap grading in the absorber layer of a–$SiO_x$:H solar cells, to try to achieve a higher $J_{SC}$ while still retaining the high $V_{OC}$ ×FF product. Test layers were deposited at different $CO_2/SiH_4$ ratios to determine the dependence of the bandgap ($E_{04}$) and the deposition rate on the $CO_2/SiH_4$ ratio. With the experimental data and fitted polynomial equations a method was devised to vary continuously the bandgap in a step wise manner. Using this grading method, experiments were designed where the intrinsic a–$SiO_x$:H layer of a total length of 200 nm was subdivided in 3 graded bandgap regions. The first graded region named p-i started from the end of the p-layer with a high bandgap (2.1 eV). Decreasing the bandgap over a certain length until reaching a region with no added Oxygen with a low bandgap (1.96 eV.) From here the central i region started, maintaining a constant bandgap for a certain length until the bandgap starts increasing again. This marks the 3rd region called i-n, where the bandgap continues to increase over a certain width until reaching 2.1 eV at the beginning of the n-layer.

Graded experimental cells results showed that it was beneficial to have a small graded region width in the p-i and i-n region (10-30 nm). Since with this grading length $J_{SC}$ could be increased significantly (8% increase) from reference cell values without grading performed. However a small compromise in a drop of $V_{OC}$ and FF values around (1-2%) was observed at the same time from reference cell values. The gains in $J_{SC}$ are bigger than the loss of $V_{OC}$ ×FF product and result in a relative efficiency gain of (4-5%) from reference cell. This technique paired with other cutting edge techniques to increase photocurrent can lead to a new record for an a–$SiO_x$:H thin film solar cell. Or it can lead to better current matching in tandem or triple junction solar cells.

*Mario Rogelio Rodríguez Luna*
*Delft, December 2017*

# Contents

**List of Figures** xi

**List of Tables** xv

**1 Introduction** 1

1.1 The need for Energy . . . 1

1.1.1 The gap of energy consumption . . . 2

1.1.2 How much energy will be needed? . . . 3

1.2 The unsustainable path of Fossil Energy . . . 4

1.2.1 Energy Security and Economy Diversification . . . 4

1.2.2 Pollution due to FF usage . . . 6

1.2.3 Human induced Climate Change . . . 6

1.3 How to overcome the energy challenges? . . . 7

1.3.1 Energy Efficiency in the European Union . . . 7

1.3.2 The Paris COP21 Agreement . . . 8

1.3.3 Green Energy in the INDC . . . 9

1.4 Renewable energy, unexploited potential . . . 9

1.4.1 Solar Energy, how much would be needed? . . . 10

**2 Motivation** 13

2.1 Introduction and basic working principle of a solar cell . . . 13

2.2 Brief History on Solar Photovoltaics . . . 13

2.2.1 Current Photovoltaic Technologies . . . 15

2.3 Overcoming the theoretical limit . . . 17

2.3.1 Multijunction Solar Cells, opportunities and challenges . . . 18

2.4 Motivation and Objective . . . 20

**3 Experimental Setup** **23**

3.1 Introduction . . . 23

3.1.1 Preparation of Samples . . . 23

3.2 Thin Film Deposition Techniques . . . 24

3.2.1 Plasma-Enhanced Chemical Vapour Deposition . . . 24

3.2.2 Physical Vapour Deposition . . . 24

3.3 Characterization of Individual Test Layers . . . 25

3.3.1 Spectroscopic Ellipsometry (SE) . . . 25

3.4 Characterization of experimental solar cells . . . 28

3.4.1 Solar Simulator . . . 28

3.4.2 Current Density (J) and Voltage (V) measurement . . . 29

3.4.3 External Quantum Efficiency (EQE) . . . 31

3.4.4 Data Processing . . . 33

**4 Grading Method** **35**

4.1 Introduction . . . 35

4.2 Deposition rate and bandgap dependance on $CO_2/SIH_4$ ratio . . . 35

4.3 Making of a layer with a graded bandgap . . . 37

**5 Graded Bandgap Solar cells** **41**

5.1 Introduction . . . 41

5.2 Experimental Section . . . 45

5.2.1 Reference a–$SiO_x$:H Solar Cell . . . 45

5.2.2 Experimental Solar Cell description . . . 45

5.3 Results and Discussion . . . 47

5.3.1 Experimental cells varying the i-n region . . . 47

5.3.2 Experimental cells varying the p-i region . . . 51

5.3.3 Overview of electrical performance of all cells . . . 55

5.3.4 Solar-cell yield . . . 56

**6 Conclusions and Recommendations** **59**

**A Appendix A Grading example** **61**

**B Appendix B Electrical Performance** **63**

**C Solar-cell Yield for all Experimental Cell** **65**

**D Appendix D External Quantum efficiency extended plots** **71**

**Bibliography** **77**

# List of Figures


1.1 World Population Distribution in 2017 [1, Table. 1] . . . . . 1

1.2 World Distribution of Primary Energy Consumption [2] . . . . . 2

1.3 2014 consumption of primary energy sources for selected countries [3] . . . . . 3

1.4 Projections of population change by 2050 for selected countries[1] . . . . . 3

1.5 Comparative primary energy source consumption over the past 15 years. [4, p. 4] . . . 4

1.6 Crude oil prices and key geopolitical and economic events [5] . . . . . 5

1.7 Global mean temperature records, since year 1880 by 4 climate study institutions [6] . 7

1.8 2015 estimated finite and renewable planetary energy reserves (TW-years). Total recoverable reserves are shown for the finite resources. Yearly potential is shown for the renewables [7, fig. 2] . . . . . 10

1.9 Total Area required to supply all energy needs of the World in 2030 with Solar Power [8] 11

2.1 The Photovoltaic Effect in a Silicon solar cell [9]. . . . . 14

2.2 Thin film selenium cell demonstrated by Fritts in 1883 [10]. . . . . 14

2.3 Distribution of Market Share for Photovoltaic Technologies [11] . . . . . 16

2.4 Maximum theoretical solar cell efficiency as a function of the material bandgap, using SQL assumptions.[12] . . . . . 17

2.5 Illustration of a 4 junction (W)a-Si:H/(N)a-Si:H/a-SiGex:H/nc-Si:H thin-film silicon solar cell. Tunnel recombination junction (TRJ) includes all doped layers between the two neighboring absorber layers. [13] . . . . . 18

2.6 Performance of a hybrid a-Si:H/polymer tandem solar cell (a) J–V curves of best performing hybrid tandem solar cell (flat) and respective single-junction reference cells. (b) EQE of the flat tandem solar cell. [14] . . . . . 19

2.7 EQEs of (a) tandem (a-SiOx:H/nc-Si:H) and (b) triple (a-SiOx:H/a-Si:H/nc-Si:H) junction solar cells that use a–$SiO_x$:H as the top absorbing solar cell. The number under each EQE curve represent the photocurrent density of the individual layer. [15] . . . . . 20

2.8 (a) External solar cell parameters and (b) EQEs of a-SiOx:H 1J solar cells as a function of i-layer thickness. [15] . . . . . 21

3.1 Schematic diagram of PECVD [16] . . . . . 24

3.2 Multiple reactor system, similar to AMIGO configuration [17, fig. 7] . . . . . 25

3.3 Schematic of a Physical Vapour Evaporation Device by e-beam [18, fig. 4] . . . . . 26

3.4 SE setup . . . 26
3.5 Linear Polarization of light[19] . . . 27
3.6 Elliptical Polarization of light[19] . . . 27
3.7 Absorption coefficients for c–Si; a–Si:H a–$SiO_x$:H (c–Si values obtained from [20]) . . . 28
3.8 Schematic of Angle of Incidence for AM0, AM1, and AM2 [21] . . . 29
3.9 Solar Spectra for space and terrestrial use [22] . . . 30
3.10 AMG1.5 Solar Simulator Spectral Irradiance [23] . . . 30
3.11 Sample of a–$SiO_x$:H thin film cell . . . 31
3.12 In House 30 pin setup . . . 31
3.13 Solar Cell I-V Characteristic Curve [24] . . . 32
3.14 EQE setup . . . 32

4.1 Comparison at 300°C and 200°C of Deposition ratio ($v_{dep}$) vs $CO_2$/$SiH_4$ ratio $r_{CO_2}$ . . . 36
4.2 $CO_2$/$SiH_4$ ratio vs Optical Bandgap $E_{04}$for test series at 200°C and 3W power . . . 37
4.3 Example of designed grading for the intrinsic layer bandgap, using a configuration of 30p-i. 110 mid-i, 60 i-n . . . 38
4.4 Real deposition behaviour using 10nm steps during grading . . . 38

5.1 Structure of a graded bandgap GaAs solar cell $E_{g1}$ =1.73 eV [25] . . . 42
5.2 Simplified energy band-diagram of an a–Si:H p-i-n solar cell with a graded interface layer[26] . . . 42
5.3 Bandgap profiling for the cases of: (a) no profiling, (b) normal profiling, (c) reverse profiling, and (d) double profiling.[27] . . . 42
5.4 Top: V type profile. Middle: U type profile. Bottom: profile design for optimization. Mg1 and Mg2 were varied independently between 1.5 and 1.80 eV in steps of 0.05 eV. [28] 43
5.5 Schematic i-layer band gap profiling of the 'U-shape', 'V-shape' and 'E-shape' structures, without buffer layers. [29] . . . 43
5.6 Plot of the optical band gap profile for the i-a-SiGe:H films, showing three different bandgap profiles. [30] . . . 44
5.7 Schematic diagram of variable i-n region experimental cells, with a fixed length of 30 nm for the p-i region . . . 46
5.8 Schematic diagram of variable p-i region experimental cells. Cells deposited at 200°C had a constant i-n grading width of 40 nm. Cells deposited at 300°C had a constant i-n grading width of 100 nm. . . . 46
5.9 J-V curve for reference cells deposited at 200°C and 300°C. . . . 47
5.10 External quantum efficiency plot for reference cells deposited at 200°C and 300°C. . . . 47

5.11 a, b, c, d. Ordered from left to right and top to bottom, four electrical properties ($V_{OC}$ $J_{SC}$ FF & $\eta\%$) vs i-n region length, keeping the p-i region at a fixed length of 30 nm. Sample cells deposited at 200°C have royal blue symbols. Sample cells deposited at 300°C have light green symbols. . . . . 48

5.12 Comparison of EQE for samples deposited at 200°C. Sharing in common a p-i region grading length of 30 nm; and varying the i-n region length. A larger version of this plot can be found in Fig. D.1 . . . . . 49

5.13 Comparison of EQE for samples deposited at 300°C. Sharing in common a p-i region grading length of 30 nm; and varying the i-n region length. A larger version of this plot can be found in Fig. D.2 . . . . . 49

5.14 a, b, c, d. Ordered from left to right and top to bottom, four electrical properties ($V_{OC}$ $J_{SC}$ FF & $\eta\%$) vs p-i region length. Sample cells deposited at 200°C keeping the i-n region at a fixed length of 40 nm. . . . . 51

5.15 Comparison of EQE for samples deposited at 200°C. Sharing in common a i-n region grading length of 40 nm; and varying the p-i region length. An extended version of this plot can be found in Fig. D.3 . . . . . 52

5.16 a, b, c, d. Ordered from left to right and top to bottom, four electrical properties ($V_{OC}$ $J_{SC}$ FF & $\eta\%$) vs p-i region length. Sample cells deposited at 200°C keeping the i-n region at a fixed length of 40 nm. . . . . 53

5.17 Comparison of EQE for samples deposited at 300°C. Sharing in common a i-n region grading length of 100 nm; and varying the p-i region length. An extended version of this plot can be found in Fig. D.4 . . . . . 54

5.19 30 cell areas performance distribution of $V_{OC}$×FF for reference cell at 200°C. . . . . 56

5.20 30 cell areas performance distribution of $V_{OC}$×FF for the reference cell deposited at 300°C. 56

5.21 The distribution of $V_{OC}$×FF for reference cell at 300°C. . . . . 57

5.22 Performance distribution of $V_{OC}$×FF for highest efficiency cell at 200°C. . . . . 57

5.23 Performance distribution of $V_{OC}$×FF for highest efficiency cell at 300°C. . . . . 57

C.1 Yield of performance for solar cells deposited at 300°C. Part 1) . . . . . 66

C.2 Yield of performance for solar cells deposited at 300°C. Part 2) . . . . . 67

C.3 Yield of performance for solar cells deposited at 200°C. Part 1) . . . . . 68

C.4 Yield of performance for solar cells deposited at 200°C. Part 2) . . . . . 69

D.1 Extended version of comparison of EQE for samples deposited at 200 °C. Sharing in common a p-i region grading length of 30 nm; and varying the i-n region length. . . . 72

D.2 Extended version of comparison of EQE for samples deposited at 300 °C. Sharing in common a p-i region grading length of 30 nm; and varying the i-n region length. . . . 73

D.3 Extended version of comparison of EQE for samples deposited at 200 °C. Sharing in common a i-n region grading length of 40 nm; and varying the p-i region length. . . . 74

D.4 Extended version of comparison of EQE for samples deposited at 200 °C. Sharing in common a i-n region grading length of 100 nm; and varying the p-i region length. . . . 75

D.5 Extended version of comparison of EQE for Reference cells and best performing in terms of highest efficiency experimental cells deposited at 200 °C and 300 °C. . . . . 76

# List of Tables

5.1 Deposition Conditions for the Reference cell . . . . . 45

5.2 External Parameter results for Reference cells . . . . . 47

A.1 Example of Gas flow and deposition time for configuration of 30p-i. 110 mid-i, 60 i-n . 61

B.1 Electrical Performance raw data for samples presented in Fig. 5.18 . . . . . 63

# 1

# Introduction

## 1.1. The need for Energy

Societies need energy in order to enable growth. And as the human population is rapidly increasing in the recent decades, with every new human being each nation has the challenge to increase their energy output. As of 2017 the United Nations Department on Economic and Social Affairs (UN DESA) reports the total human population as being close to 7.6 billion, with projections to increase to 9.8 billion by 2050 and to 11.2 billion by 2100 [1]. The same report also mentions that more than half of human population is located in Asia (4.5 billion of people) with China and India alone having 35% of global population). The contribution of the other continents is summarized in Fig. 1.1.

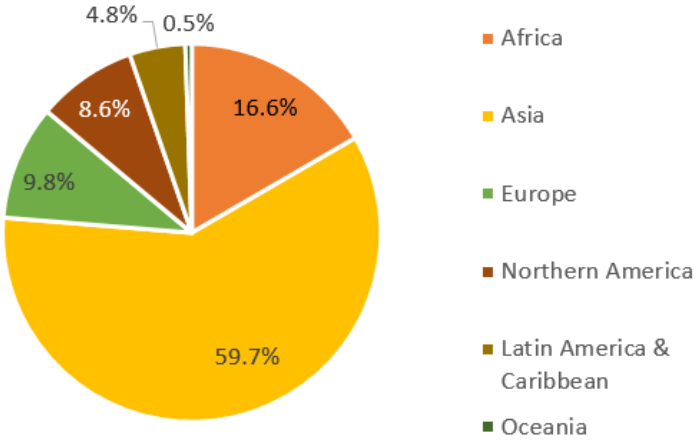


Figure 1.1: World Population Distribution in 2017 [1, Table. 1]

However the distribution of energy around the world differs significantly to how population is distributed. In Fig. 1.2 it can be seen that a big portion, around 21% of the total energy consumption is taken by Northern America, while this region only houses 8.6% of the global population . A similar disparity can be seen when comparing Europe consumption (21.5%) and population (9.8%) percentages.

Both regions share in common that they have nations with highly developed economies. Fig. 1.2 also shows another important fact: Africa, Middle East, Latin America regions while they also have increased their energy consumption since 1965, the amount of this increase is quite small when compared to

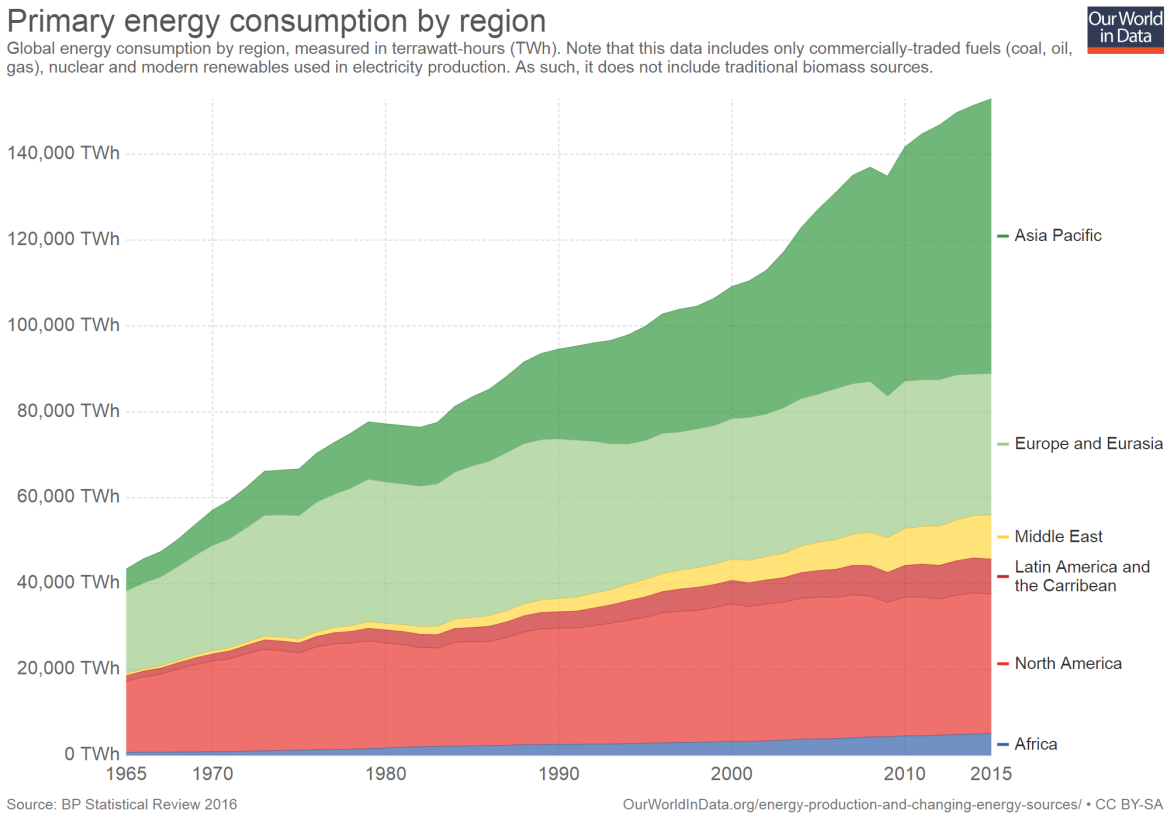


Figure 1.2: World Distribution of Primary Energy Consumption [2]

the other regions. And also these regions hold many countries that strive to get their economies and prosperity to the levels of the already developed nations.

Therefore it cannot be ignored that a certain amount of minimum energy is necessary for an acceptable level of prosperity in a society. Those nations who are improving their economy and living standards will demand more energy as well. The following subsections give a brief explanation of how big is the energy gap for the developing nations; and how much is the total energy needed for a world that is constantly growing.

### 1.1.1. The gap of energy consumption

Before explaining how much is the gap, first it must be established what would be an optimum level of energy consumption, so that prosperity can be attained.

One possible benchmark is the European Union (EU) goal to cut in 20% from projected levels its primary energy consumption by 2020, the target including the reduction is set as 1483 Mtoe (Million Tonnes of Oil Equivalent)[31]. Dividing this number by the projected population for Europe of 513.8 million people for 2020 [32]; it roughly gives an average of 2.88 toe (Tonnes of Oil Equivalent) per capita per year.

When considering the previous value, it could be possible that it represents more energy than what it would be needed for a developing region in the tropics and near the equator; because these regions do not have such a big demand of energy when it comes to residential heating. At the same time the amount of new infrastructure needed to attain the same levels of prosperity, could offset this. However it is beyond the scope of this work to decide how to modify such value. Therefore a consumption of

2.8 toe per capita per year is considered as the threshold of energy use for an acceptable prosperity level.

To understand the energy gap across different economies, Fig. 1.3 is presented. In this figure two types of countries are presented together, starting from the left are the countries predicted to be the biggest contributors to the growth of global population by 2050 (UN DESA [1, p. 14]), most of these countries belong to the African continent; and then continuing from the center with China are the economies predicted to be the 10 biggest by 2050 according to Business Consulting Price Water House Coopers (PwC)[33].

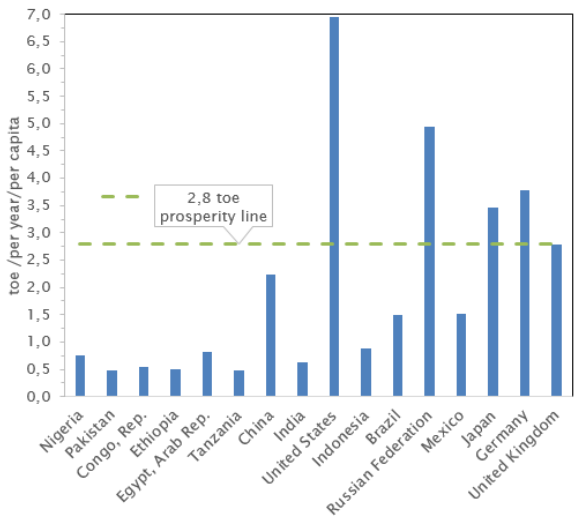


Figure 1.3: 2014 consumption of primary energy sources for selected countries [3]

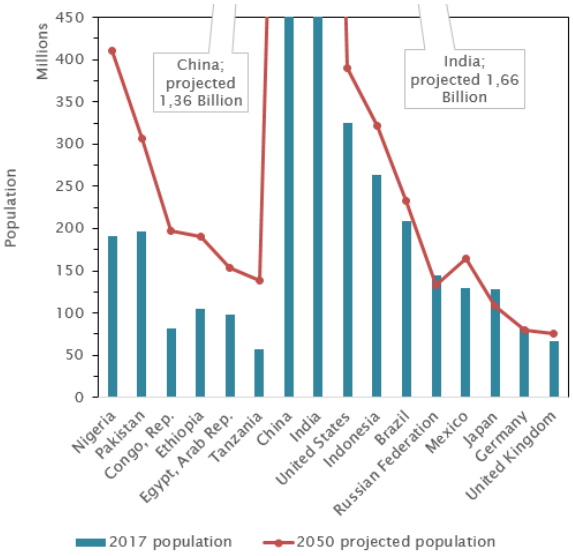


Figure 1.4: Projections of population change by 2050 for selected countries[1]

Fig. 1.3 and Fig. 1.4 show together that several of the countries expected to grow the most, are also the ones who are farther away from the energy consumption threshold for prosperity (2.8 toe per year per capita). And economies like Indonesia, Mexico, Brazil, India, will most likely increase their energy expenditure as more people from those countries become wealthier and obtain access to better services and products.

A limitation on this analysis that has to be mentioned is that the energy consumption of a country is not only related to the life standard of its inhabitants but also to the nature of the most important economic activities. Providing an example, China consumption of energy per capita may look not far away from the prosperity line, but this could be related more to the intense industrial activity rather than to a direct increase in living standards.

### 1.1.2. How much energy will be needed?

The economic and population growth discussed in the previous sections poses a challenge in the energy demand; in 2014 the International Energy Agency (IEA) reported the global demand as being 13,700 Mtoe [34] which is roughly equal to $1.59 \times 10^5$ TWh (given an equivalence of $1$ Mtoe $= 11.63$ TWh) this demand is expected to increase to around 17,886 MToe ($2.08 \times 10^5$ TWh) by 2040 [35], this is an increment of 30% percent.

Currently the actual distribution of the primary energy supply is dominated by fossil fuels, as can be seen in Fig. 1.5, in 2015 around 86% of the total supply was contributed by gas, coal and oil, while less than 10 percent was attributed to renewable sources of energy.

Energy shortage using the current sources of energy is not expected in the very near future (next

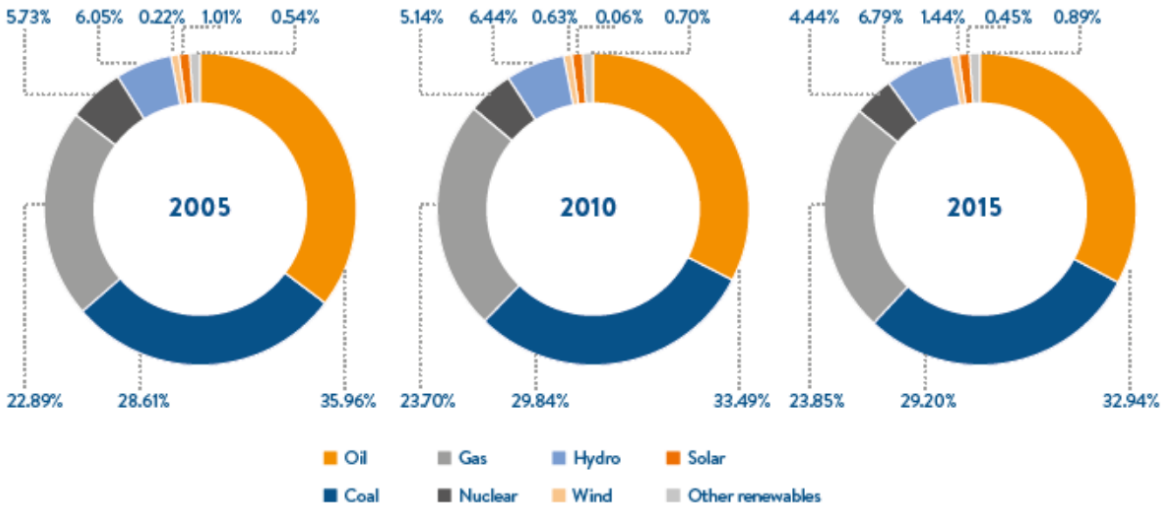


Figure 1.5: Comparative primary energy source consumption over the past 15 years. [4, p. 4]

20 years). However to continue with it carries an assortment of problems, for example: scarcity of resources before the end of the century, energy insecurity due to oil driven geo-politics, consequences of Greenhouse Gas Emissions (GHG). The next section explains these problems in detail.

## 1.2. The unsustainable path of Fossil Energy

Humanity cannot indefinitely rely on non-renewables and specifically fossil fuels (FF)(oil, gas, coal) to drive its energy needs. The future is not completely certain, on when we will run out of FF. Current estimates published on 2017 by British Petroleum (BP) predict that by dividing total remaining world reserves by the rate at which the oil is being extracted on 2016 (Reserves to Production R/P ratio) the oil reserves will exhaust in 50.6 years[36]; similarly the same report gives an R/P ratio for gas and coal of 52.5 and 153 years respectively.

The previous estimations are quite possible they may change in coming years. Mainly due to the fact that the amount of found proven reserves during the past decade, increased for gas and oil by an amount of 18% and 23% relative to 2006 levels [36]. This could also happen again in the near future sending the R/P ratio further into the future. But the opposite is also possible that under an increased demand of energy, the production of next years becomes more intense and the estimate shortens instead.

Scarcity of FF over mid century is therefore a very real problem, but is not the only reason pushing towards finding alternatives for the main source and carrier of energy.

### 1.2.1. Energy Security and Economy Diversification

Energy security can be defined as the protection from threats that have an impact on the continuity of the energy supply chain [37]. For a long time as explained by the distribution in the energy sources (see Fig. 1.5) this meant to have a secure supply of gas, coal and most importantly oil.

Oil as a commodity is subject to many price changes due to an array of geopolitical and economic issues: political instability and wars; rig depletion's; emerging markets and new rigs flooding the global production; lack of demand due to economic recessions; oil producing countries agreeing on cutting extraction to drive up prices. The list of factors is as diverse as with any other exported commodity. On Fig. 1.6 it can be seen how the crude oil barrel price has varied since 1970 together with a list of

events that are likely linked to the big changes in the prices.

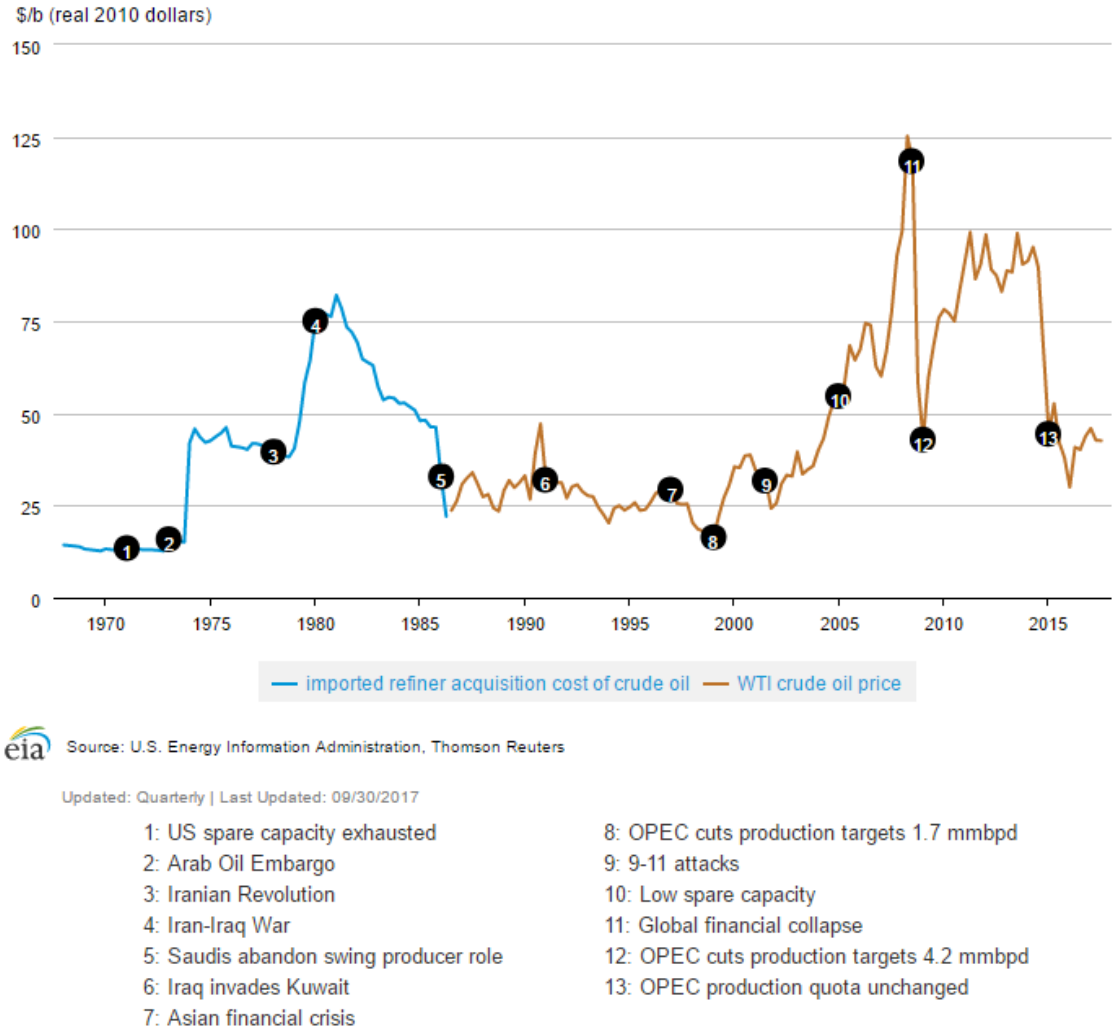


Figure 1.6: Crude oil prices and key geopolitical and economic events [5]

Facing these changes in the oil prices, the world is then divided into two types. The countries without oil reserves and those who provide it to the rest of the world. During the past century and early 2000's oil importing countries had their economy growth benefited during periods of low oil prices. But in the case of scarcity or sudden spike of the prices it could also lead to economic stagnation or recession. The oil embargo of 1973 provides a good memory of this scenario.

On the other hand, for countries having a surplus of oil reserves. A high oil price leads do a direct increase in wealth. But it can also create a dangerous situation of over dependence on oil. A period of high prices and continued growth makes governments over optimistic on the future prosperity. Having as a consequence a likely harsh downfall if the oil price collapses.

Previous scenario can be taken into example by recounting the economic crisis in Mexico of 1982. In 1971 the Cantarell oil reservoir was discovered, the most productive in Mexico to date [38]. The government had a sudden surplus of income; and foreign credit was easy to be obtained. By 1982 external debt was close to 91.57% of national GDP. When the oil price started decreasing in the same year as seen in Fig. 1.6 the country entered into a deep recession from which it would not fully recover until 1989 [39].

At the face of these problems the most plausible solution continues to be diversification of the

energy sources and the economic activities. In the past the only way to diversify the energy sources was to obtain the FF from other countries or to stockpile in anticipation of high price periods, or heavily invest in nuclear energy . But in recent years with the drop in prices of renewable energy choice, diversification is a practical reality.

Three examples of countries that are diversifying its energy sources are Costa Rica, Denmark and Germany. In 2015 97% of Costa Rica's electricity came from a mix of using hydroelectric, geothermal and wind [40]. Denmark in the same year obtained 42% of the electricity energy by harvesting wind energy[41]. And Germany by its aggressive bet on renewable energy, obtained in 2016 21% of its total electrical energy needs in the public sector by using Wind and Solar Energy [42], these numbers albeit optimistic do not mean that the energy economy is totally balanced. Transportation in Costa Rica accounts for around 70% of the energy consumption and it is covered completely by oil; Denmark and Germany are still heavy users of FF when it comes to heating and transportation needs.

### 1.2.2. Pollution due to FF usage

Air pollution due to FF burning is also a major concern. More than 3 million people died in 2010 in the world due to outdoor air pollution coming from carbonaceous particles smaller than 2.5 micrometers $PM_{2.5}$ and $O_3$. 50% of the causes were attributed to residential use of energy, power generation and land traffic [43]. And by 2050 estimates, mortality related to air pollution can increase to above 6 million per year globally in a business as usual scenario.

### 1.2.3. Human induced Climate Change

Burning of Fossil Fuels is one of the main causes for increasing levels of $CO_2$ in the atmosphere. Current concentration levels are at 406 parts per million (ppm)[44]. This value lies in contrast with studies of the ice cores concentration of $CO_2$, which report an oscillation of the $CO_2$ concentration between 180 to 280 ppm for the last 400 thousands of years. In comparison with this timescale the jump from 280 ppm to current levels was obtained in just 67 years (1950 to 2017). Current trends show a rate of increase of 2 ppm each year [45].

Increasing $CO_2$ concentration is relevant because this gas is accepted as one of the agents that causes grenhouse effects alongside methane, ozone, water vapour, and nitrous oxide. At the same time the $CO_2$ concentration is increasing it is also observed that the global mean temperature has risen by one Celsius degree from pre-industrial times of year 1880. Fig. 1.7 shows four climate study institutions closely agreeing on these records.

On the face of these changes, in recent years scientific research has tried to find, if there is a real connection between human caused $CO_2$ emissions and the rising of the global average temperature. The consensus of the scientific community on the veracity of this connection, lies between 97 to 99 percent [46].

Therefore in this thesis it is assumed climate change is real and is most likely anthropogenic. But, whether or not its effect is harmful for the entire world is a debated subject, the Intergovernmental Panel on Climate Change (IPCC) predicted several consequences if no action is taken to reduce the current trend on GHG emissions [47] some of them are listed here:

- The average temperature of Earth may increase by up to 4 °C by year 2100 from pre-industrial times (year 1880).
- Increase of sea level.
- More acidic sea due to dissolution of $CO_2$ in the oceans.
- Changes in agricultural production due to different responses of crops to changing temperatures and water availability.

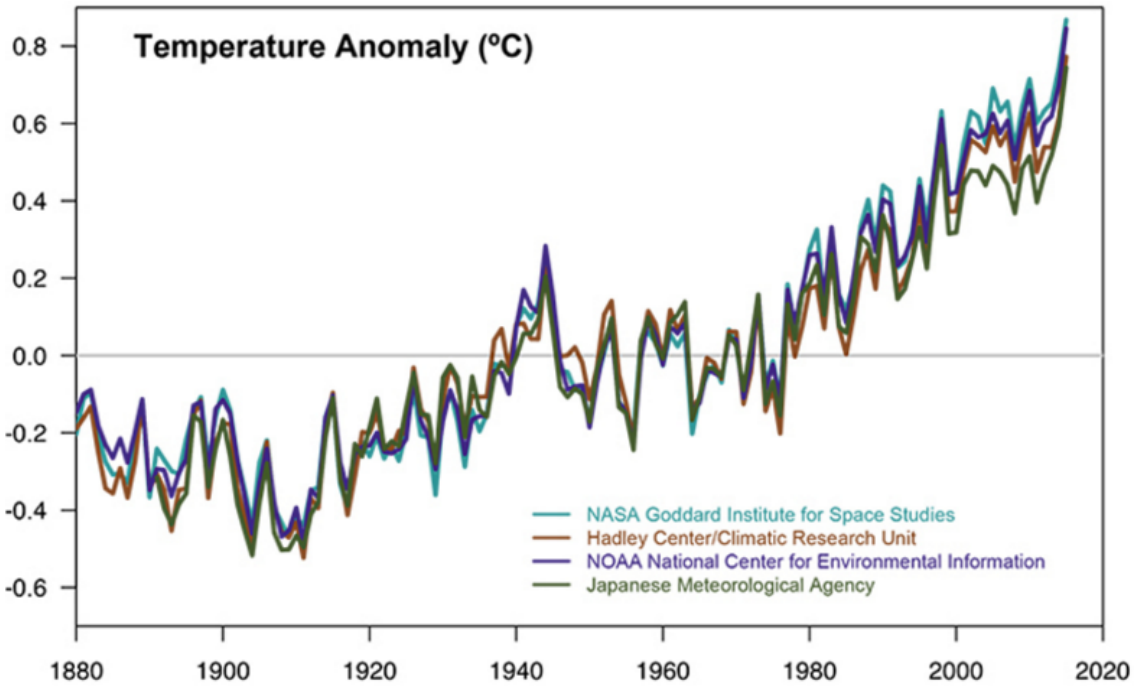


Figure 1.7: Global mean temperature records, since year 1880 by 4 climate study institutions [6]

- Less need for energy consumption to warm cold places, and more energy needed to cool down high temperature regions.
- Migration patterns, and conflicts over resources could be affected by the rise of temperatures.
- Naturally ocurring storms could be strenghtened due to warmer oceans.

What was talked in the previous sections. The growing energy needs and the disadvantages of primarily using fossil fuels. Raises a major challenge to find ways that change how energy is harvested and consumed. The following section describes solutions that have been proposed to alleviate this problem, some of them come from international cooperation, like the 2015 conference of the parties held in Paris and the European Union goal on energy efficiency.

## 1.3. How to overcome the energy challenges?

Referencing again Fig. 1.3, we can observe that not all countries that are highly developed have the same consumption of energy per person, in average a United States citizen almost doubles the energy consumption of a Japanese. It is increasingly seen that to enable growth in a sustainable way, energy consumption needs to be optimized. So energy efficiency will have to play a big role in the future.

To give an example in how developed nations are applying energy efficiency. It is explained in the next subsection, the European Union current target on energy efficiency.

### 1.3.1. Energy Efficiency in the European Union

The European Union presented a common goal on efficiency and energy use reduction for all its members. The goal established is to decrease the emissions of GHG by 40% by 2030 in comparison with

1990 levels[48], this goal can be considered an extension of the goal to cut by 2020 in 20% the GHG emssions.

New policies related to this objective were placed by a portion of the EU members, some examples of them are [49]:

- In Germany preferential loans were given for the construction of highly efficient new homes, and the retrofitting for energy efficiency of existing buildings.
- In France the new draft national laws includes a 30% fiscal reduction on the cost of energy efficiency renovations.
- Manufacturers of cars are requested to make public the $CO_2$ performance standards for cars and vans
- Smart-meters aimed at making possible to know for consumers when the electricity price is lower; due to the cyclical availability of Renewable Energy.
- Regulation on minimum energy performance for products and making this information available for the consumer.

The European Union goal is part of a bigger effort. As a single group the EU presented this goal as an Intended Nationally Determined Contribution (INDC). The INDC came as a commitment during the global summit in 2015 on climate change. The next subsection talks in detail of this international summit.

### 1.3.2. The Paris COP21 Agreement

In 2015 the United Nations Framework Convention on Climate Change (UNFCCC) celebrated the 21th Conference of the Parties (COP21). In it, all the 193 members of the United Nations and 4 more non members participated together on a new deal to mitigate and adapt to the phenomena of climate change.

The result was the Paris Agreement and the Intended Nationally Determined Contributions (INDC). The way this agreement worked, is that under the rules delimited by the Paris Agreement. Each nation would propose for itself what goals and measures would be taken to reach the goal of keeping global temperature average increase in this century below 2°C since pre-industrial levels[50].

This agreement is significantly different to the previous international cooperation on climate change; the Kyoto protocol. The Paris Agreement did not impose penalties to countries who do not not achieve their goals. Another difference is that in the Paris agreement each country in the world, both developing regions and already highly developed ones, had to sumbit their own INDC. Meaning all nations had differentiated responsibilities when mitigating climate change, but all played an important part.

The nations through their commitment stated in the INDC established several ways to achieve the emission reductions, including but not limiting to:

- Restore carbon sinks for example by reforesting forests.
- Reduce the use of coal, oil, and gas for heating and to produce electricity.
- Incentive energy efficiency.
- Apply carbon-tariffs to discourage the use of fossil fuels.
- Use of electric and hydrogen powered transportation.
- Increase the installed capacity of Renewable Energy sources.

Emerging economies had a very different INDC that the ones from developed countries. This is because as a general situation they recognize the need to provide more energy to their people while also keeping new GHG emissions at minimum. The next sections describes the part renewable energy is expected to play within this setting.

### 1.3.3. Green Energy in the INDC

Renewable energy technology is sometimes called green energy due to not emitting GHG during operation. This is specified because during manufacturing the necessary components are energy intensive in many ways and emissions of GHG are incurred.

However in comparison renewable energies during the total life-cycle as a much lower cummulative emissions than any fossil fuel option. As a consequence renewable energies been given a large part of the responsibility in several of the INDC to achieve the goal in reduction of GHG emissions.

108 INDC's include renewable energy in some form as part of their energy mix, to reduce the Greenhouse gas emissions, outstanding within these commitments it can be mentioned some of the biggest efforts top energy consumers have on Renewable Energy. China projects to increase by 2020 its wind energy capacity to be 200 GW,[51]. This goal is well on track since in 2016 China installed 23.3 GW of wind power taking its total capacity to 169 GW [52].

Another big player India is planning to go from 10 GW of installed capacity of solar energy in 2017 to 100 GW by 2022[53].

To give some context in 2015 for the United States the total installed capacity for electricity productions amounted to 1064 GW of which, 64% amounted to fossil fuel, 19.7% to nuclear 6.5% to hydro and only 9.6% to others form of renewable energy like wind with 72.5 GW, and 12.6 GW of solar energy installed.[54]

## 1.4. Renewable energy, unexploited potential

Having discussed in previous sections the need for emission reductions and the integration of clean energy sources into the mix, now in this section it will be briefly described what are the most important sources of Renewable Energy together with the potential of each.

Fig. 1.8 shows the potential of different sources of energy to supply the actual demand of global population, this demand is represented by the brown circle as being close to 18.5 TW-year, (TWy) in 2015. Close to this value are the potential for the renewable energy resources in Earth and farther to the right are the total estimated energy reserves for the non-renewable.

The author gives 23,000 TWy for sun energy potential per year. This value takes already into consideration that around 65% of light is absorbed by the atmosphere before reaching the ground. The sun potential also assumes only the light incident on continental land. o give an estimate on how much

Considering the 23,000 TWy sun potential and assuming only 20% of conversion efficiency with a 1.7% of all continental land covered would give enough power to cover current energy needs more than 4 times.

$$\frac{23,000\,\text{TWy} \times 20\%\,\eta \times 1.7\%\ (\text{land use})}{18.5\,\text{TWy}} \approx 4 \text{ times } 2015 \text{ energy needs}$$

On a smaller scale but also quite significantly wind power shows the potential to cover all the energy needs. Hydro power is already well established and although it has room to grow it is not expected to

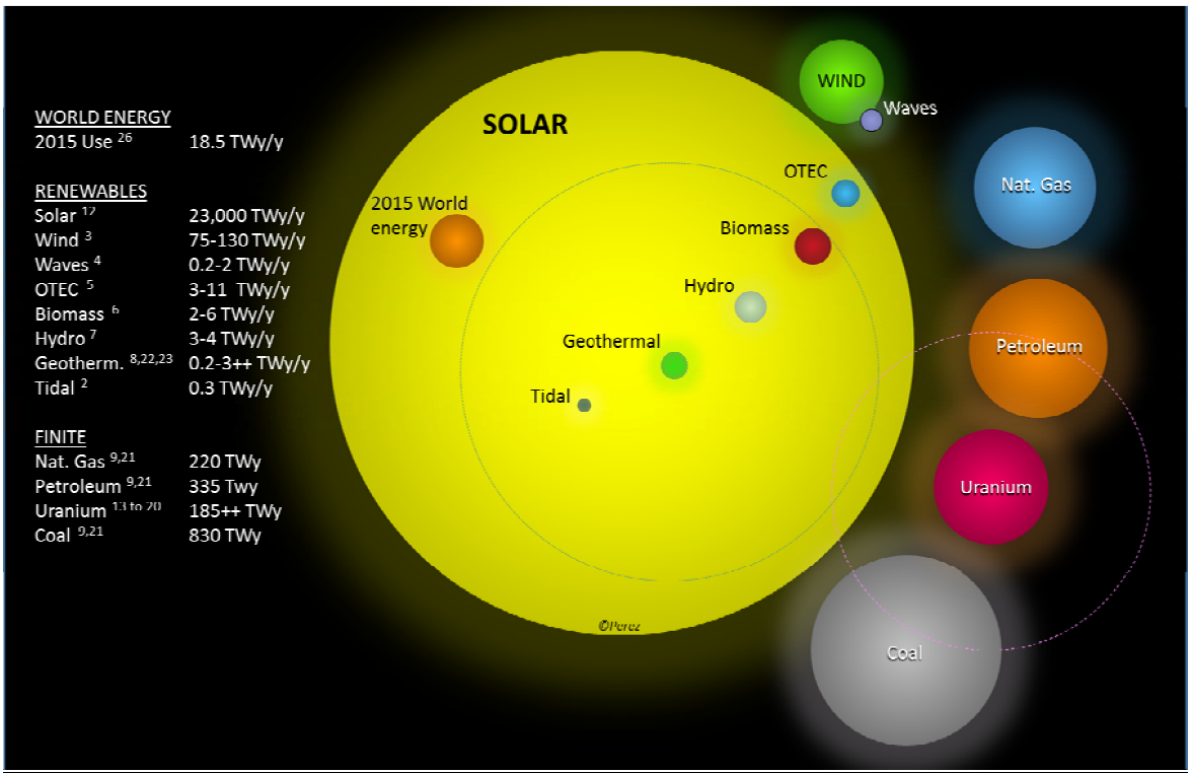


Figure 1.8: 2015 estimated finite and renewable planetary energy reserves (TW-years). Total recoverable reserves are shown for the finite resources. Yearly potential is shown for the renewables [7, fig. 2]

be enough to supply all the global energy.

In the case of geothermal, several countries like Indonesia. Mexico, Iceland, New Zealand and Italy for example; have a significant installed capacity for generation (more than 500 MW)[55], however the future potential is localized to those countries with enough geological activity.

Biomass is an interesting case since it can help greatly in the energy transition period from oil based fuels with the use of ethanol fueled engines, however because of the low efficiency of biomass to wheel energy conversion (around 7%) [56] and the displacement of land it represents to food crops, the potential will always remain lower than the necessary to satisfy all energy needs.

Lastly in the case of ocean energy like tidal, wave and Ocean Thermal Energy Conversion (OTEC) the potential is expected to be useful for coastal areas, and islands, contributing together with solar and wind energy.

### 1.4.1. Solar Energy, how much would be needed?

As explained before it is possible to power completely the world by means of using solar power only. But, How much area of photovoltaic solar cells would be needed, when compared to all the available land?

Fig. 1.9 provides a sample of all the area needed. In this figure a forecast is used from the International Energy Agency for the 2030 total energy supply needed. Therefore, the total energy needs are assumed as $1.99 \times 10^5$ TWh. The author draws areas to be covered by solar panels to satisfy this demand. Assuming a conversion efficiency from the sun to electricity as 20%; and 2000 hours available per year of direct sunlight. The map then estimates that per square meter 400 kWh per year can be harvested. The total area needed to satisfy the demand is quite big (496,805 square kilometers); but it is not so immense when distributed around the world.

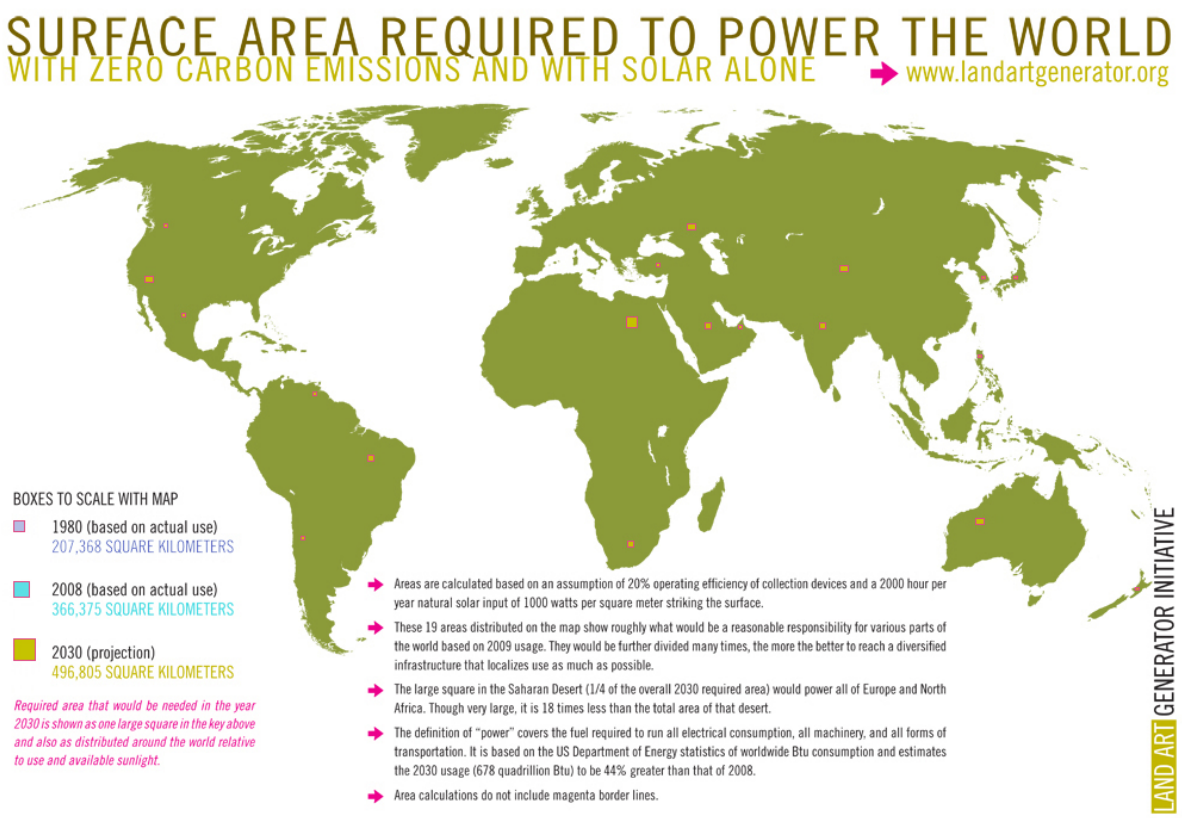


Figure 1.9: Total Area required to supply all energy needs of the World in 2030 with Solar Power [8]

The author makes use of 19 areas around the world to distribute the solar harvesting. However in reality many more at a smaller size would be installed in a pure solar powered world, to reduce the transmission losses and for individual energy security on each country.

Also important to consider is that by using a mix of other types of renewable energy sources like off shore and inland wind energy, the area using solar energy at the end would be smaller. These estimates do not take into consideration that solar cell panels are expected to become more efficient over time by the use of novel technologies that will be explained in following chapters.

# 2

# Motivation

## 2.1. Introduction and basic working principle of a solar cell

In the previous chapter it was established how harvesting energy from the sun can contribute a major part of the energy needed in the near future. Section 1.4.1 discussed using solar cell for this purpose. This chapter briefly explains the basic principle of electricity generation using solar cells, followed by a discussion of the most important achievements that led to the present day technologies. Afterwards it will be discussed an array of the leading technologies in the field nowadays. Finally , the technology used in this work will be discussed, the limitations associated with it in recent research; and the main limitation this work aims to tackle.

The photovoltaic effect happens when in the presence of electromagnetic radiation, (be it visible light or not) a potential difference is observed, across two different materials forming a junction[57]. A solar cell takes advantage of the photovoltaic effect to harvest energy in the form of electricity. The effect very briefly explained consists of four steps: 1) Absorption of electromagnetic radiation in the form of photons. 2) Generation of charge carriers (electron-hole pairs) due to the photon energy being enough to excite an electron to a higher energy state and leaving behind a void called hole 3) Separation of charge carries due to the junction materials forming a semipermeable membrane that in one extreme allows only for holes to propagate and in the other extreme only electrons, these membranes separate the p-n materials. 4) The generated charge carriers are collected at the contacts to perform work in an external circuit before returning to the cell and recombine.[57]. In Fig. 2.1 the charge carriers and the p-n junction of a common silicon technology cell is shown.

The above process is not so straightforward in reality because many other interactions happen at the same time, for example a large portion of the incident light gets reflected. And inside the solar cell materials, the charge carriers generated normally tend to quickly recombine, and the ones who get to the contacts also have to deal with difference in potential barriers before being collected.

## 2.2. Brief History on Solar Photovoltaics

The photovoltaic effect was first discovered in 1839, when Edmond Becquerel found by accident that platinum electrodes placed apart submerged in a electrolyte, could exhibit a voltage when light illuminated the electrodes [10]. In 1873 Adams and Day discovered in Selenium the first solid material to exhibit a behaviour similar to Becquerel experiment and show a current under action of light. Using this result In 1883 Charles Fritts made the first solar cell by coating molten selenium with a thin layer of gold, this cell had an energy conversion between 1 and 2 percent [58]. A diagram of the described cell can be seen in Fig. 2.2.

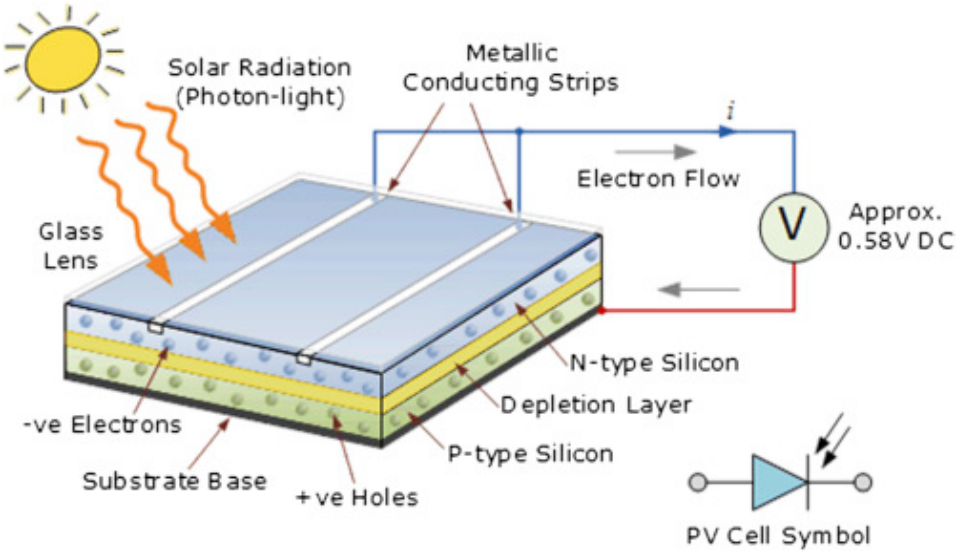


Figure 2.1: The Photovoltaic Effect in a Silicon solar cell [9].

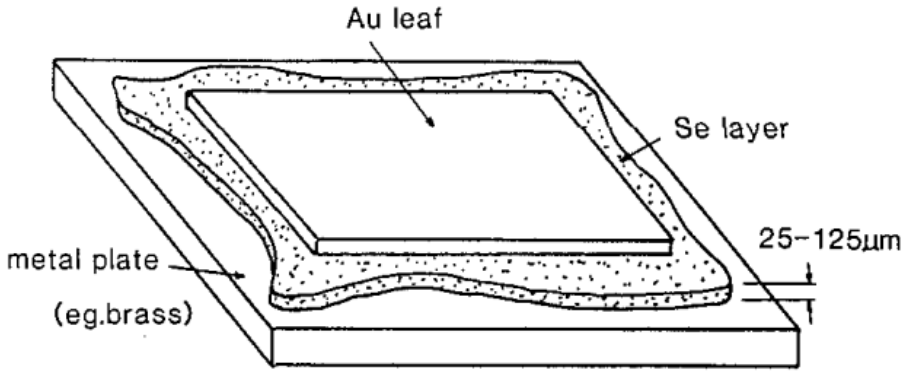


Figure 2.2: Thin film selenium cell demonstrated by Fritts in 1883 [10].

One of the most important contributions came in 1905 when Albert Einstein published his famous paper on the photoelectric effect. He theorized light had packets of energy (now called photons) and that this energy varied according to the frequency of the light. He proposed that depending on the material, the photoelectric effect could only be observed until a specific limit on the frequency of light. Over this limit no matter how intense the light source would be it would not liberate an electron. The study gave a physical equation framework to study what type of light was needed to trigger the photoelectric effect [59].

It would take a long time before another major discovery was made on solar cells. In 1954 Daryl Chapin, Calvin Fuller, and Gerald Pearson at Bell Laboratories discovered that pn silicon junctions diodes could generate a voltage when placed under light. They invented the first silicon solar cell, having an efficiency of 4.5%. Months later this efficiency was improved to 6% [60]. Other materials were also discovered soon as being viable for solar cells like GaAs made by RCA lab in 1956[9]. Together with these discoveries the underlying physics of the cells were starting to be theorized, like for example the paper by Joseph Loferski in 1956 explaining how materials with a bandgap between 1.1 and 1.6 could possibly have a better potential for ultimate efficiency than silicon [61]. Another very important work was the paper of William Shockley and Hans J. Queisser in 1960 relating the ultimate efficiency of a solar cell as a function to the bandgap of the material [62].

The initial solar cells albeit having a low efficiency, were given attention for space applications. Where autonomous energy was of paramount importance over cost. One of the first examples was the year of 1958 when the NASA Vanguard Satellite was launched being the first one to have solar cells as a backup power [60]. The next big improvement was made with the introduction of a new type of technology. Thin film solar cells, that did not need as much material thickness as silicon wafers to absorb the same amount of energy. In 1963 a CdTe/$Cu_2$ cell having 6% efficiency was reported [63]. And in 1974 a cell having a structure of p–$CuInSe_2$/n–CdS 12%.[64]. The first experimental working cell of a–Si technology was reported on 1976, having a structure of a–Si:H; p-i-n single junction and an efficiency of 2.4% [65]. In the past 2 decades several improvements were made on silicon based solar cells and on different thin film technologies. It is beyond the scope of this thesis to explain each incremental achievement. The next section makes a jump in the time line, to enlist now the current technologies in solar cells.

### 2.2.1. Current Photovoltaic Technologies

Current PV technologies can be classified in 3 main groups [66].

**First generation**: It is the most mature technology, consisting on p-n junctions of crystalline silicon (c-Si), they are further divided into mono-crystalline or multi-crystalline cells. The current record of efficiency in a silicon crystalline cell goes to Kaneka, having reported 26.7% efficiency for a n-type heterojuction cell employing interdigitated back contacts [67].

**Second generation**: It comprises Thin Film (TF) technologies. They have this name because the thickness of the photosensitive material used, is orders of magnitude lower than for crystalline silicon. a–Si:H cells, for example usually have for the absorbing $i$ layer a thickness between 0.2-0.3 µm. While crystalline silicon wafers in contrast usually have a thickness between 250-350 µm[68]. The main TF technologies are enlisted below:

- Amorphous silicon (a–Si).
- Multi-junction thin silicon film (a–Si/µc–Si).
- Cadmium telluride (CdTe).
- Copper, indium, gallium, (di)selenide/(di)sulfide (CIGS).
- Gallium Arsenide.

TF solar cells although called second generation in reality they are not far away in their birth as the first generation. c-Si has been researched more extensively due to its advantages, like being a cheap material, in great abundance and with a manufacturing process that has matured by simultaneous efforts to commercialize it. However TF technologies have also their own advantages, like requiring very little active photovoltaic material. In some case being flexible solar cells and lightweight added to their versatility. In recent years as c-SI technologies have matured, there has been increased attention to the possibilities TF offer. Efficiency in TF commercial modules is coming closer to what has been seen for c-SI modules. As of June 2017 GaAs TF record modules have a confirmed efficiency of 24.8% [69] [70]. In comparison CIS an CdTe follow with record modules of 19.2% and 18.6% efficiency, respectively [71] [72]. The last cell of the group is the tandem cell made of two absorbers a–Si/nc–Si (also called micromorph) the record module has an stabilized efficiency of 12.3% [73].

**Third generation**: They introduce new materials and novel concepts on better use of the incident light to increase the efficiency while using cheap abundant materials. This category is further subdivided into:

- Organic solar cells (OPV.
- Dye sensitized cells DSSC.
- Perovskite
- Quantum Dots
- Multi junction solar cells and em cells.

Multijunction cells are not restricted to a certain type of material. It is a definition for solar cells that have more than one absorber layer. Multijunction solar cells were developed at the beginning for space applications. Since the high cost of them were not more important in this market, than the desire for a higher efficiency. The other PV technologies in the third generation are relatively new. From them only organic cells have a commercial module with a reported efficiency of 8.7%. It is interesting to mention also the case of perovskites, because in four years they took a leap from 12% to 22.7% in efficiency [74]. Even so there are not yet commercial modules, mainly because of long term stability concerns.

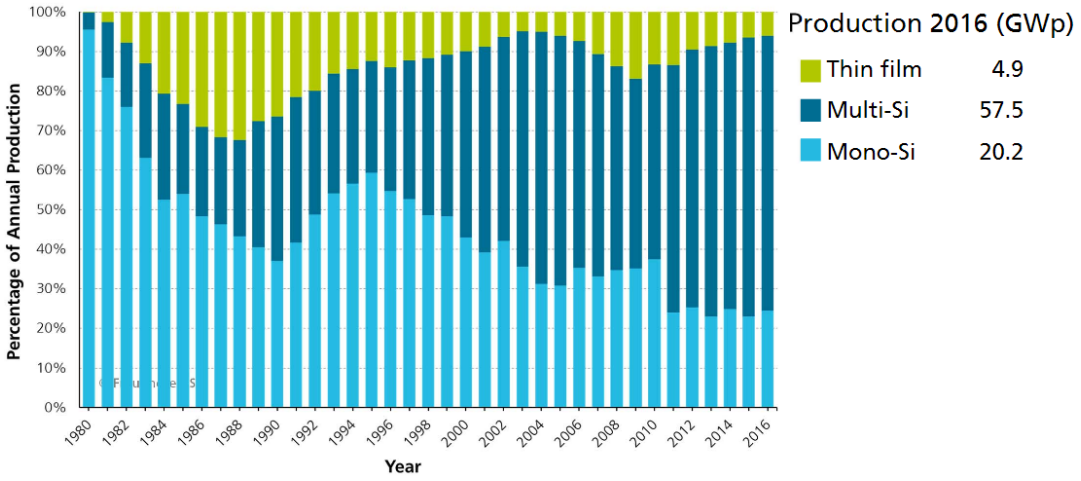


Figure 2.3: Distribution of Market Share for Photovoltaic Technologies [11]

Although the diversity of solar cell technologies is quite vast, the solar cell market for commercial modules is currently dominated by single junction solar cells based in c-Si technology. In Fig. 2.3 can be seen how the global market share has changed since 1980. TF technologies got a share of almost a 6%. But there are reasons to believe that in the future the market could become more diverse,

to include a bigger portion of promising TF technologies, and third generation solar cells. The main reason is the maturing of silicon based technologies as the efficiency draws closer each year to their theoretical limit.

## 2.3. Overcoming the theoretical limit

A solar cell like any other device that converts energy, has an ideal limit over what amount of incident energy can be converted. William Shockley and Hans J. Queisser [62] defined a theoretical limit for a single junction material as a function of the bandgap, named now as the Shockley Queisser Limit (SQL). The maximum limit they calculated was of 33.16% efficiency at a bandgap of Eg=1.3 eV [75]. c-Si has a bandgap lower than this, being Eg=1.12 eV. The SQL for this bandgap, together with the bandgap of other materials is shown in Fig. 2.4. The SQL comprises these type of losses:

- Non absorption of photons with energy below the bandgap of the material.
- Conversion into heat of photon energy above bandgap (thermalization).
- Voltage loss due to radiation of thermal energy.
- Radiative Recombination.

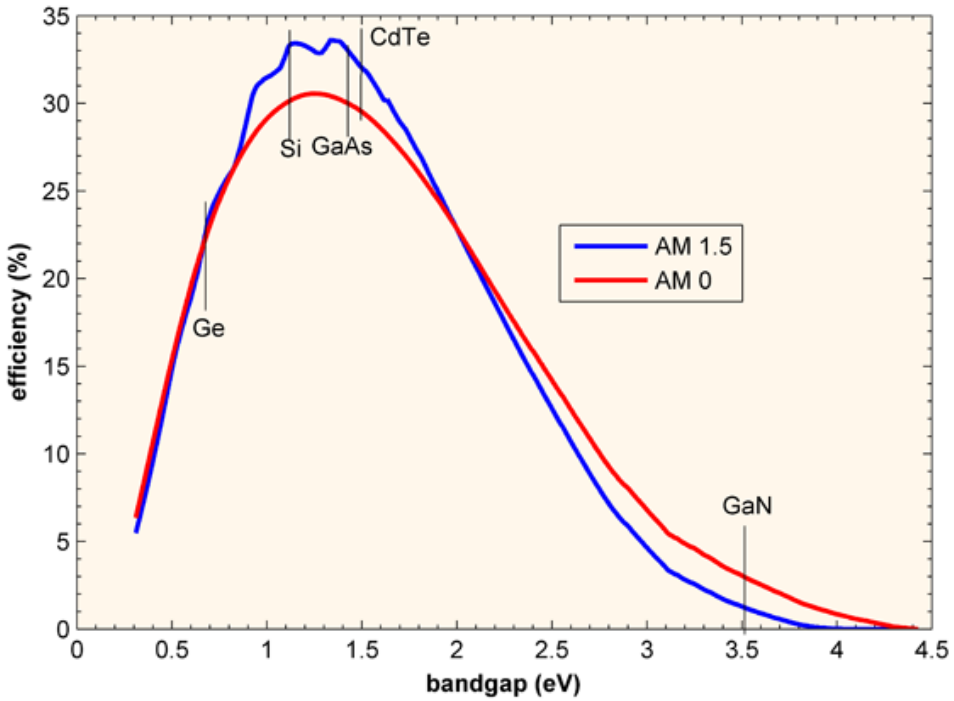


Figure 2.4: Maximum theoretical solar cell efficiency as a function of the material bandgap, using SQL assumptions.[12]

Other losses that are common in solar cells are not accounted in the SQL. Example of these losses include optical (reflection and transmittance) and other types of recombination like Auger or Shockley Read Hall (SRH). A more detailed balance by Tiedje *et al.* [76] incorporates also Auger recombination and free carrier absorption losses, calculating for c-Si a maximum theoretical efficiency of 29.8% percent under AM1.5. The best performing to date c-Si solar cell (26.7%, [67]) is already close to the SQL. In order to produce devices that go over this limit. It is necessary to work outside of the SQL assumptions. The concepts challenging the SQL are diverse. One of these concepts is multiple electron-hole pairs by spectral conversion. This method proposes that if the energy of a photon is higher than the

bandgap, instead of being lost as heat, a way could be found to create two low energy photons, to excite additional e-h pairs. This method is also called down-conversion. It has been applied with DSSC solar cells to avoid degradation induced by UV light by converting it first into higher wavelength ligth that can be utilized by the DSSC material [77].

Another concept to go over SQL limit is called up-conversion. It takes two sub-bandgap photons that would normally be transmitted and lost. To convert their energy into one above-bandgap photon. The up-conversion process has been proven with rare earth elements with fluorescent materials and with intermediate energy states. Where photons with energy below the bandgap excites carriers to an intermediate state, with new photons exciting the carrier from the intermediate state to the conduction band. Both up-conversion and down-conversion aim to achieve EQE values above unity [78]. Similar to spectral conversion, is the concept of spectral separation where incoming sun light its refracted or filtered, and later redirected. So that each part of the spectrum can reach different solar cells, according to the bandgap in which they operate [79]. Also in modification of incoming light another interesting concept is thermophotovoltaic solar cells. For this concept incident light is first trapped or concentrated into a material (emitter). This material when heated due to radiation it emits then photons at a specific low bandgap matched to a solar cell that acts as the receiver [80]. Out of all the concepts that challenge the SQL limit one of the most important is the concept of multijunction solar cells. They are discussed further in the next section.

### 2.3.1. Multijunction Solar Cells, opportunities and challenges

In a multijunction solar cell, a number of different layers are stacked one on top of the other. The basic working principle is that each layer has a different bandgap in order to absorb a different part of the light spectrum. The layer with the highest bandgap is placed on top to received the incoming ligth first. Photons with an energy below the bandgap of the first layer are transparent to this layer and a fraction of them are absorbed into the next layer. Multiple layers with decreasing bandgap values can be stacked in this way. Fig. 2.5 shows an example of a multijunction solar cell, with 4 absorbing layers.

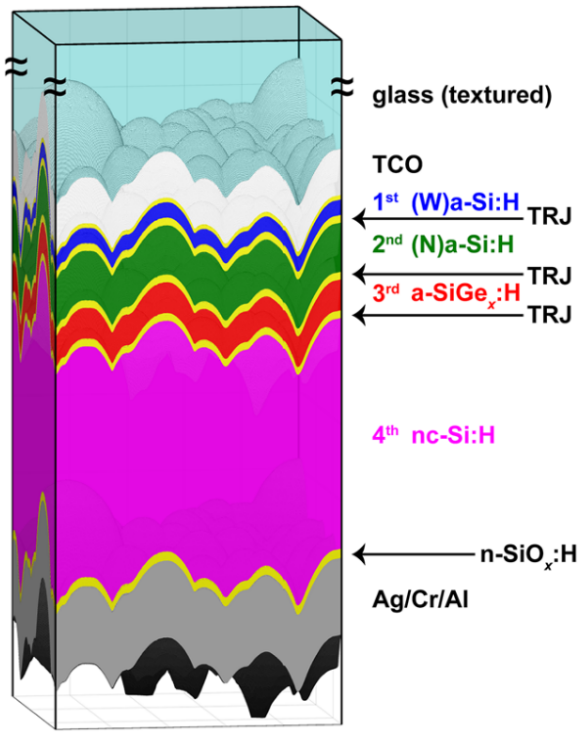


Figure 2.5: Illustration of a 4 junction (W)a-Si:H/(N)a-Si:H/a-SiGex:H/nc-Si:H thin-film silicon solar cell. Tunnel recombination junction (TRJ) includes all doped layers between the two neighboring absorber layers. [13]

Solar cells with two absorbing junctions are called tandem cells, but there are solar cells with 3, 4 or even more junctions. By applying the concept of multijunction solar cell a higher theoretical value for the maximum efficiency can be reached. Under non concentrated light, for 2 junctions the theoretical efficiency limit is calculated as being 42%. For 3 a junction device it goes up to 49%. As the number of junctions increases to infinite, the maximum theoretical efficiency is calculated as 68% percent [81]. The maximal theoretical efficiency increments with each added layer, but every new layer adds a smaller amount of efficiency than the previous layer. Multijunction solar cells are usually connected in series with one terminal in the top layer and the other connected to the bottom layer. In this configuration the voltage output will approximately be equal to the added output of the 3 cells. Where as the current that will be obtained will be limited to match the current of the lowest producing cell in the stack. Fig. 2.6 serves as an example of how $J_{SC}$ and $V_{OC}$ behave in a tandem solar cell. This hybrid tandem solar cell reported in [14], is made with a-Si:H as a top cell and polymer (PMDPP3T:PC60BM) as a bottom cell. As can be seen in Fig. 2.6 a), the $V_{OC}$ of the tandem cell is slightly lower than the sum of the individual materials as single junctions solar cell. However the tandem $J_{SC}$ is slightly lower than the $J_{SC}$ of a-Si:H as a single junction. Current matching in this solar cell is seen in Fig. 2.6 b). The output current of the bottom cell was reduced to better match the top cell $J_{SC}$. Since any extra absorption of this layer would not contribute to the solar cell performance.

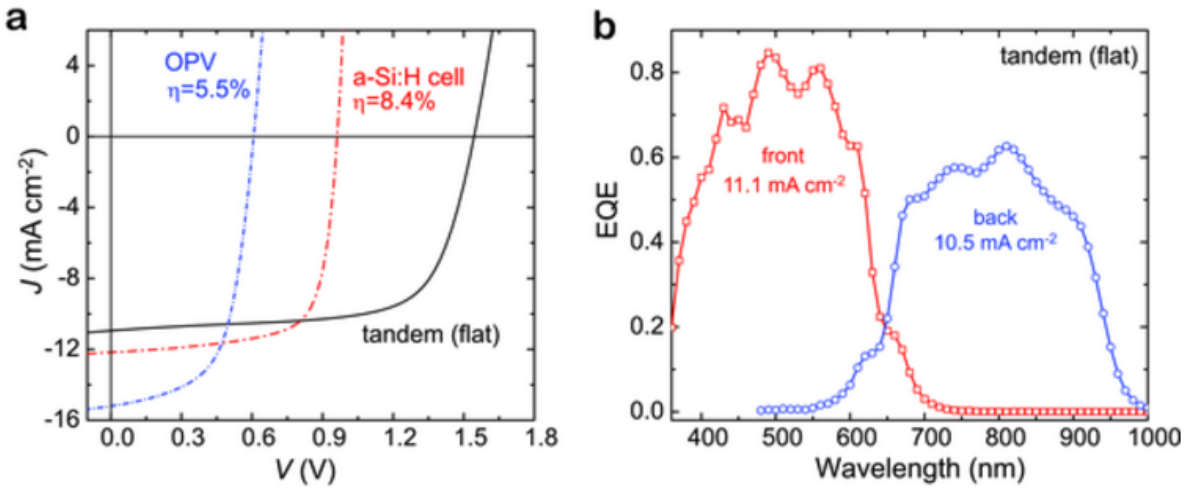


Figure 2.6: Performance of a hybrid a-Si:H/polymer tandem solar cell (a) J–V curves of best performing hybrid tandem solar cell (flat) and respective single-junction reference cells. (b) EQE of the flat tandem solar cell. [14]

Si *et al.* [82] discusses that each additional layer can increase parasitic absorption. Also that each layer represents another chance of reflection for the light. Another disadvantage is that for tandem cells connected in series between each junction a TRJ zone is needed to allow carriers to move and recombine between junctions. These needed areas are a source of voltage loss. The cell also becomes more complicated to manufacture with each additional layer. Because of these drawbacks, tandem or triple junction solar cells are often more attractive to make than cells with more than 3 junctions.

There is a trend in research of tandem or triple junction solar cells to try to create a device that is made from cheap abundant materials. With a manufacturing process that is not as energy intensive as with c-Si. Because of this reason hydrogenated amorphous silicon (a–Si:H) and hydrogenated amorphous silicon oxide (a–$SiO_x$:H ) are often materials used in multijunction thin film solar cells.

## 2.4. Motivation and Objective

a–$SiO_x$:H is a promising material with a higher $V_{OC}$ than c-Si, a–Si:H, or nc-Si. However the $J_{SC}$ of the single junction solar cells made with a–$SiO_x$:H is usually smaller than the 3 technologies just referenced. To increase the efficiency of a tandem or triple junction solar cell using a–$SiO_x$:H it would be ideal to find a way to increase the output current while still maintaining a high $V_{OC}$×FF. Kim *et al.* [15] reported a tandem cell with a structure of a-SiOx:H/nc-Si:H and an efficiency of 10.92%. The external quantum efficiency of the individual layers in this tandem cell can be seen in Fig. 2.7a. The nc-Si:H layer has a high photocurrent density of 12.53 mA/cm$^2$, but this current is significantly limited in the tandem cell output, by the a–$SiO_x$:H layer that only manages to produce 9.78 mA/cm$^2$. The a–$SiO_x$:H solar cell is thus current limiting. Only when used in a triple junction solar cell as seen in Fig. 2.7b, the a–$SiO_x$:H solar cell could generate enough current to not limit the performance.

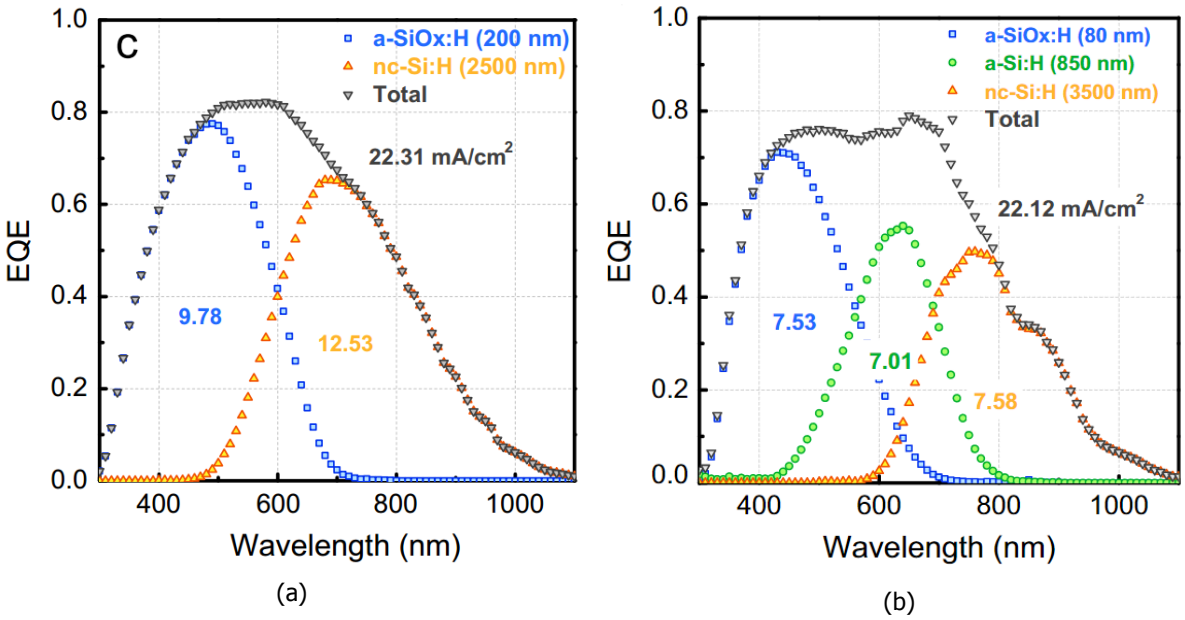


Figure 2.7: EQEs of (a) tandem (a-SiOx:H/nc-Si:H) and (b) triple (a-SiOx:H/a-Si:H/nc-Si:H) junction solar cells that use a–$SiO_x$:H as the top absorbing solar cell. The number under each EQE curve represent the photocurrent density of the individual layer. [15]

A common approach to increase photocurrent in solar cells is to increase the absorber layer thickness. For a–$SiO_x$:H solar cells it is possible to do this as well but up to a certain limit. Fig. 2.8a & Fig. 2.8b published in [15] show how $J_{SC}$ and EQE response increases as the intrinsic absorber layer is made thicker. However with increasing thickness the $V_{OC}$ ×FF product tends to decrease and after 250 nm in thickness the $V_{OC}$ ×FF drastically drops. Therefore practically this method can only increase $J_{SC}$ up to around 10 mA/cm$^2$. Using additionally other methods to increase photocurrent density, like enhancing light trapping and reducing reflection with textured surfaces; or optimizing the p-layer and n-layer thickness to decrease parasitic absorption. Made possible to achieve a photocurrent of 12.3 mA/cm$^2$. And a record efficiency of 8.8% for a–$SiO_x$:H single junction solar cells [83].

From this limitation in generated $J_{SC}$ comes the motivation for this work, to explore a new untested method with the goal of generating a higher photocurrent density in a–$SiO_x$:H solar cells. So this material becomes better suited to be paired in a tandem thin fim solar cell.

The objective of this thesis, is to investigate the effect bandgap grading can have on the performance of a single junction solar cell based on a–$SiO_x$:H. By keeping the bandgap high near the p- and n-layer, we aim to maintain the high $V_{OC}$×FF product that a–$SiO_x$:H cells have. And by introducing a smaller bandgap region in the middle of the graded region containing only a–Si:H we aim to increase $J_{SC}$ . This strategy is inspired by the benefits bandgap grading made for a–$SiGe_x$:H solar cells. The advantages

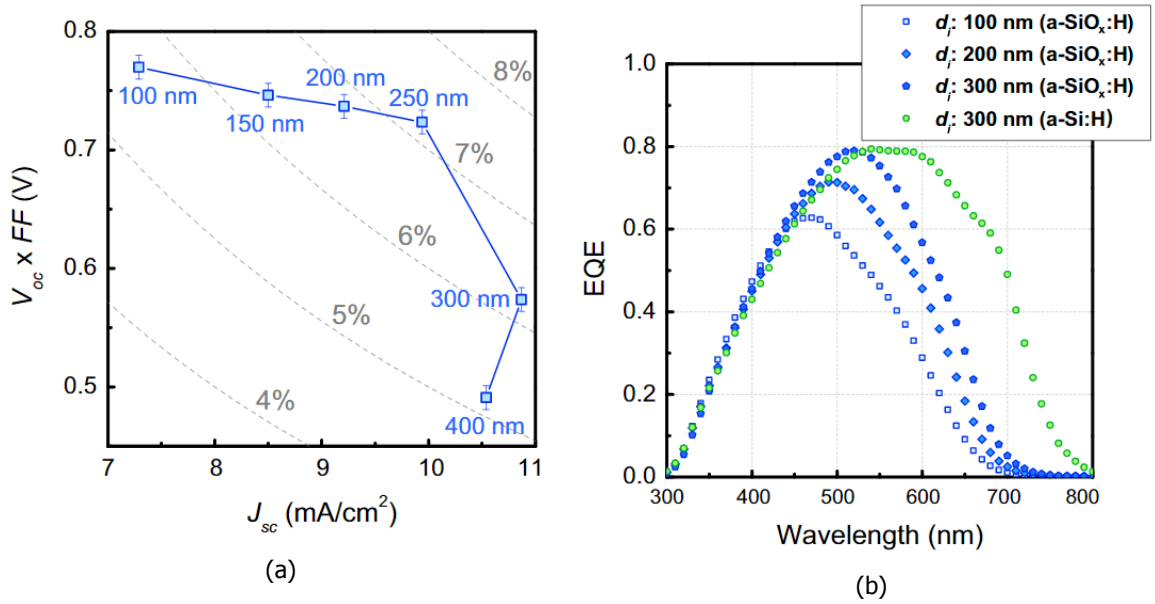


Figure 2.8: (a) External solar cell parameters and (b) EQEs of a-SiOx:H 1J solar cells as a function of i-layer thickness. [15]

grading have provided will be discussed in detail in Section 5.1.

# 3

# Experimental Setup

## 3.1. Introduction

The objective of this chapter is to describe the necessary steps to prepare the experimental cells. Materials used, equipment employed and processing of the results. First it will be explained the size and physical preparation of the samples.

Then it will be explained the type of equipment that is used during the manufacture of the experimental samples. These samples are of two kinds: the individual layers p, i, n, deposited to analyze their properties by separate; and the full experimental a–$SiO_x$:H photovoltaic cell. Later it will be discussed what instruments are employed to characterize the samples. Both of individual layers, and the full cells. The description of the instruments includes a brief description of the basic working principle. It will also be discussed specific methods to process the measurement information, that were necessary to properly describe the characteristics of the samples.

### 3.1.1. Preparation of Samples

The technology used in this work a–$SiO_x$:H . Is very thin, the thickness is always less than a few micrometers [68]. This makes necessary for the thin film to have a substrate over which the material can be deposited. When individual layers were deposited the material selected was Corning Eagle XG glass. For deposition of experimental cells the substrate used was Asahi VU glass. This material has a Transparent Conductive Oxide (TCO) coating made of $SnO_2$:F. The TCO also fulfills the function of increasing the path of light and light trapping. The glass substrates used are cut in stripes of approximately 9.7-10 cm×2.2-2.5 cm.

To make sure that the cells do not have any defects due to contaminated particles, the substrates undergo first a cleaning preparation:

- The substrate is submerged in acetone ($C_3H_6O$) for 10 min.
- Compressed nitrogen is used to dry up the glass.
- The substrate is submerged in isopropyl alcohol $C_3H_8O$.
- Again nitrogen is used to dry the glass.

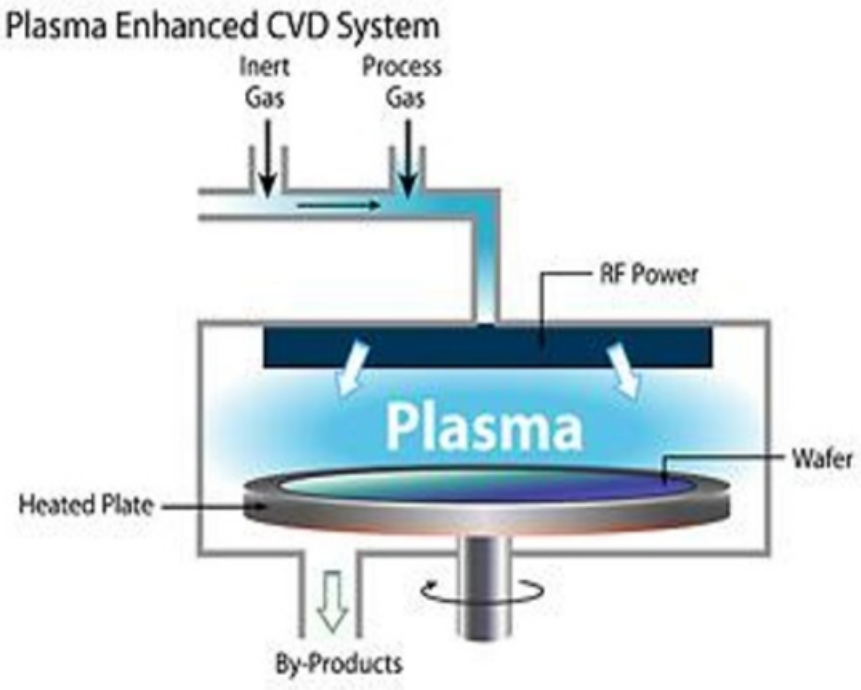


Figure 3.1: Schematic diagram of PECVD [16]

## 3.2. Thin Film Deposition Techniques

### 3.2.1. Plasma-Enhanced Chemical Vapour Deposition

The a–$SiO_x$:H thin films deposited in the work of this thesis were made employing the Technique of Plasma-Enhanced Chemical Vapour Deposition (PECVD), using the equipment AMIGO located in the room CR10000, Else Kooi Laboratory (EKL), of Delft University of Technology. The PECVD method consist of filling a chamber with reactant gases between parallel electrodes, one of them grounded and the other connected to an Radio Frequency (RF) power source. This power excites the reactant gases into a plasma, this plasma provides a part of the energy needed for the gases to undergo a chemical reaction. Within the chamber there is a substrate holding a glass film where on top of it the resulting product of the gases reacted are deposited, this substrate has to be heated uniformly to temperatures between 200 to 400 °C for the reaction to take place. [17]

A simplified schematic of the system used can be seen in Fig. 3.1 in the deposition chamber, one side of the substrate is covered at a time. The system used has different chambers according to the gases to be employed in the reaction, an example of the working configuration is shown in Fig. 3.2, AMIGO differs from the previous schematic on the fact that it has six deposition chambers, named as DPC 1 to 6, and one chamber/cassete to load the substrates.

The main input parameters governing the outcome of this process, are: the substrate temperature; electrode proximity/distance; RF power; reactant gas flow rate; and deposition time.

### 3.2.2. Physical Vapour Deposition

Physical Vapour Deposition works by first obtaining a high vacuum in the chamber where the metal and the substrates are placed, after reaching the desired pressure, it is proceeded to heat up the coating materials, the metal evaporates and as a result of the heat and low pressure, and begins to settle onto the substrate material [84]. By adjusting the heating temperature and process time the deposited

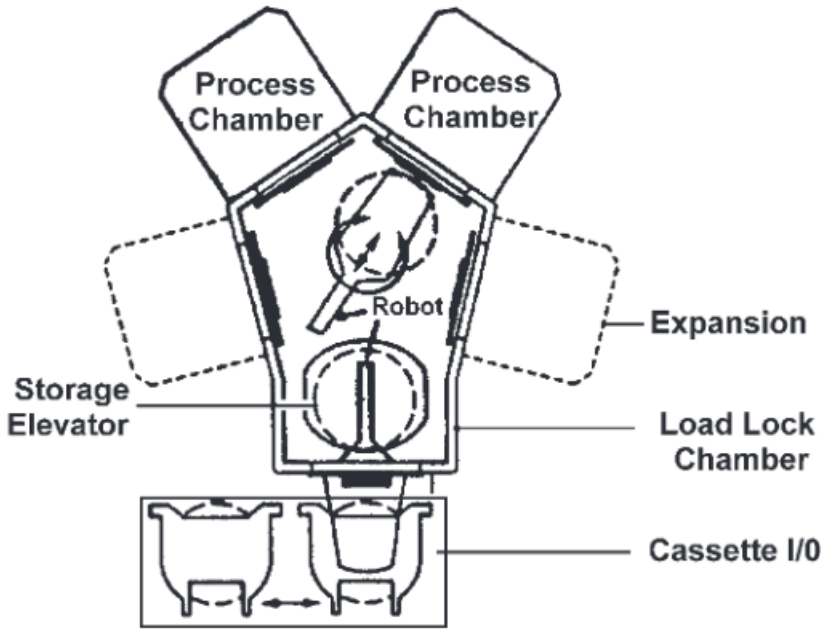


Figure 3.2: Multiple reactor system, similar to AMIGO configuration [17, fig. 7]

thickness can be controlled.

To deposit the contacts in the test solar cells, a metal evaporator is used from the room CR10000 of EKL laboratory in TU Delft, this equipment identified as PRO500S from manufacturer Provac has 4 slots of $10x10\ \mathrm{cm}^2$ to load samples placed in an overhead rotating plate, the materials to be deposited are deposited in a set of ceramic crucibles each containing a different material that can be selected and rotated with the available software, the crucible is heated up by means of high current through it leading to a thermal evaporation, in the specific case of Ag deposition the slot used is different, the Ag pellets are evaporated by means of an electron beam (e-beam) coming from a tungsten filament, In Fig. 3.3 a simplified diagram of the system used can be seen. The metals used in this work are Aluminum (Al), Silver (Ag) and Chromium (Cr). For each solar cell deposition, the contacts are defined within an area of $4x4\ \mathrm{mm}^2$, by using a mask that separates 30 of these areas, within the original cell deposited (total cell area 10*2.5 $\mathrm{cm}^2$).

## 3.3. Characterization of Individual Test Layers

Before being able to make experimental TF solar cells, it is necessary to know both the deposition rate of each type of the doped layers and what is the bandgap of the layers. This section deals with the techniques and equipment used to obtain these values.

### 3.3.1. Spectroscopic Ellipsometry (SE)

Ellipsometry is a technique where the optical properties of a sample material are obtained by means of analyzing a light beam that was reflected on the surface of the sample. it is of special interest to this work because it can accurately measure the thickness of thin films deposited in substrate to the order of $1\text{Å} = 0.1\mathrm{nm}$, and also important optical properties like refractive index or bandgap can be obtained, as long as an appropriate model of a similar material is provided for comparison and fitting. The equipment used for this work is the one showed in Fig. 3.4, it is an spectroscopic ellipsometer

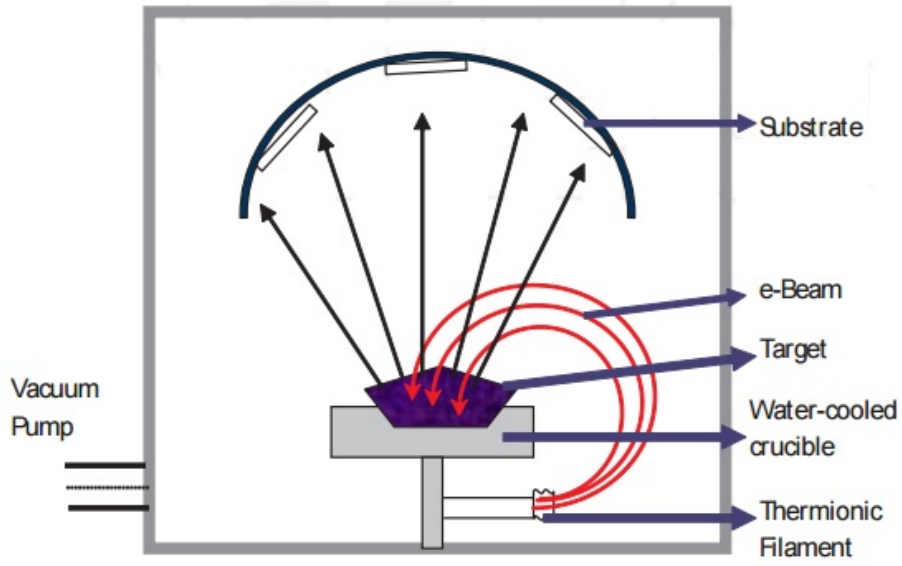


Figure 3.3: Schematic of a Physical Vapour Evaporation Device by e-beam [18, fig. 4]

(SE) made by JA. Wollam Co Inc, model M-2000. The working principle of it will be explained in the following paragraphs.

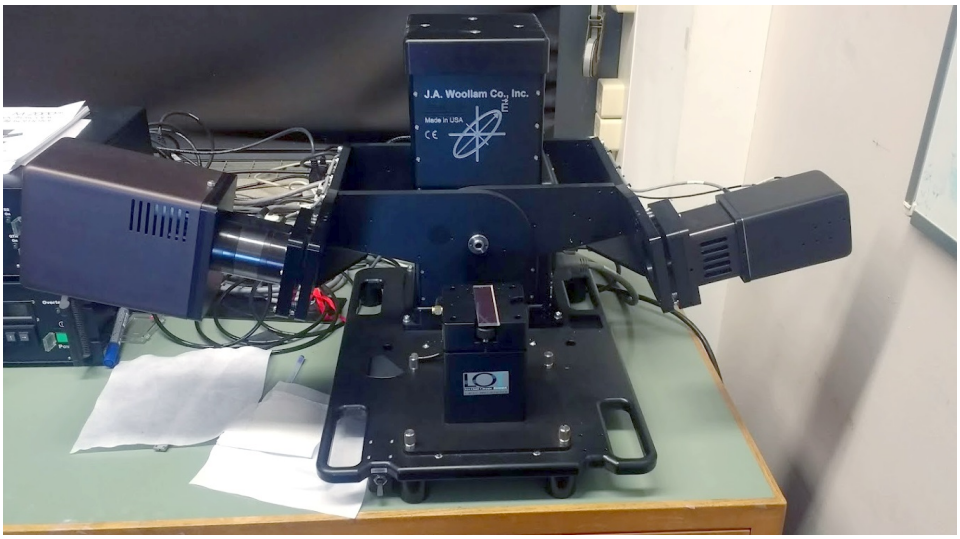


Figure 3.4: SE setup

The way the SE equipment works is by first firing a light beam and having it linearly polarized through a filter, by saying this it means that the light incident travels with an electric and magnetic field in the same phase, this is illustrated in Fig. 3.5. However once the beam is reflected from a media that partially absorbs the light like the material sample, the magnetic and electric field will no longer be in the same phase, the phase displacement and attenuation is directly related to the thickness of the material and the electric vector would go from describing a straight line path, to have an ellipse path [85], this is represented in Fig. 3.6.

These changes observed in the analyzer of the reflected signal are measured in a property called

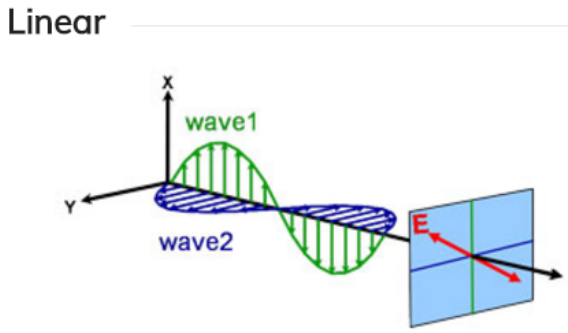


Figure 3.5: Linear Polarization of light[19]

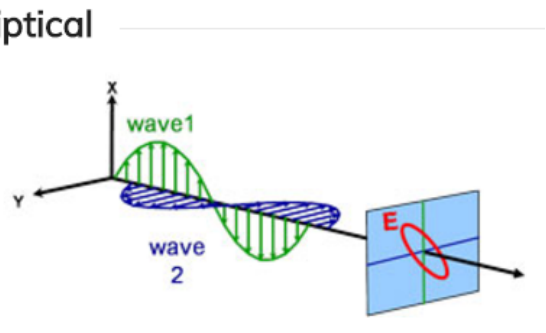


Figure 3.6: Elliptical Polarization of light[19]

complex reflectance ratio ($\rho$) , which is a complex number and has two components $\Delta$ and $\Psi$. $\Delta$ is the phase difference from incoming to reflected ray

$$\Delta = \delta_1 - \delta_2$$

and $\Psi$ relates to the ratio of the reflected signal amplitudes which were attenuated, the basic equation of ellipsometry is shown below:

$$\rho = \frac{\rho_p}{\rho_s} = \tan\Psi \exp(i\Delta)[57, eq.\ 9.8] \tag{3.1}$$

$\rho_p$ and $\rho_s$ refer to the parallel and perpendicular components of the reflected light already normalized with respect to the source signal strength.

The measured values can be fitted to a model of a material with a similar composition to obtain: Film Thickness ($z$), Refractive index ($n$), extinction coefficient ($k$), and other values that are not mentioned here, due to not having relevance for this work.

Both $n$ and $k$ form part as a complex number of the refractive index:

$$\tilde{n} = n + ik$$

Where n is the real part, and k the imaginary one also called the extinction coefficient. both are wavelength dependant ($\lambda$), and $k$ can be used to calculate the absorption coefficient $\alpha$ with Eq. (3.2).

$$\alpha = \frac{4\pi k}{\lambda}[57, eq.\ 4.26] \tag{3.2}$$

$\alpha$ can describe how well a refractive material absorbs light at a certain wavelength in accordance with the following Eq. (3.3):

$$I(z) = I_0 \exp(-\alpha z)[57, eq.\ 4.25] \tag{3.3}$$

Where $I_0$ represents the incident light, $I(z)$ the amount of the light that can pass through the material after reaching the thickness $z$.

### Measuring bandgap with ellipsometry

The ellipsometer can be used to calculate the bandgap, by means of first knowing the absorption coefficient $\alpha$. As the energy of the photon approaches the bandgap, $\alpha$ tends to sharply decrease.

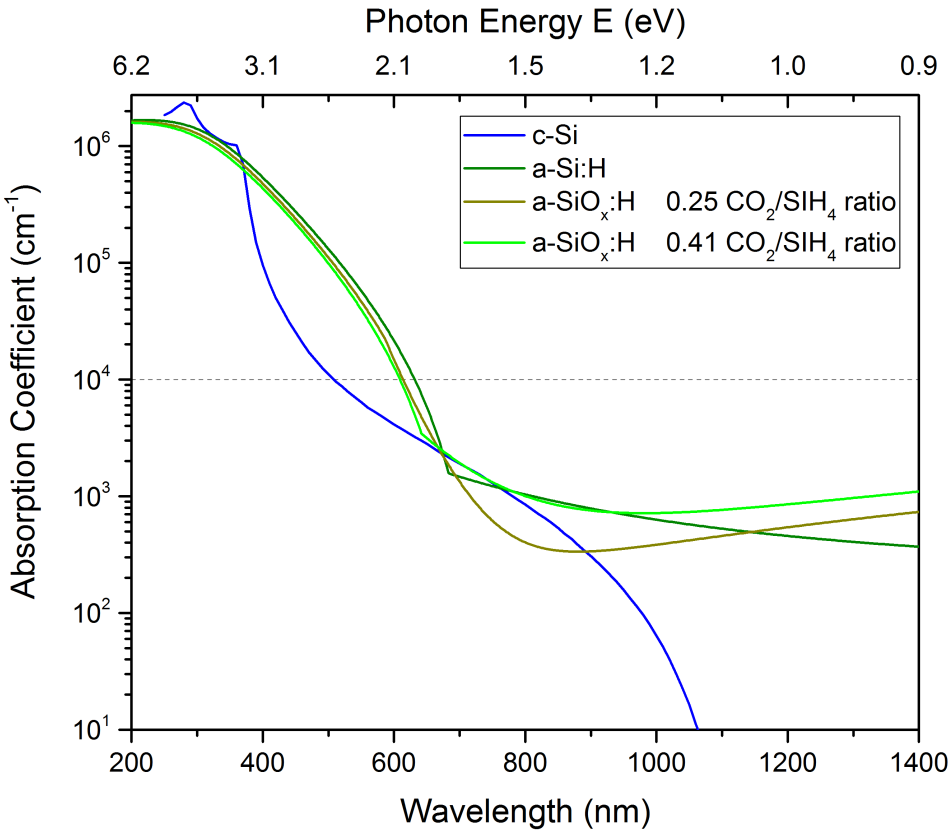


Figure 3.7: Absorption coefficients for c–Si; a–Si:H a–$SiO_x$:H (c–Si values obtained from [20])

Fig. 3.7 shows how this happens for c-Si between 1.1 and 1.2 eV. However, amorphous silicon does not have the same sharp decrease. Because of the presence of defects inherent to the material, a portion of the low energy photons are also trapped but do not contribute significantly to the generation of energy carriers. Therefore a practical criteria has to be used, a well accepted one is to allocate the optical bandgap as the value where ($\alpha$) becomes $10^4$ $\mathrm{cm}^{-1}$ [86].

The line drawn in Fig. 3.7 shows where the optical bandgap $E_{04}$ is located for the a–Si:H and a–$SiO_x$:H . These amorphous silicon results are part of the series of experimental layers made during the course of this work. They are used again during Chapter 4.

## 3.4. Characterization of experimental solar cells

The completed experimental solar cells were measured in terms of their most important electrical parameters, this section describes these parameters and the equipment used. However before talking on the solar cell measurement equipment. Below is given a short introduction on the standardized emission spectrum used in the measurements.

### 3.4.1. Solar Simulator

Solar simulators are machines that try to mimic the electromagnetic emission of the sun in a standard defined condition. These conditions depend on if the sun rays have crossed the atmosphere and the angle of incidence. Fig. 3.8 shows 3 different ways in which the sun rays reach the Earth. AM0 is defined by the ASTM E490 as the spectral irradiance in outer space just before the sun radiation enters the Earth atmosphere. AM 1 means the sun rays have entered the full atmosphere until sea level and

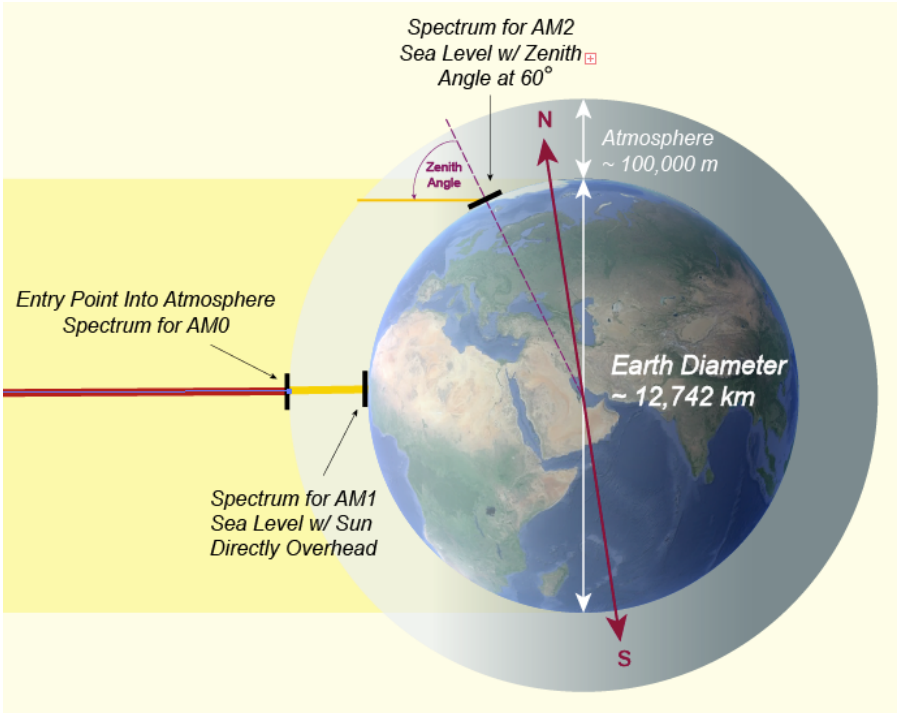


Figure 3.8: Schematic of Angle of Incidence for AM0, AM1, and AM2 [21]

the angle of incidence is perpendicular to Earth. "AM" is defined by the following equation.

$$AM = \frac{1}{\cos(\theta)}$$

Where $\theta$ refers to the angle of incidence of the sun when measured from a line normal to the ground. AM1 therefore corresponds when $\theta$ equals zero. AM2 as depicted in Fig. 3.8 is used to describe the path the sun rays have to take for a zenith angle at 60 degrees.

Fig. 3.9 shows a plot of the Spectral Irradiance versus wavelength for AM0, AM1.5 Global and AM1.5 Direct. The graph show the difference between the spectral irradiance intensity of both standards. AM0 has a total intensity of 1353 $\mathrm{W/m^2}$, while AM1.5 Global has a total intensity of 1000 $\mathrm{W/m^2}$ as stated by ASTM G173-03. The reason for the difference in the two apart from the angle of incidence. Is that a part of the incoming radiation (AM0) gets reflected or is absorbed as it travels the atmosphere.

The solar simulator used in this work complies to the Standard Test Conditions (STC) meaning it gives an AM1.5 spectral response shape, measuring at 25°C. And with a total irradiance of 1000 $\mathrm{W/m^2}$. The simulator is made by Wacom Electro Co. LTD model WXS-156S. The setup for the illumination consist in a continuous type, two lamp system, Xenon (1000W) and Halogen (400W). It matches the AM1.5 spectra quite well as can be seen in Fig. 3.10 from 300 till 1200 nm.

### 3.4.2. Current Density (J) and Voltage (V) measurement

The procedure to use the solar simulator to measure the electrical properties is described in this section. Each sample of solar cell looks similar to the one in Fig. 3.11 and is as described in Section 3.2.2, for each one of the 30 contacts a Current Density (J) vs Voltage (V) measurement array is calculated, for this purpose an in house built accessory is available that has 30 pins matching the area of the test solar cell, (see Fig. 3.12) the data in the output of the software gives the following key external parameters:

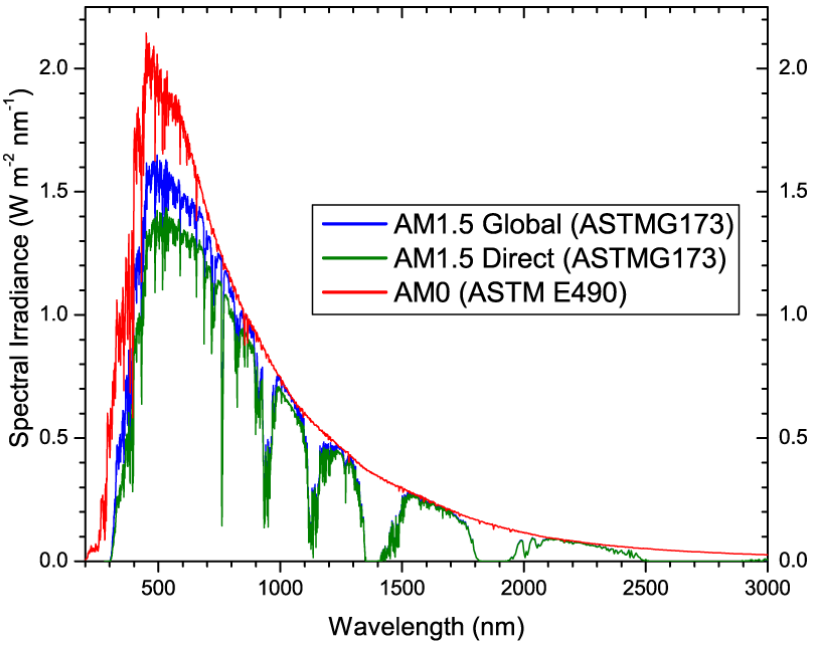


Figure 3.9: Solar Spectra for space and terrestrial use [22]

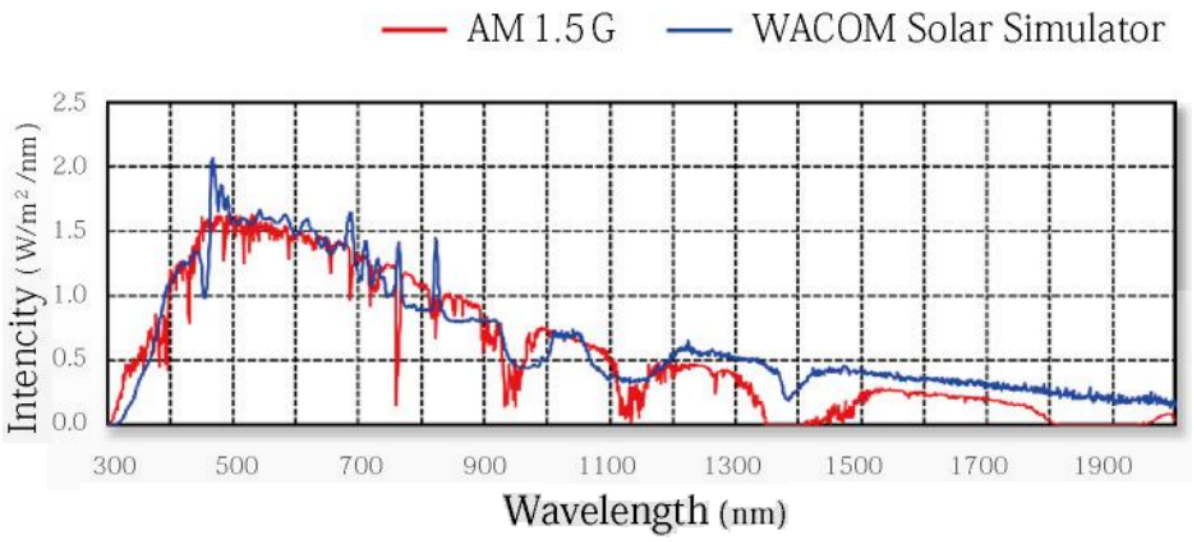


Figure 3.10: AMG1.5 Solar Simulator Spectral Irradiance [23]

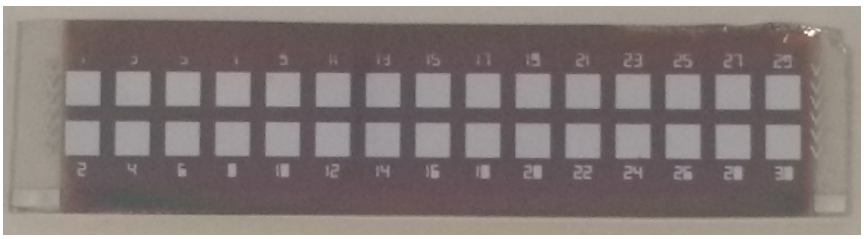

Figure 3.11: Sample of a–$SiO_x$:H thin film cell

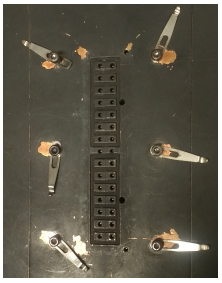

Figure 3.12: In House 30 pin setup

- $J_{sc}$ called short circuit current density represents the maximum current density exhibited by the solar cell, when connected in the short circuit condition (V=0).
- $V_{oc}$ Open Circuit Voltage it is registered at the point where the current is equal to zero.
- FF called fill factor the software calculates it by dividing the maximum power generated by the product of $J_{sc}$*$V_{oc}$
- $R_s$ series resistance this value and the shunt resistance are mostly related to defects during manufacturing of the cell. A big series resistance will reduce the FF and short circuit current, so the smaller it gets the better quality of the cell.[57]
- $R_{sh}$ Shunt resistance also called parallel resistance it is represented in the solar cell as an alternate path for the light generated current to flow, a very small shunt resistance means the current generated is leaked, or also said that the cell is ”shorted”. Performance wise $R_{sh}$ the bigger it gets the better the performance of the solar cell
- $V_{mpp}$ and $J_{mpp}$ are voltage and current at the maximum power point when multiplied together with the illuminated area they give the maximum power that can be obtained from the solar cell.

A typical Current vs Voltage (I-V) curve is shown in Fig. 3.13, this figure helps to point where the previous parameters discussed are placed. To transform this plot into a Current Density vs Voltage (J-V) curve it is only necessary to divide the current by the illuminated area.

Current measurements performed by the solar simulator, need to be corrected because there is a slight spectral mismatch between the solar simulator output and the AM1.5 standard solar spectra. The mismatch can be understood by looking at Fig. 3.10. Using external quantum efficiency it is possible to arrive at a more accurate value for the $J_{SC}$ and correct for the spectral mismatch, as it will be explained in the next section.

### 3.4.3. External Quantum Efficiency (EQE)

External Quantum Efficiency (EQE) is the ratio between how many photons reach a photovoltaic device surface, and how many electron-hole pairs are generated and collected (also called $I_{ph}$).

The EQE is measured by using a home built setup, first a calibrated sensor with a known EQE response is illuminated by a Xenon light source passed through a monochromator and a chopper to get a specific wavelength of light that is changed in steps of 10 nm. This gives a measurement of a photocurrent $I_{sc}$, which is divided by the product of the known EQE and the electron charge to obtain the photon flux dependant on the wavelength as can be seen in Eq. (3.4).

$$\Psi_{ph,\lambda} = \frac{I_{ph}^{ref}(\lambda)}{qEQE^{ref}(\lambda)} [57, eq.\ 9.8] \tag{3.4}$$

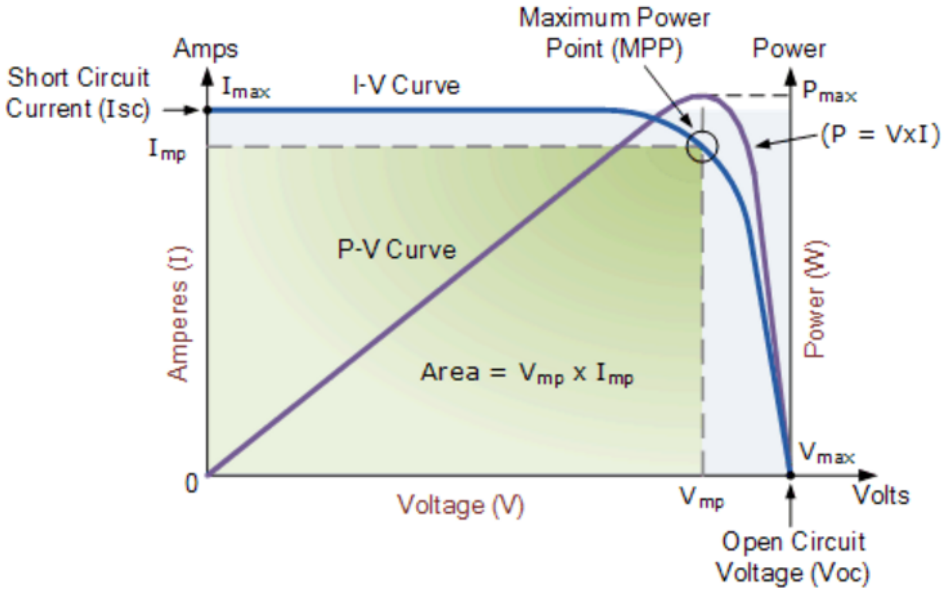


Figure 3.13: Solar Cell I-V Characteristic Curve [24]

After the previous calibration step is completed the solar cell is mounted, one of the 30 dots of 4×4 $mm^2$ in area is selected to be measured. This cell receives the now calibrated light beam, and again by illuminating at steps of 10 nm the cell it can be obtained the EQE response by rearranging Eq. (3.4). The total short circuit current $J_{sc}$ is calculated as shown in Eq. (3.5) where the product of the wavelength dependant photon flux, and EQE is integrated per the wavelenght range used (for the purpose of this work from 300nm to 1200nm) and then multiplied by the electron charge.

$$J_{sc} = -q \int_{\lambda\, begin}^{\lambda\, end} \Psi_{ph,\lambda} * EQE(\lambda)_{cell} * d\lambda [57, eq.\ 9.10] \tag{3.5}$$

For illustrative purposes the in house built available EQE setup is showed in Fig. 3.14.

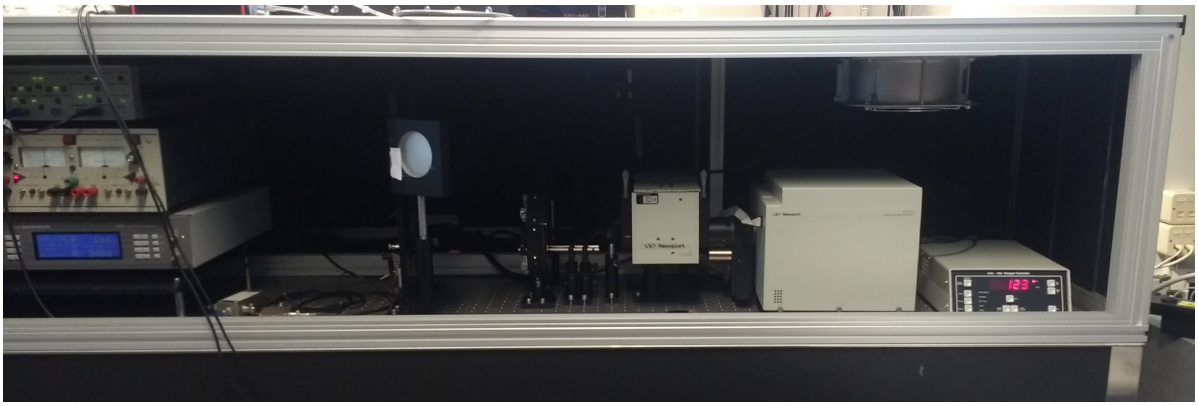

Figure 3.14: EQE setup

### 3.4.4. Data Processing

As explained in Section 3.4.2 Wacom setup, measures in one sweep the electrical properties of the 30 isolated cell areas. During the measurements it was seen that several of the experimental cells do not have homogeneous results across the 30 isolated cell areas, some cell areas were performing quite well; others were acceptable and there were also cases of cell areas that did not work. This made necessary to establish a method to equally evaluate the performance of all the experimental cells.

The method is as follows: out of the 30 cells measured by Wacom setup, the results of the 5 best performing in $\eta(\%)$, were averaged, from this average the values of $V_{OC}$ and FF representing the experimental cell are taken. The error margin for the samples was taken by means of obtaining the standard deviation ($\sigma$) of the best 5 performing cells. One standard deviation was used as equal to the error margin when presenting the results.

To select the value that represents the $J_{SC}$ of the experimental cell. What was done is to measure the $J_{SC}$ of the best performing cell area (in $\eta\%$ as defined by Wacom setup measurement) using the EQE setup as explained in Section 3.4.3.

Using these 3 values $J_{SC}$ , $V_{OC}$ and FF the efficiency $\eta\%$ is then calculated by using the following formula:

$$\eta\% = \frac{V_{OC} \times FF \times J_{SC}}{1000 \frac{W}{m^2}} \times 100\% \tag{3.6}$$

For the specific case of $\eta\%$, the error margin was obtained taking into account the propagation of error. Eq. (3.7) is adapted from the theory found in [87]. In this equation the three ($\sigma$) of the parameters used to calculate $\eta\%$, are combined to give the standard deviation of the efficiency ($\sigma_{\eta\%}$). This value is used as the margin error for $\eta\%$.

$$\sigma_{\eta\%} = \eta\% \sqrt{\left(\frac{\sigma_{V_{OC}}}{V_{OC}}\right)^2 + \left(\frac{\sigma_{FF}}{FF}\right)^2 + \left(\frac{\sigma_{J_{SC}}}{J_{SC}}\right)^2} \tag{3.7}$$

# 4

# Grading Method

## 4.1. Introduction

In this chapter it will be explained the method developed to achieve an absorber intrinsic layer of a–$SiO_x$:H where across the total thickness, the bandgap of the material can be varied by adjusting the amount of $CO_2$ gas flow employed to deposit the layer. The basic theory lies in going from using the optical bandgap exhibited by a layer of a-Si:H and by means of incorporating a flow of $CO_2$ at different ratios of the total gas flow to achieve a material with a higher bandgap. The structure of this chapter starts by explaining first the parameters used when depositing the a–$SiO_x$:H intrinsic layers. Then it will be shown how the deposition rate ($v_{dep}$) and the bandgap ($E_{04}$), vary when depositing layers with different $CO_2/SIH_4$ gas flow ratio ($r_{CO_2}$). The next section explains how the relationship between $r_{CO_2}$, $v_{dep}$ and $E_{04}$ can be used together with a polynomial fitted equation. To calculate at what time and with what $r_{CO_2}$, a layer has to be deposited to have a desired $E_{04}$ and thickness. The last section gives a procedural example on how to deposit a graded absorber layer, using the tools developed during the chapter.

The deposition parameters for the intrinsic a–$SiO_x$:H layer are based on previous research made by Kim *et al.* [83], [88], and Guijit [89]. The substrate used for the test layer was Corning Eagle XG glass. This substrate was prepared like it is explained in Section 3.1.1. The deposition conditions all test layer share are: RF power density of 21 mW/cm$^2$, with an effective area of 12×12 cm$^2$, meaning the total power used was aproximately 3 W; chamber pressure was 2 mbar. The variation of $r_{CO_2}$ was done with one condition placed, the total gas flow of $CO_2$ and $SIH_4$ always had to add up to 10 sccm (standard cubic centimeters per minute). The samples were subdivided in two series, one was made at 200°C and another series was deposited at 300°C.

## 4.2. Deposition rate and bandgap dependance on $CO_2/SIH_4$ ratio

As reported by Kim *et al.* [88]. It is known the bandgap of a–$SiO_x$:H is strongly dependant on the amount of $CO_2$ flow. It is also known that for a–$SiO_x$:H with different values of $r_{CO_2}$, the velocity at which the material is deposited in the substrate $v_{dep}$ also changes. Therefore the first step made was to determine how $v_{dep}$ varied when changing $r_{CO_2}$. For this purpose samples at 200°C and 300°C, were prepared with increasing values of $r_{CO_2}$, from 0 till 1.63.

The thickness of each test layer was measured with the method described in Section 3.3.1. The results obtained for the thickness were divided by the deposition time (2400 s) to get the deposition rate.

Fig. 4.1 shows how the deposition rate varies as the $CO_2/SiH_4$ ratio increases. As it can be observed, a bigger proportion of $CO_2$ leads to a slower deposition rate. This means that a cell deposited with a higher ratio $r_{CO_2}$, will need more time to achieve the same thickness as one deposited at a lower $r_{CO_2}$. Also it was seen that cells deposited at the same $r_{CO_2}$, but at a higher temperature (300°) had a slightly faster $\nu_{dep}$. The dashed lines in Fig. 4.1 are curves fitting the trend of the data. They were made using Origin Lab software with a base equation of the type of polynomial second order in the shape

$$y = B1x + B2x^2 + C$$

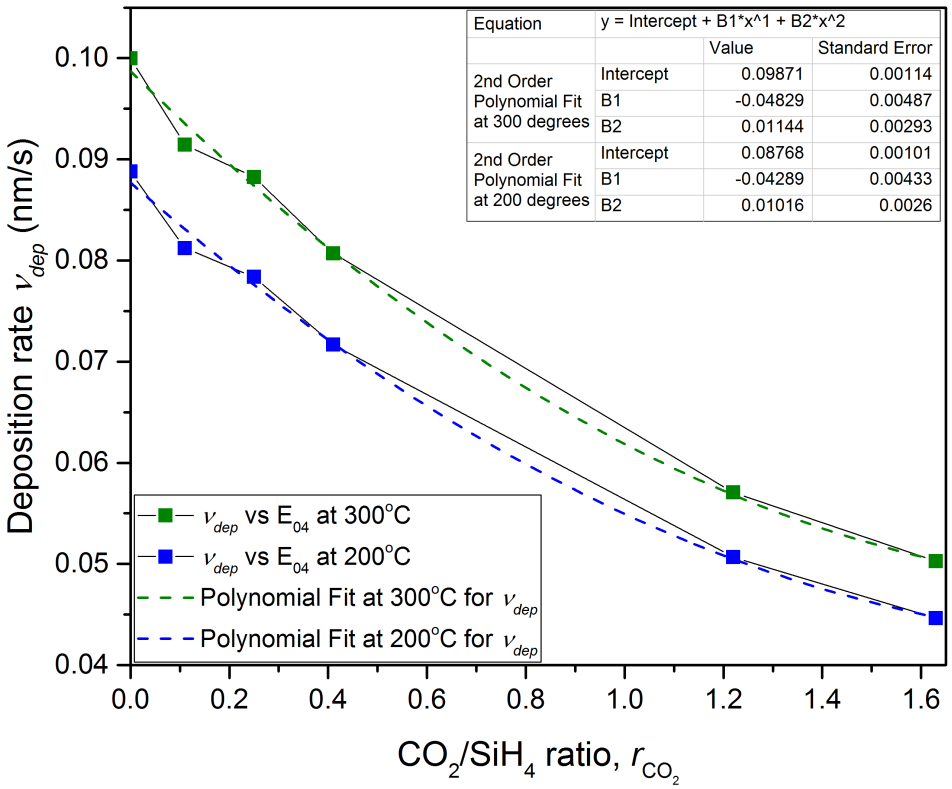


Figure 4.1: Comparison at 300°C and 200°C of Deposition ratio ($\nu_{dep}$) vs $CO_2/SiH_4$ ratio $r_{CO_2}$.

The polynomial fitted equations are used later in this chapter to calculate $\nu_{dep}$ when $r_{CO_2}$ is known. Embedded into Fig. 4.1 are the coefficient values for the fitted equations. From these values Eq. (4.1) is presented for 300°C samples; and Eq. (4.2) is presented for 200°C samples.

$$\nu_{dep} = 0.0987 - 0.0483 r_{CO_2} + 0.0114 r_{CO_2}^2 \tag{4.1}$$

$$\nu_{dep} = 0.0877 - 0.0429 r_{CO_2} + 0.0102 r_{CO_2}^2 \tag{4.2}$$

Afterwards it was necessary to determine how the bandgap $E_{04}$ varies when the deposition rate $r_{CO_2}$ changes. Also in this case test layers at 200°C and 300°C were prepared, with the same values of $r_{CO_2}$ as previously used.

The bandgap of each test layer was measured with the method described in Section 3.3.1. Fig. 4.2 shows how the $CO_2/SiH_4$ ratio varies as the optical bandgap increases. The reason to display the data in this way is because the method devised to make a graded bandgap region, starts with $E_{04}$ as a know desired quantity, and the rest of variables are calculated from it. As it can be observed in

Fig. 4.2. Increasing $r_{CO_2}$ will also increase $E_{04}$. And overall, samples deposited at 200 °will have a bandgap slightly bigger (0.01 to 0.03 eV) than samples deposited at 300°C (when no other deposition parameter is varied). In the same way as was done with the previous plot, the dashed lines in Fig. 4.2 are curves fitting the trend of the data.

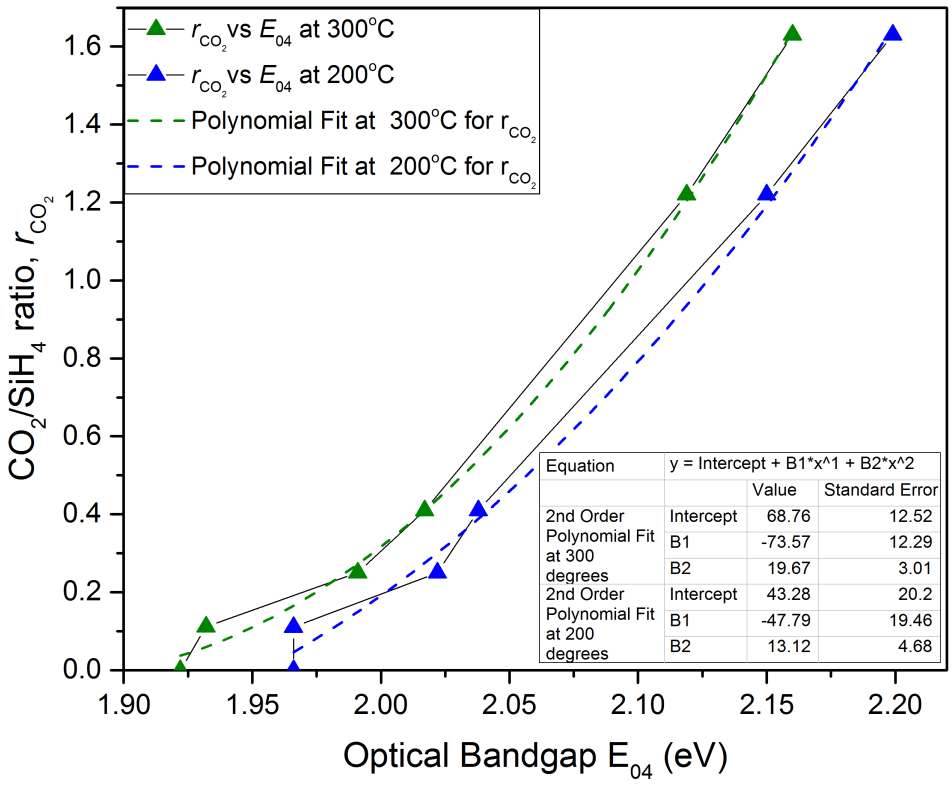


| Equation | | y = Intercept + B1*x^1 + B2*x^2 | |
|---|---|---|---|
| | | Value | Standard Error |
| 2nd Order Polynomial Fit at 300 degrees | Intercept | 68.76 | 12.52 |
| | B1 | -73.57 | 12.29 |
| | B2 | 19.67 | 3.01 |
| 2nd Order Polynomial Fit at 200 degrees | Intercept | 43.28 | 20.2 |
| | B1 | -47.79 | 19.46 |
| | B2 | 13.12 | 4.68 |

Figure 4.2: $CO_2/SiH_4$ ratio vs Optical Bandgap $E_{04}$ for test series at 200°C and 3W power

The polynomial fitted equations are used later in this chapter to calculate $r_{CO_2}$ as a function of a desired and known $E_{04}$. Embedded into Fig. 4.2 are the coefficient values for the fitted equations. From these values Eq. (4.3) is presented for 300°C samples; and Eq. (4.4) is presented for 200°C samples.

$$r_{CO_2} = 68.76 - 73.57E_{04} + 19.67E_{04}^2 \tag{4.3}$$

$$r_{CO_2} = 43.28 - 47.79E_{04} + 13.12E_{04}^2 \tag{4.4}$$

## 4.3. Making of a layer with a graded bandgap

During the test depositions described in the previous section it was seen that the optical bandgap of a–$SiO_x$:H layers could be varied from the value when not having any oxygen in its composition (1.96 eV) to a value close to around 2.2 (eV),

In a regular solar p-i-n solar cell with a–$SiO_x$:H as the intrinsic (i) absorber layer. the bandgap of the absorber layer is kept constant trough the entirety of its composition by having a fixed $CO_2/SiH_4$ gas flow ratio, in this section an example is provided on how to design a intrinsic absorber layer where across the total thickness there are regions with varying bandgap and with a constant bandgap.

The example consist on a absorber layer of a total thickness of 200nm, having 3 regions, the regions

are numbered by the order in which the light would pass through it. The first region, the one called p-i region is attached to the p layer and buffer, and will have in this example a thickness of 30 nm. The bandgap is designed to vary from 2.1 eV at start, to the lower value of the bandgap possible 1.96 eV during a distance of 30nm, in a linear progression. Then it follows the second region, in the example it will have 110 nm and a constant bandgap of 1.96 eV. This region stops at a thickness of 140nm (30nm 1st region + 110 nm 2nd region). The third region, also called the i-n region, starts having a bandgap of 1.96 ev with a linear progression for the bandgap during 60 nm until reaching 2.1 eV, when the intrinsic layer ends. This configuration is represented in Fig. 4.3.

While the progression of the grading is aimed at being linear, during deposition this has to be approached in a way that suits the capabilities of the deposition chamber, the way to approach the bandgap grading is to divide the grading length in 10 nm steps, and in each one change the bandgap to an equal amount so that the amount of length for the different graded areas is equal, as can be seen in Fig. 4.4.

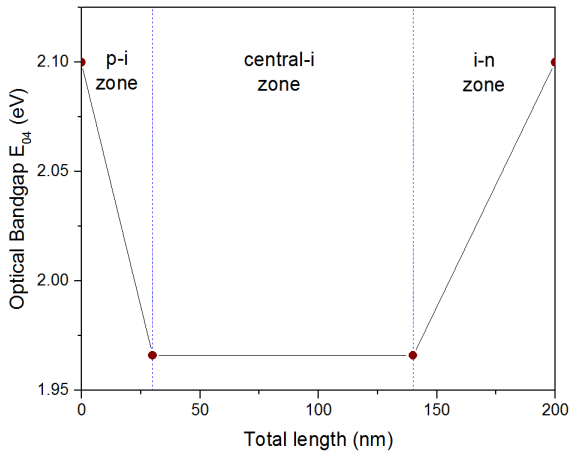


Figure 4.3: Example of designed grading for the intrinsic layer bandgap, using a configuration of 30p-i. 110 mid-i, 60 i-n

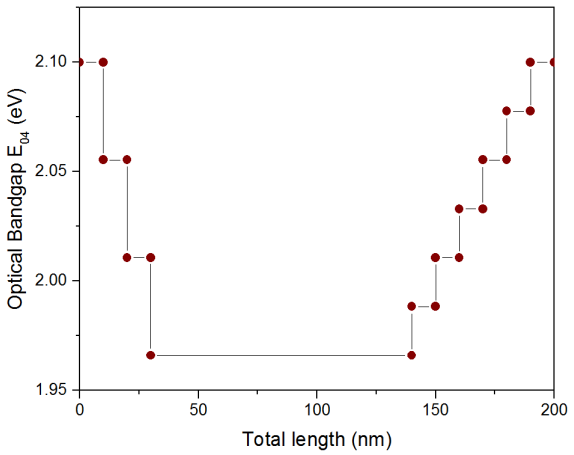


Figure 4.4: Real deposition behaviour using 10nm steps during grading

Each bandgap step has a different flow ratio needed, and also a different deposition rate. Therefore several parameters need to be calculated to make an accurate deposition. To explain the calculation step Table A.1 is provided. It contains the calculations made for an example grading made at 200°C. The second row in Table A.1 is written in bold letters because this grading step is used to go over the calculation steps.

1. From the bandgap range (i.e 1.966eV to 2.1eV) and number of steps (30nm divided by 10nm =3 steps) obtain the bandgap step.

$$Eg_{step} = Eg_{previous\ step} - \frac{Eg_{up} - Eg_{down}}{number\ of\ steps} = 2.1 - \frac{2.1 - 1.966}{3} = 2.055\,\text{eV}$$

2. Use Eq. (4.4) with $Eg_{step}$ as $(E_{04} = 2.055)$ to obtain $r_{CO_2}$.

$$r_{CO_2} = 13.12(2.055^2) - 47.79(2.055) + 43.28 = 0.48$$

3. Use Eq. (4.2) with $r_{CO_2} = 0.48$ to obtain $v_{dep}$.

$$v_{dep} = 0.0102(0.48^2) - 0.0429(0.48) + 0.0877 = 0.069\,\text{nm} * \text{s}^{-1}$$

4. Calculate the deposition time from $v_{dep}$ and the thickness desired.

$$Deposition\ time = \frac{Thickness}{v_{dep}} = \frac{10\text{nm}}{0.069\,\text{nm} * \text{s}^{-1}} = 145\,\text{s}$$

5. Finally the individual gas flow rates can be calculated from $r_{CO_2}$. Since it is know that the sum of both $SiH_4$ and $CO_2$ flows is always 10 sccm.

$$\mathrm{SiH_4}\, feed = \frac{10\,\mathrm{sccm}}{r_{CO_2} + 1} = \frac{10\,\mathrm{sccm}}{0.49 + 1} = 6.7\,\mathrm{sccm}$$

$$\mathrm{CO_2}\, feed = 10 - \mathrm{SiH_4}\, feed = 10 - 6.7 = 3.3\,\mathrm{sccm}$$

The rest of the bandgap profile steps are calculated in a similar way with two exceptions, the 4th row of Table A.1 is the mid-i zone where the $CO_2$ gas feed is equal to zero, and from the 5th row and onward where the bandgap is increasing and therefore the bandgap step is being added this time around instead of subtracted.

# 5

# Graded Bandgap Solar cells

## 5.1. Introduction

After the grading method has been established. This chapter will describe the experiments done using this method. The objective for these experiments is to explore how a graded variation of the oxygen concentration in the intrinsic absorber layer and thus on the bandgap, affects the solar cell performance.

The structure of this chapter begins by explaining the past research that involved bandgap grading in solar cell technologies. Enumerating what were the most promising techniques, and the common agreements among different researchers. Then the experimental procedures will be explained. Starting with how the reference cell **without bandgap grading** was made, detailing the structure of the cell and the deposition parameters. Next it will be described the variations and configurations when designing the bandgap graded experimental cells. After this solar cell results will be presented for the reference cell, and for the experimental cells. Finally another section is presented to explain the phenomena seen on the variation of the yield of working solar cell areas for each bandgap configuration.

Grading in a solar cell means that in one of the layers a material property is varied continuously in concentration in order to achieve a different performance. This section gives a background on what research has been done for bandgap grading on thin film solar cells from early 1970's till present days.

One of the earlier attempts to produce a semiconductor with a graded bandgap comes from 1975. Konagai and Takahashi [25] at Tokyo Institute of Technology presented a work related to GaAs solar cells. They reported that one of the limiting aspects to improve the efficiency in this type of solar cells was the high surface recombination velocity of GaAs (around S=$10^6$ - $10^7$ cm/s). The device proposed was a $p$–$Ga_{1-x}Al_xAs$/$n$–GaAs where in the front of the device the ratio of Al to Ga was increased to make the bandgap higher towards the surface. The study theorized that the effect of the surface recombination could be minimized, and the efficiency at shorter wavelengths increased, if a bigger electrical drift field was introduced as it was done with the bandgap grading from 1.73 eV to 1.43. A solar cell using the grading was published having 14% efficiency. A diagram of the band structure is shown in Fig. 5.1.

Another early technology that used bandgap grading was published in 1986 [26]. This solar cell was an a–Si:H solar cell that had a p-i-n structure with amorphous silicon carbide as the front p layer, and intrinsic a–Si:H as the absorber i layer. This device incorporated an interface layer of 10 nm between the p and i layer, Fig. 5.2 shows how the p-i interface is placed. Across the 10 nm length the silane/methane ratio used during deposition was linearly graded, to smoothly go from the bandgap of a-$SiC_x$:H to the bandgap of pure a–Si:H. In the same report experimental cells results were presented, reporting an improvement of all external parameters over cells without the graded interface, and obtaining also a gain in efficiency from non graded cells of 7% to 8.2% for cells having the grading.

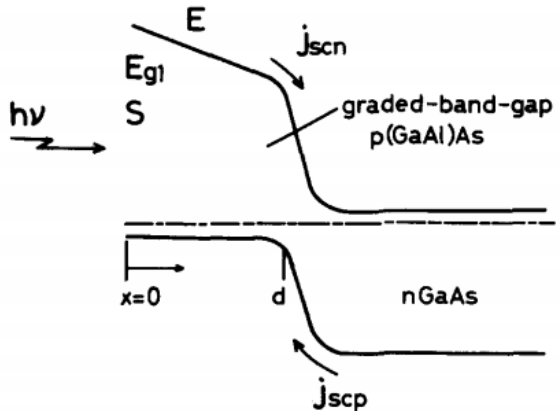


Figure 5.1: Structure of a graded bandgap GaAs solar cell $E_{g1}$ =1.73 eV [25]

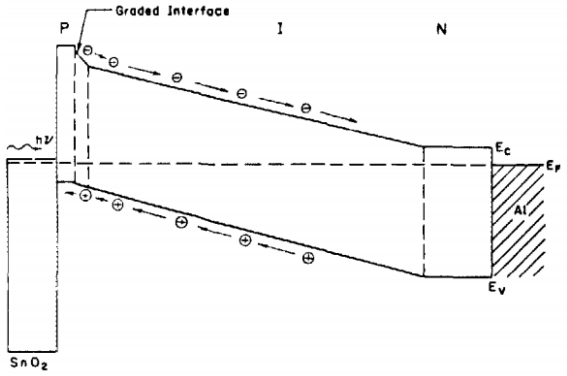


Figure 5.2: Simplified energy band-diagram of an a–Si:H p-i-n solar cell with a graded interface layer[26]

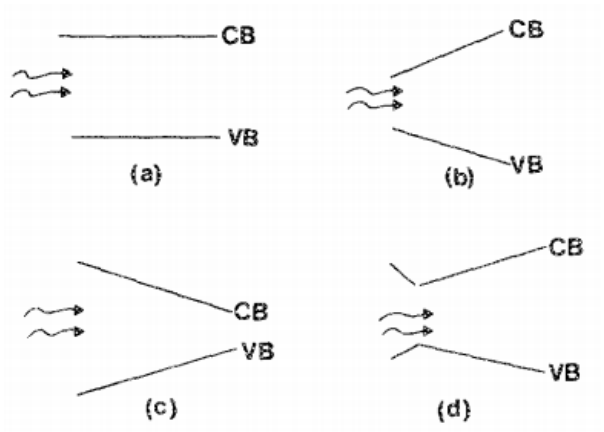


Figure 5.3: Bandgap profiling for the cases of: (a) no profiling, (b) normal profiling, (c) reverse profiling, and (d) double profiling.[27]

Grading of the bandgap became an interesting research topic, because it was an relatively inexpensive way to obtain an additional gain, using already available manufacturing technologies. In 1989 and 1990 two important papers [27][90] were published in the graded bandgap topic. In the two works mentioned, a numerical modeling tool for a-Si:H alloy solar cells was devised. For the specific case of an intrinsic a–$SiGe_x$:H absorbing layer, the bandgap of the intrinsic layer could be varied depending on the amount of Ge alloyed. Increasing the Ge content in the layer reduces its bandgap. Three scenarios were proposed to model the intrinsic layer, while varying the bandgap: a normal profile (from 1.52 eV bandgap from front receiving layer to 1.71 eV bandgap at the back of i layer); a reverse profile (from high $E_g$ to low $E_g$); and a combination called double profiling (called later in literature as V shape); where the bandgap starts as a reverse profile for a short length and then becomes a normal profile until the end of the i layer. These 3 bandgap profiles can be seen in Fig. 5.3. The computing model predicted that for illumination under red light, cell performance of a constant bandgap cell (1.52 eV) could be improved using the grading profiles described previously. A higher $J_{SC}$ and FF under normal profiling would be obtained; and a higher $V_{OC}$ for reverse profiling would be achieved. Experimental results from the same research supported the calculated model predictions.

Fine tuning of the bandgap profiling for a–SiGe:H was done later. Van Swaaij *et al.* [91] showed the effects of the grading width length, for the p-i regions and i-n regions. Using both computer simulation and experimental results. The work concluded that when designing bandgap grading a very small p-i graded region is needed to improve $J_{SC}$ and $V_{OC}$ while making the i-n graded region length as big as possible increased all external parameters. Other works regarding grading optimization in a–SiGe:H

also had a similar conclusion, or build forward upon this premise [28].

About why these effects are seen with the grading, different theories have been presented. Like for example that a narrowing bandgap profile, decreases recombination of minority carriers of holes at the p-i interface, resulting in enhanced carrier collection [90][92]. Other authors state that the $J_{SC}$ decreases when the grading profile introduces more material of a higher bandgap, modifying the average bandgap of the solar cell [30]. However it cannot be stated the effect is fully understood. Lundszien *et al.* [93] [94] presented experimental results where using a buffer layer with an intermediate step of constant bandgap between the p and i layer, would have similar results to a graded profile of U shape. and also that if the bandgap grading slope was designed in reverse, the improvement of $V_{OC}$ ,$J_{SC}$ and FF also remained.

Other ways to improve the bandgap profile have been proposed, like in computer models shown in [28]. In this work two ways of bandgap profiling are mentioned, one having a flat constant bandgap region, and another one claiming to have a better performance by having regions with different grading slopes. In Fig. 5.4 the two mentioned profiles can be seen. Other works proposing a different approach to grading show an exponential grading slope as used in [29] and depicted in Fig. 5.5. Going forward, more recent research [30], presented an experimental cell using a UV shape as can be seen in Fig. 5.6, the results state the UV shape to have better efficiency than V or U shape cells. This approach closely resembles what was proposed by [28].

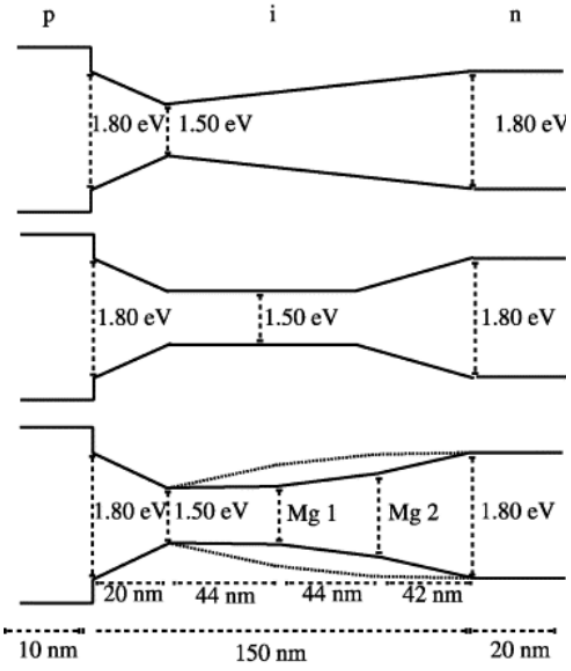


Figure 5.4: Top: V type profile. Middle: U type profile. Bottom: profile design for optimization. Mg1 and Mg2 were varied independently between 1.5 and 1.80 eV in steps of 0.05 eV. [28]

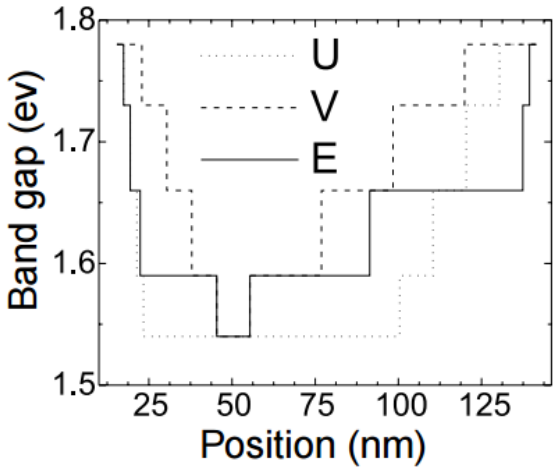


Figure 5.5: Schematic i-layer band gap profiling of the 'U-shape', 'V-shape' and 'E-shape' structures, without buffer layers. [29]

Graded bandgap research has also benefited other types of thin film technologies, since there have been research efforts trying to use it. For example in 2001, for $Cu(In,Ga)Se_2$ solar cells a research work using bandgap grading was presented [95]. The solar cell had an absorber layer of CuInSe, the way to tune the bandgap was by controlling the Ga/In ratio or the S/Se ratio, as either of them is increased the bandgap also goes up. The grading used in this research resembled a V shape, and it showed a variation of performance according to different configurations of 4% in efficiency. The benefits of grading that are predicted by other works go up to 3% [96]. However there is a discrepancy with numerical models as they only showed around 1% efficiency of predicted gain [97]. Seeing the benefits this type of modification can bring to the performance of TF solar cells. It is also interesting then, to explore the effects bandgap graded design will have for solar cells based on a–$SiO_x$:H technology.

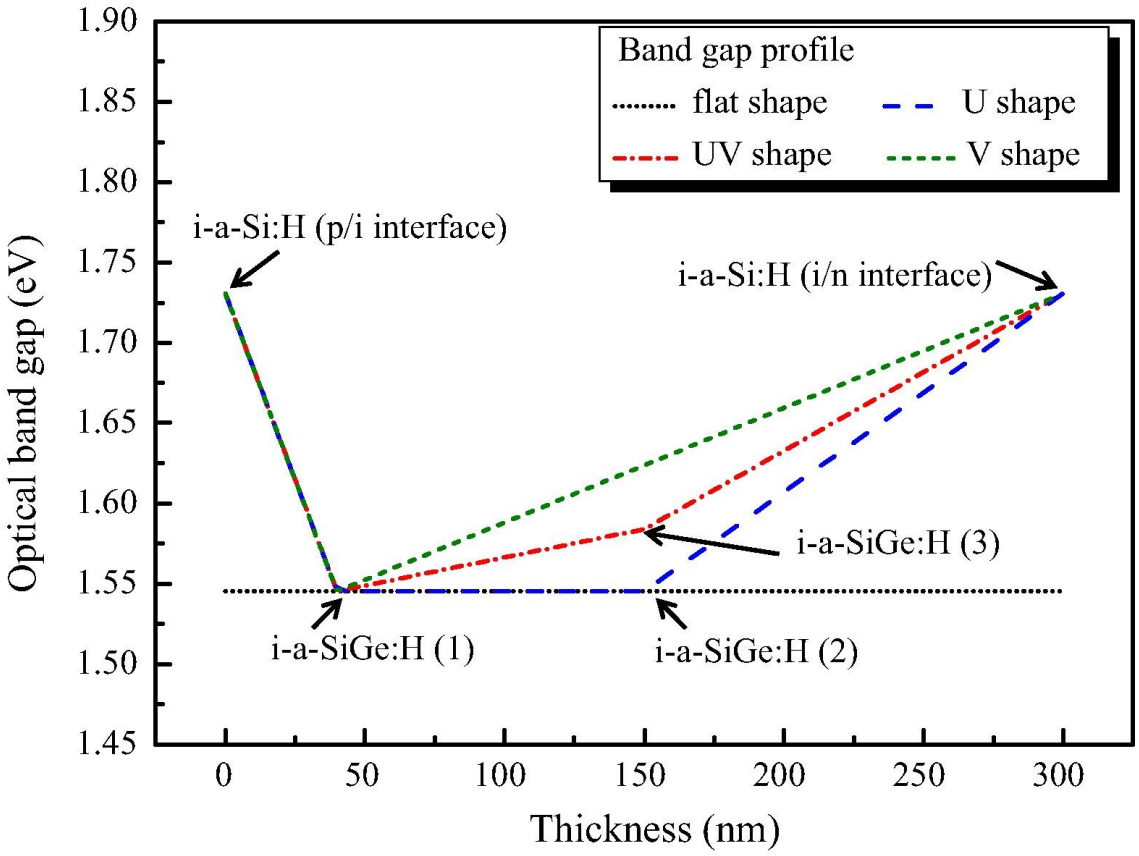


Figure 5.6: Plot of the optical band gap profile for the i-a-SiGe:H films, showing three different bandgap profiles. [30]

## 5.2. Experimental Section

This section explains the deposition parameters for the amorphous silicon oxide solar cells. The basic structure of the solar cells deposited in this work. How the two reference cells differ from each other. The different configurations that were made on the experimental cells when compared to reference cell parameters, and finally what were the bandgap grading configurations for the experimental cells. The subsection that follows describes in detail the reference cell structure and deposition parameters.

### 5.2.1. Reference a–$SiO_x$:H Solar Cell

Before trying to produce a solar cell with a graded bandgap. It was necessary to first obtain a good reference cell based in a–$SiO_x$:H technology, so the effects of grading could be properly assessed. The reference cell here presented is based on the research published by Kim *et al.*[88] [83] and Guijt [89]. The structure of the cell starts with a substrate of Asahi VU glass. Over this material a layer of ZnO:Al is sputtered at 300 °C, this ZnO:Al serves as a protection for the $SnO_2$:F conductive coating present in the Asahi VU glass. The next step of the process is the deposition of a a p-i-n solar cell structure. The layers are mentioned in the order they are deposited: p-nc–Si:H seed (5nm)/ p-a–$SiO_x$:H (7nm) / i-a–$SiO_x$:H buffer/ i-a–$SiO_x$:H absorber (200nm)/ n-nc–Si:H buffer (5nm)/ n-nc–$SiO_x$:H (100nm). The metal contact was deposited using the technique described in Section 3.2.2 and it was composed of 150 nm Ag/30 nm Cr/300 Al. The deposition parameters, including gas flows, RF power pressure and temperature for the p-i-n layer are enlisted in Table 5.1.

Table 5.1: Deposition Conditions for the Reference cell

| Layer | $f_{SiH_4}$ (sccm) | $f_{H_2}$ (sccm) | $f_{CO2}$ (sccm) | $f_{B_2H_6}$ (sccm) | $f^*_{PH_3}$ (sccm) | Power RF (W) | Power RF (mW/cm$^2$) | Pressure (mbar) | Temperature (°C) |
|---|---|---|---|---|---|---|---|---|---|
| p-nc–Si | 1.5 | 200 | – | 30** | – | 50 | 347 | 2.5 | 300 |
| p-a–SiOx:H | 20 | 20 | 45 | 2 | – | 5 | 35 | 0.7 | 300 |
| i-a–SiOx:H | 2.5 | 200 | 2.5 | – | – | 6 | 42 | 2.6 | 200/300 |
| i-a–SiOx:H | 8 | 200 | 2 | – | – | 3 | 21 | 2 | 200/300 |
| n-nc–Si:H | 1 | 100 | – | – | 1.2 | 10 | 69 | 1.5 | 300 |
| n-nc–SiOx:H | 1 | 100 | 2 | – | 1.2 | 10 | 69 | 1.5 | 300 |

*2% in $H_2$ gas flow, **200 ppm in $H_2$ gas flow.

Table 5.1 mentions two types of temperature for the i–a–$SiO_x$:H layer. This is because two types of reference cell were made. Identical in all senses, except that one sample was made with the deposition chamber at a temperature of 200°C and the other at 300°C.

### 5.2.2. Experimental Solar Cell description

Since there is not yet another research reference on bandgap grading done on a single junction cell with a–$SiO_x$:H . It was then necessary to look at previous literature for a starting point for bandgap grading. Developing on what has worked for other TF solar cells. In Section 5.1 it was seen that for a-$SiGe_x$:H solar cells, several pieces of research coincide on how a small width bandgap graded region designed between the p and the i layer was beneficial to the performance of the solar cell. This grading done on the called p-i region varied in width among the different pieces of research, but it always had a width between 5 to 25% of the total absorber thickness. A similar approach is used as a starting point, for the grading of the a–$SiO_x$:H experimental cells.

The grading was subdivided in 3 regions in the same way as it was explained in Section 4.3. For these 3 regions the bandgap of the central i–region was always kept at 1.96 eV, the bandgap of the p-i region always started at 2.1 eV and the bandgap for the i-n region always ended at 2.1 eV. All the variations on the bandgap through the layer length, (here on after called ”grading”) for the different experimental cells follow this grading on the initial and final values of the bandgap of each area. The

variations on each experimental cell are only about each region length but always keeping the total length at 200 nm, like in the reference cell. The first series of experiments consists on samples where the p-i region was kept relatively small, fixed at a length of 30 nm while the middle i and i-n region length were varied. Two series of experimental cells were made by keeping the p-i region at 30nm. One set was made at 200°C; varying the i-n grading width from 10 to 60 nm. The other set was deposited at 300°C while varying the i-n grading width from 20 to 140 nm. The 3 regions of the graded absorber layer just discussed are depicted in Fig. 5.7. In here the length of the central i region and the i-n region are a function of $(x)$ equal to the i-n region length, for this starting set of experiments, the i-n region $(x)$ was varied with a length from 10 to 60 nm respectively.

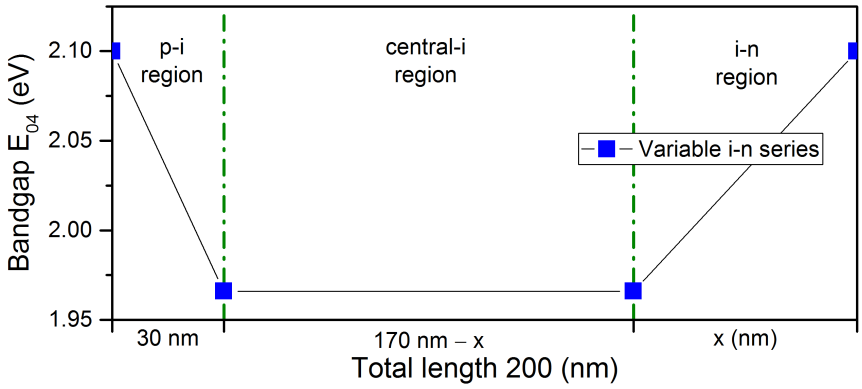


Figure 5.7: Schematic diagram of variable i-n region experimental cells, with a fixed length of 30 nm for the p-i region

The second and third series of experiments have in common that the i-n region length was fixed while the p-i region grading width was varied. One set was made at 200°C, with a constant i-n region grading width of 40 nm. The p-i grading width was varied from 10 to 50 nm. The other set was deposited at 300°C with a constant i-n region grading width of 100 nm. The p-i grading width was varied from 15 to 60 nm. In Fig. 5.8 the length of the central i region and the p-i region are a function of $(x)$ equal to the p-i region length. The length of the i-n region is fixed with the values described previously.

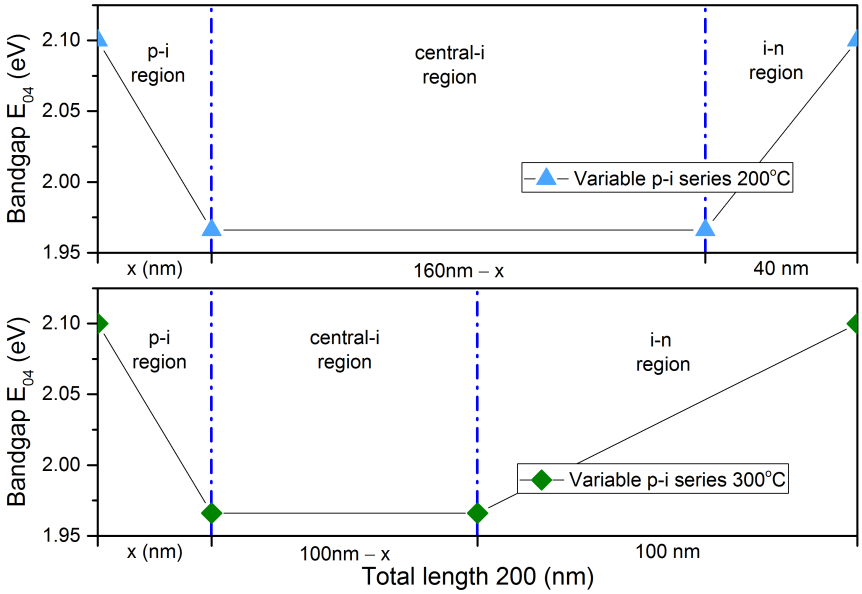


Figure 5.8: Schematic diagram of variable p-i region experimental cells. Cells deposited at 200°C had a constant i-n grading width of 40 nm. Cells deposited at 300°C had a constant i-n grading width of 100 nm.

## 5.3. Results and Discussion

This section presents the data characterizing all solar cells made during the course of this work. The reference cell will be the first results to be presented and discussed. Next it will be the turn for the experimental solar cells where the i-n region was varied. And later on for the experimental cells where the p-i region was varied. The results are further subdivided according to if the absorbing i-layer of the solar cell was deposited at 200°C o 300°C.

The external parameter results are presented in Table 5.2. The current density vs voltage (J-V) curve representing the two reference cells is plotted in Fig. 5.9. And the external quantum efficiency of both reference cells is compared in Fig. 5.10. These results show that the cell at 200°C has a better $V_{OC}$ . While the cell at 300°C had a higher $J_{SC}$ and FF leading to also a better efficiency. The EQE curves show that the cell at 300°C, had for a better response for the wavelength ranges between 350-550 nm and for 600-650 nm, being equivalent in the 650 to 800 wavelength range. The difference in $V_{OC}$ and $J_{SC}$ can be explained by the bandgap of the absorber layer in the two reference cells being slightly different. It was seen in Fig. 4.2 that depositing at 200°C for a–$SiO_x$:H gives a slightly bigger bandgap (0.01-0.03 eV) that when doing so at 300°C. Noting that this can be affirmed because the $CO_2/SIH_4$ ratio and the RF Power used were the same.

Table 5.2: External Parameter results for Reference cells

| | $\mathbf{J_{SC}}$ **(A/m$^2$)** | $\mathbf{V_{OC}}$ **(V)** | **FF** | $\eta$ **(%)** |
|---|---|---|---|---|
| Reference cell at 300°C | 118 ±1.9 | 0.945 ±0.005 | 0.686 ±0.005 | 7.66 ±0.15 |
| Reference cell at 200°C | 112 ±2.5 | 0.996 ±0.003 | 0.654 ±0.009 | 7.32 ±0.19 |

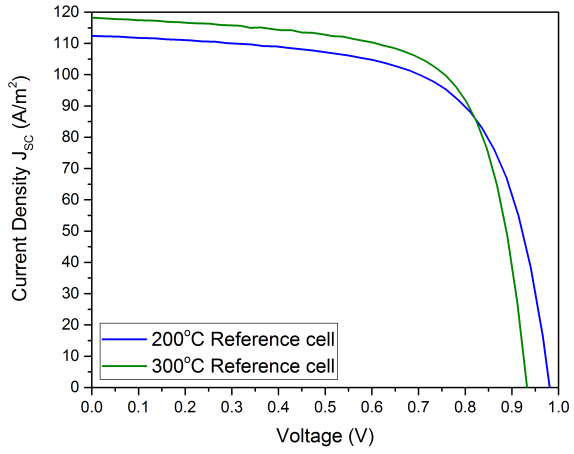


Figure 5.9: J-V curve for reference cells deposited at 200°C and 300°C.

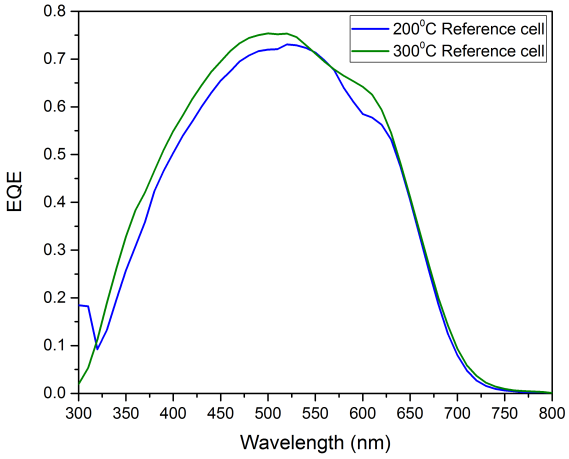


Figure 5.10: External quantum efficiency plot for reference cells deposited at 200°C and 300°C.

### 5.3.1. Experimental cells varying the i-n region

Using the method explained in Section 3.4.4 the experimental results for four external parameters ($J_{SC}$ , $V_{OC}$ , FF and $\eta$%) at 200°C and 300°C are presented in Fig. 5.11 a,b,c & d. Here these graphs show how the four parameters vary in response to the length of the i-n region when the p-i region has a fixed length of 30 nm. The blue dotted line represents the value of the reference cell made at 200°C while the green dotted line corresponds to the reference cell value at 300°C.

External Quantum efficiency plots are also provided to show comparison on what part of the light spectrum is converted to collected charge carriers depending on the grading. The plots provided in

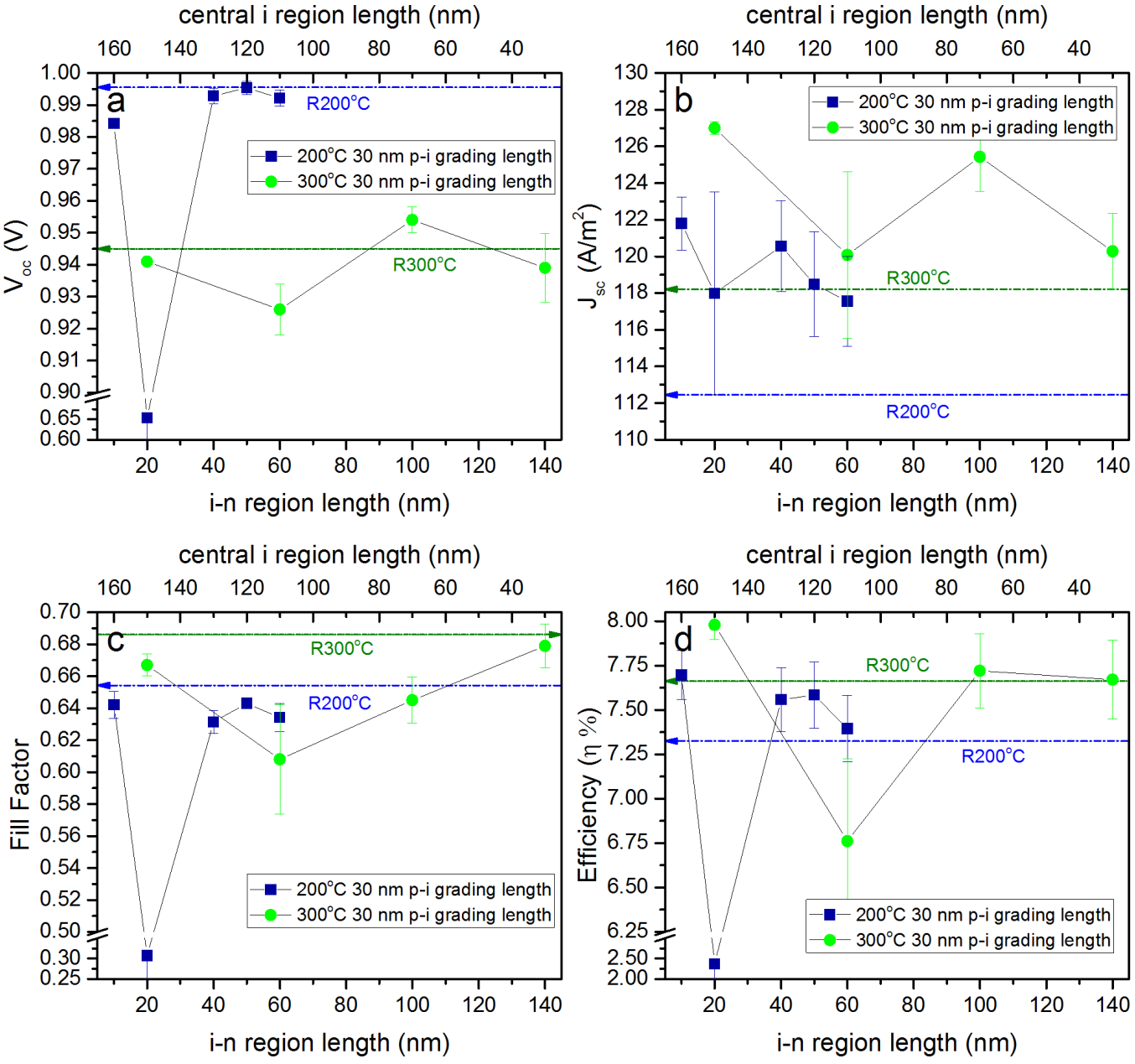


Figure 5.11: a, b, c, d. Ordered from left to right and top to bottom, four electrical properties ($V_{OC}$ $J_{SC}$ FF & $\eta$%) vs i-n region length, keeping the p-i region at a fixed length of 30 nm. Sample cells deposited at 200°C have royal blue symbols. Sample cells deposited at 300°C have light green symbols.

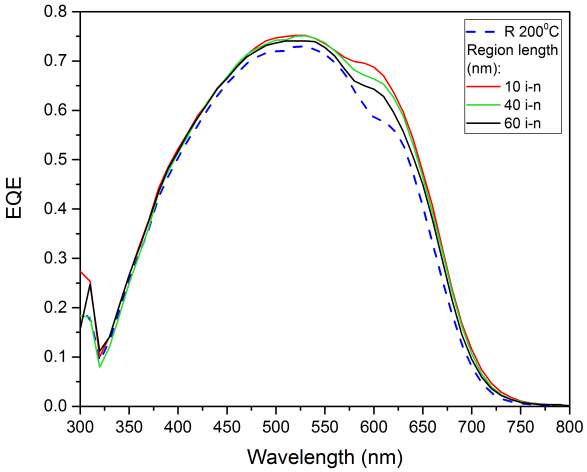


Figure 5.12: Comparison of EQE for samples deposited at 200°C. Sharing in common a p-i region grading length of 30 nm; and varying the i-n region length. A larger version of this plot can be found in Fig. D.1

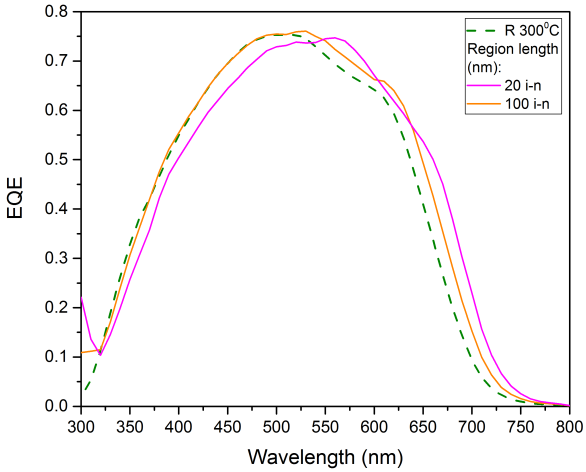


Figure 5.13: Comparison of EQE for samples deposited at 300°C. Sharing in common a p-i region grading length of 30 nm; and varying the i-n region length. A larger version of this plot can be found in Fig. D.2

Fig. 5.12 and Fig. 5.13 show the results for the same experimental cells that are presented in Fig. 5.11. It will first be discussed the results corresponding to cells at 200°C, later it will be discussed the results for the samples made at 300°C and finally these two series will be compared to each other.

The reason why in Fig. 5.11, the samples made at 300 °C were varied for the i-n region over a wider length than the samples at 200 °C, was because the batch made at 300 °was the first deposited and measured. It was seen there were very big differences in the results experienced for $J_{SC}$ , $V_{OC}$ and FF. The values dropped going from 20 to 60 nm, and the three parameters went up again at 100 nm. This gave a clue that further series of experiments with the grading width needed to be varied in smaller increments. In order to be able to better distinguish the change in the external parameters due to the effects of grading.

When looking at Fig. 5.11(a) the $V_{OC}$ for p-i grading lengths of 40 to 60 nm at 200°C is very close to the value of the reference cell (between 0.99 to 0.995 V), the value of $V_{OC}$ at 10nm suggests the $V_{OC}$ tends to drop with an i-n grading width smaller than 40nm.

In Fig. 5.11(b) it can be seen that it can be seen all solar cells have $J_{SC}$ values significantly larger than the reference cell. The highest was obtained by the cell having the shortest i-n grading width (10 nm) (an increase of 8.7% from reference values). Above 40 nm in i-n grading width, the $J_{SC}$ shows a slight trend of starting to fall. These results can also be compared to the EQE plot of Fig. 5.12 the cell at 10 nm in i-n outperforms the other cells in current collection by obtaining a better response from 400 nm till 700 nm. There is a slight improvement of the blue response (450 to 495 nm) but most of the improvement was seen in the green till early red response (495 till 620 nm). As the i-n grading width increased, the shape of the spectral response was similar, but always becoming weaker as the i-n grading width increased. It is expected that the response at higher wavelengths is larger when the i-n grading width is small. Because this solar cell would have in average more material in the absorber layer of a lower bandgap (pure a–Si:H); than a cell having more grading width, more a–$SiO_x$:H in its composition and an average bandgap composition higher. However the slight increase in the blue response cannot be answered by this logic.

Reflecting on FF values in Fig. 5.11(c) The cells always performed slightly under the value of the reference cell at 200°C (by 0.01). There is no significant trend seen for the FF going up or low in function of the i-n grading width. This trends repeats continuously across all the experimental cell data when comparing it to the reference cell values.

Lastly looking at efficiency in Fig. 5.11(d) all samples (excluding the outlier value at 20 nm) had

a higher efficiency than the reference cell. Even tough the values for the $V_{OC}$ and FF are not very different from those of the reference cell, the significant increase in $J_{SC}$ is the reason behind the increase in efficiency. The cell at 20 nm in i-n region length, had a very poor performance in $V_{OC}$ , FF and consequently in efficiency as well, it is considered an outlier value because the cell was manufactured at the same time as the rest of the other cells with the same temperature.

Next it will be discussed the results for experimental cells deposited at 300°C. Again looking at Fig. 5.11 the following trends are seen. In Fig. 5.11(a) The experimental cells show more variation from the $V_{OC}$ value of the reference cell, than how it was for the cells made at 200°C. The highest value corresponding for the sample at 100 nm in i-n grading length) was higher than the reference cell value by 0.01 V. The $V_{OC}$ values for 20 and 140 nm in i-n grading width are similar and also close to the reference cell value. But the composition of the absorber layer for both configurations is vastly different, the cell at 140 nm would have an average bandgap higher than the one at 20 nm, so in terms of only bandgap it could be expected the $V_{OC}$ to be larger (like it is for 100 nm). The fact that is not, could indicate such a large p-i grading width also increases recombination due to the higher density of defects a–$SiO_x$:H tend to have [98]. As opposed to the amount of defects a–Si:H cell have. Considering how the sample at 100 nm had the highest $V_{OC}$ , it could be possible an optimized p-i grading width for a higher $V_{OC}$ would probably be obtained between 60 and 140 nm of grading width.

Observing $J_{SC}$ performance in Fig. 5.11(b) the highest values are obtained for 20 and 100 nm in p-i grading width. The obtained gains are comparable to the ones obtained by the cells deposited at 200°C (8 to 9 A/$m^2$). The value at 100 nm is specially interesting, since it managed to increase the $J_{SC}$ and $V_{OC}$ over reference cell values. Taking a look at the EQE plot in Fig. 5.13, the two cells with the highest $J_{SC}$ show clearly a higher response over the reference cell value. But they do it by increasing the response in two different parts of the light spectrum. The cell at 100 nm i-n grading width has practically same the quantum efficiency than the reference cell up to 500 nm, after this value there is an increase in all the light spectrum up to the end at 750 nm (increase in response for green till end of red spectrum). In contrast the cell with the 20 nm i-n grading width, had a lower response than the reference cell up to 525 nm (decrease in blue-green response), but at higher wavelengths the response was always higher than the reference cell, higher also than the cell at 100 nm i-n from 650 nm and above.

A possible conclusion can be drawn from these results. As the grading width length in the i-n region increases, the EQE response tends to shift to becoming more efficient in current collection for shorter wavelengths, and less efficient for using longer wavelengths. But there is an optimized range of grading where the absorption of the shorter wavelength is maintained with the same levels of a constant bandgap cell; while still obtaining a net gain in current, from absorption into longer wavelengths (above 500nm).

Talking about FF performance in Fig. 5.11(c) for 300°C samples, the same trend was seen as with 200°C samples, where none of the cells had an equal or higher value than the one of the reference cell. The values suggest the FF tends to decrease if the i-n region and central i region are of similar width. This is theorized because the values with the shortest i-n region and central-i region were the closest to the FF value of the reference cell.

Looking at Fig. 5.11(d) to discuss about the efficiency, the cells at 100 and 140 nm i-n region width had similar values of efficiency to the one of the reference cell, the cell at 140 nm in general had a similar performance in all parameters to the reference cell, and the gain in $J_{SC}$ and $V_{OC}$ by the cell at 100 nm was negated by the loss in FF. However the cell at 20 nm in i-n grading width had an efficiency of 7.98%, this is the best efficiency that was obtained from all experimental solar cells made during the course of this work. The high result is owed to the gain in $J_{SC}$ while keeping the losses in FF and $V_{OC}$ small. Comparing the i-n grading width series at both temperatures. One trend could be seen. When a small i-n graded region (10 to 20 nm) is used, a significant gain in $J_{SC}$ is obtained while a small decrease in $V_{OC}$ and FF is expected.

### 5.3.2. Experimental cells varying the p-i region

Now it will be presented the results for the second and third series of experiments where the i-n region was kept at a fixed grading width. Unlike in the past section, this time the results at 200°C and 300°C, are not presented in the same plot. The difference in the width of the i-n region is the reason behind it. A parenthesis in the narrative is made here to explain this decision. During the course of experimenting, the first cells to be made were the ones at 300°C with a constant p-i grading width of 30 nm, it was seen in that series that the cell with 100 nm for i-n grading width was the one with the biggest $V_{OC}$ (Fig. 5.11). The series made at 300°C with a fixed i-n region was made thinking this $V_{OC}$ could perhaps be conserved. However the other 3 samples made with the i-n region width of 100 nm exhibited a considerably lower $V_{OC}$ , FF and efficiency (Fig. 5.16). Therefore it was considered a large i-n region was not beneficial to performance of the solar cell and that it would be more interesting in the next batch of experiments to vary the p-i region over a smaller constant i-n width, like with 40 nm. Discussing again the results, first are presented the electrical parameters results together with the EQE plots for the samples at 200°C. These results can be seen in Fig. 5.14. By reading this data it can be observed:

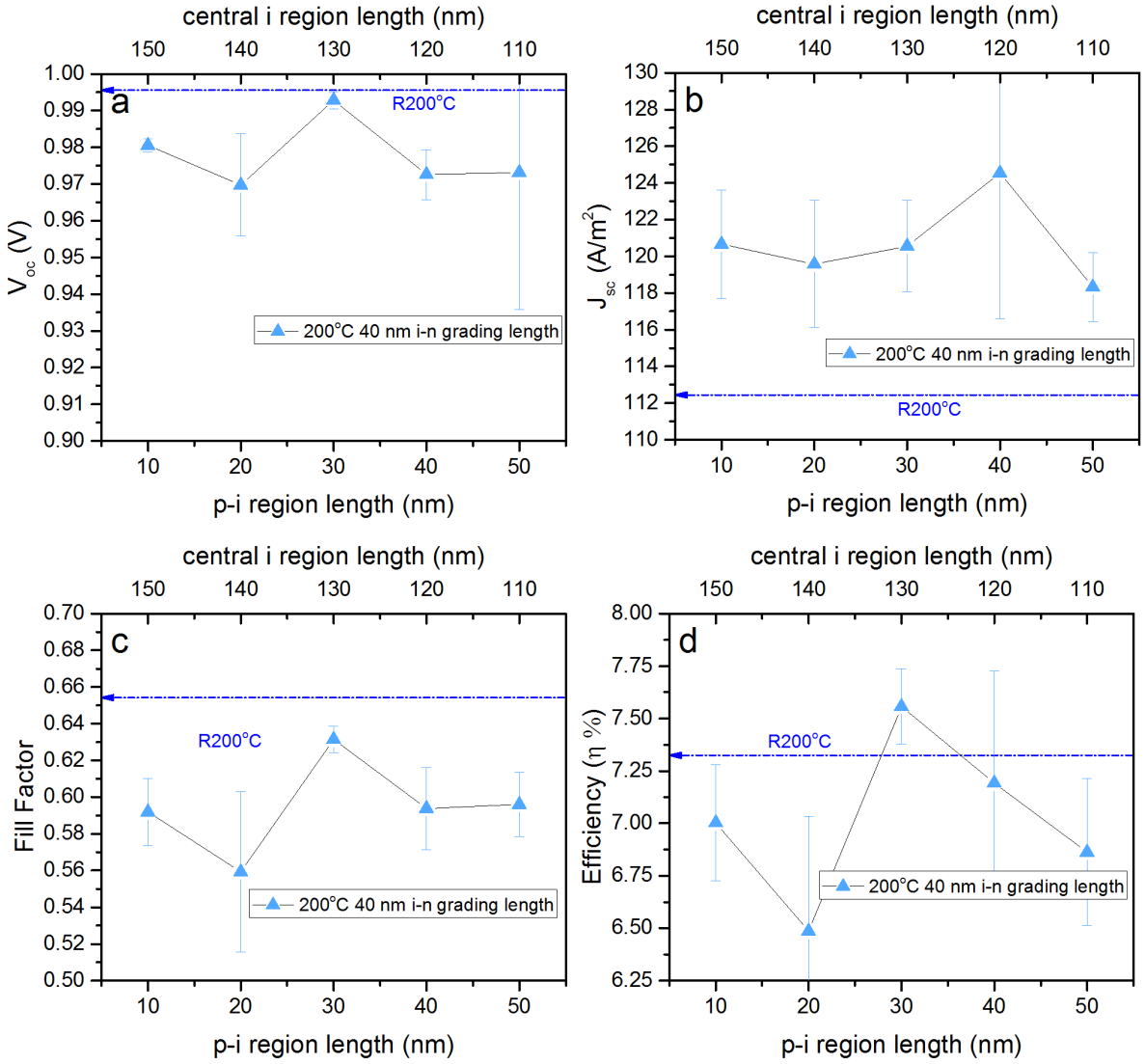


Figure 5.14: a, b, c, d. Ordered from left to right and top to bottom, four electrical properties ($V_{OC}$ $J_{SC}$ FF & $\eta$%) vs p-i region length. Sample cells deposited at 200°C keeping the i-n region at a fixed length of 40 nm.

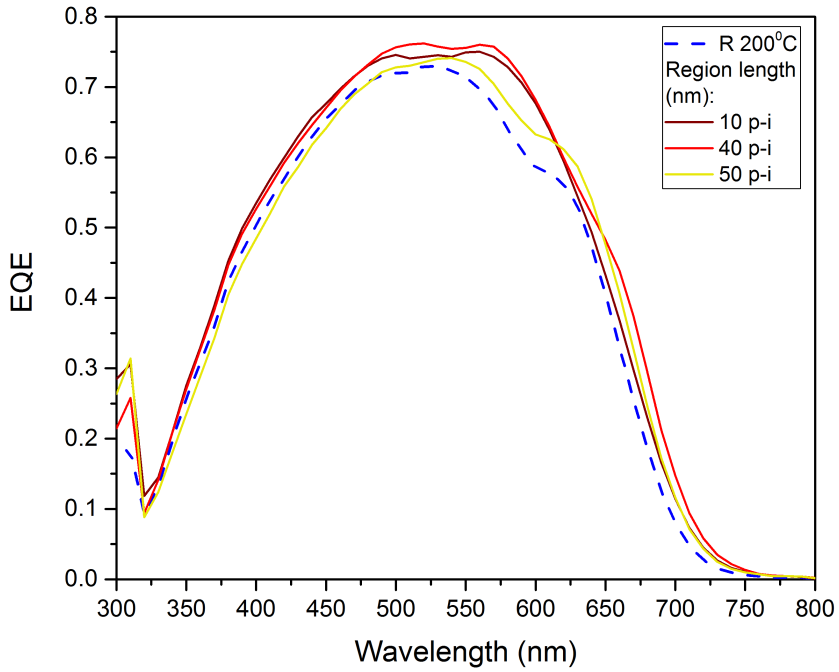


Figure 5.15: Comparison of EQE for samples deposited at 200°C. Sharing in common a i-n region grading length of 40 nm; and varying the p-i region length. An extended version of this plot can be found in Fig. D.3

Commenting first about Fig. 5.14(a) the $V_{OC}$ appears to have an optimal between 20 and 40 nm for i-n grading width, as suggested by the $V_{OC}$ above 0.99 V obtained with the 30 nm length p-i region sample. This value is the closest one to the reference cell value. The drop in the $V_{OC}$ for this experiment series was larger than the one seen for the cells varying the i-n region with the same temperature of deposition.

Looking at current density in Fig. 5.14(b), all values were above reference cell values, by at least 6 A/m$^2$. From 10 to 30 nm for p-i grading width the $J_{SC}$ is around 120 A/m$^2$ but between 30 and 50 nm a peak was seen at 40 nm, with a $J_{SC}$ of 124 A/m$^2$, the current density however drops again at 50 nm. Contrasting these values to the EQE performance from Fig. 5.15 the curves at 10 nm and 40 nm p-i grading width showed better response than the reference cell at all wavelengths, the 40 nm sample had an increase from 5 to 10% in the quantum efficiency response for the wavelength range between 500 to 600 nm.

Discussing FF performance in Fig. 5.14(c), in the same way as it was seen with all the others experimental series results till now. The FF performance was always below reference cell value. However this fall is more pronounced than the one experienced with the variable i-n series at the same temperature. It is noticeable that the FF and $V_{OC}$ results follow a very similar trend, with 20 nm being the lowest and 30 nm becoming the closer in both parameters to the reference cell values.

Lastly talking about efficiency in Fig. 5.14(d), for the sample at 30 nm in p-i grading width the efficiency is significantly better (above 7.5%) than the reference cell and all other experimental cells in this series. Comparing the performance of all cells in this series. The results suggest there is an optimal value for p-i grading length, between 30 and 50 nm, that combines a high $J_{SC}$ with a high $V_{OC}$ , to yield an even higher efficiency.

The last series of experiments to be discussed is the one corresponding for the cells deposited at 300 °C, keeping the i-n region fixed at 100 nm for the grading width and varying the p-i region length. For this series Fig. 5.16 displays the external parameters results. From them the following trends are taken:

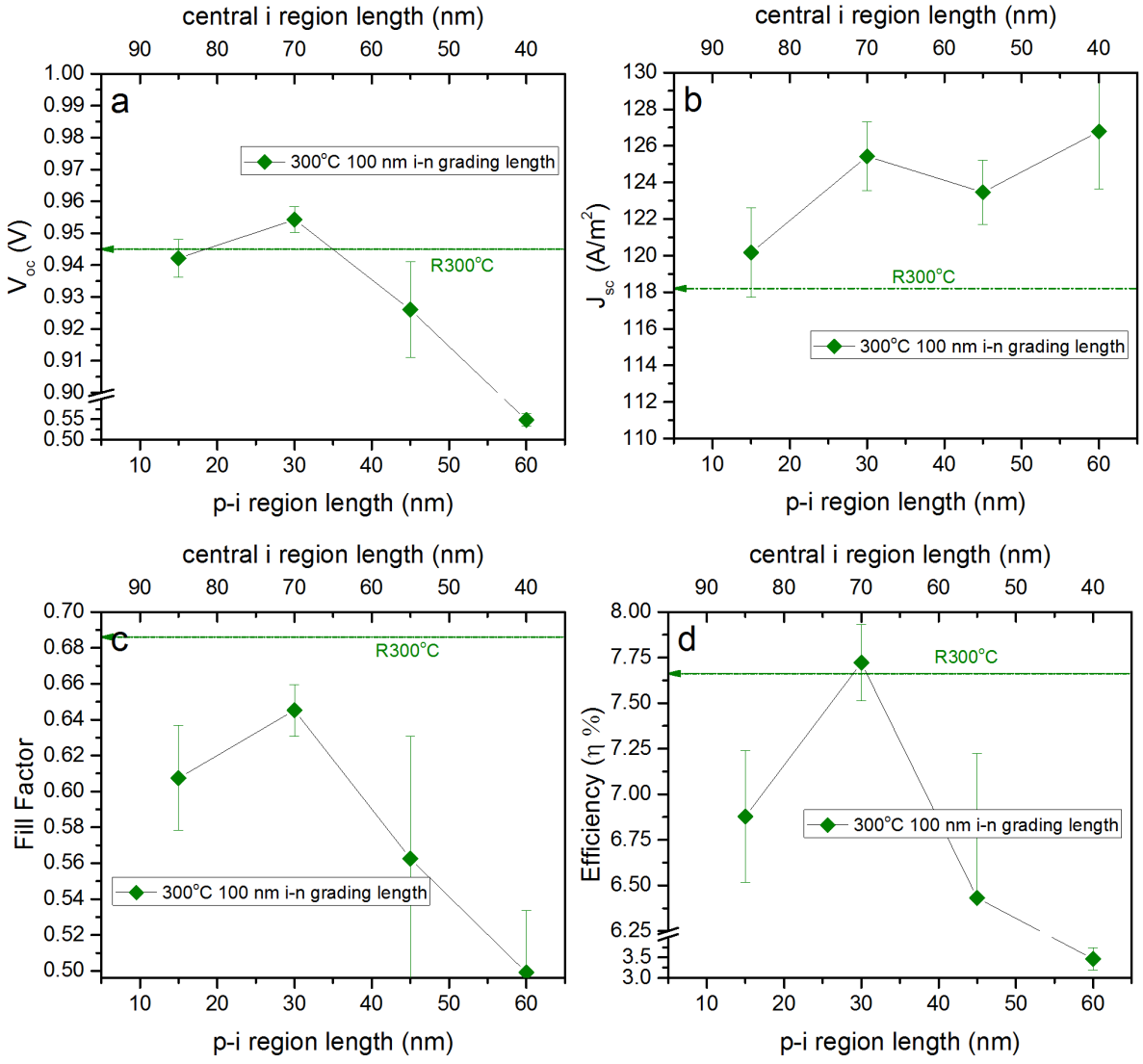


Figure 5.16: a, b, c, d. Ordered from left to right and top to bottom, four electrical properties ($V_{OC}$ $J_{SC}$ FF & $\eta$%) vs p-i region length. Sample cells deposited at 200°C keeping the i-n region at a fixed length of 40 nm.

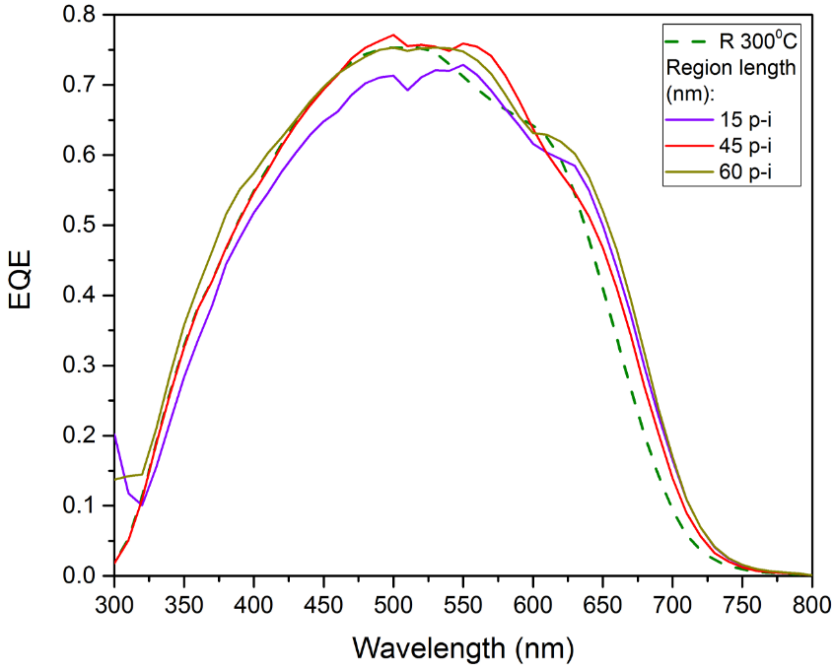


Figure 5.17: Comparison of EQE for samples deposited at 300°C. Sharing in common a i-n region grading length of 100 nm; and varying the p-i region length. An extended version of this plot can be found in Fig. D.4

Commenting on the $V_{OC}$ results seen in Fig. 5.16(a) a downward trend can be seen in $V_{OC}$ for p-i grading lengths above 30 nm, the same trend is also seen for FF. Looking at $J_{SC}$ performance in Fig. 5.16(b) there is an upward trend that with a larger p-i grading width the current density becomes the highest, comparing these values to the EQE curves in Fig. 5.17 the curves at 45 and 60 nm obtain a higher $J_{SC}$ mainly by improving the spectral response in the wavelength range after 525 nm. The FF factor values seen in Fig. 5.16(c) were all low, this issue was also seen when varying p-i region width for 200°C. Another thing in common from both series is that the FF was the closest to the reference value at 30 p-i region width.

Trying to find a reason over why the FF is decreasing with larger values of the p-i grading width; could be related to the material having a very high amount of grading (the 100 nm of fixed i-n region length). This amount of grading made necessary to deposit for more steps and for a longer time a higher $CO_2/SIH_4$ gas flow ratio. Kim *et al.*[88, Fig. 6] showed that larger $CO_2$ flow rates and oxygen concentration lead to a lower photo conductivity ($\sigma_{ph}$). The $\sigma_{ph}$ for the graded bandgap in the specific case of the 300°C samples could have gone from $10^{-5}$ (S/cm) to values of ($10^{-6}$ to $10^{-7}$) S/cm at the edge of the graded bandgap. This in turn is related to the mobility and lifetime products that when lowered because of defects increase the recombination and decrease the FF. The application of this reasoning is challenged by the results from Fig. 5.11, where the samples with 140 nm in i-n grading length do not seen the FF lowered. However it must be also interpreted that the p-i region could be more susceptible to a decrease in $\sigma_{ph}$ due to the lower mobility of holes.

Commenting on the efficiency results seen in Fig. 5.16(d) only at 30 nm of p-i grading width the efficiency is slightly above the reference cell at 7.6%. For the other cells the low FF made them all to have a very low efficiency. Considering the trends for FF and $V_{OC}$ it could be possible there is an optimum value for efficiency between 20 and 40 nm of p-i grading width.

Something that all experimental series have in common is that whenever an experimental cell had a very low average FF value, this would also be accompanied by a very high error margin (high standard deviation). Also another trend that is easy to notice is that temperature of deposition has a high relevance for $V_{OC}$ and to a lesser extent for $J_{SC}$ . Cells deposited at 200°C had $V_{OC}$ values between 0.97 and 0.995. Cells deposited at 300°C had $V_{OC}$ values between 0.925 and 0.955 V. Cells deposited

at 300°C in contrast tended to show higher $J_{SC}$ .

### 5.3.3. Overview of electrical performance of all cells

To give an overview on how the electrical performance in $J_{SC}$ , $V_{OC}$ , FF and $\eta\%$ compares for all experimental cells made during the course of this work, the Fig. 5.18 is presented. In this plot the $(y)$ axis is a combination of $V_{OC}$ and FF parameters by showing their product. The $J_{SC}$ is shown in the $(x)$ axis, and since all the parameters to calculate $\eta\%$ are present, iso-efficiency lines could be drawn. The make possible to compare the efficiency of the different samples. For example in this plot is easy to pinpoint that the best performing cell corresponds to $j$. Which is the sample made at 300°C having 30 p-i, 150 center-i and 20 i-n nm in grading width. A table showing the deposition parameters and raw results for all experimental cells is available in Table B.1.

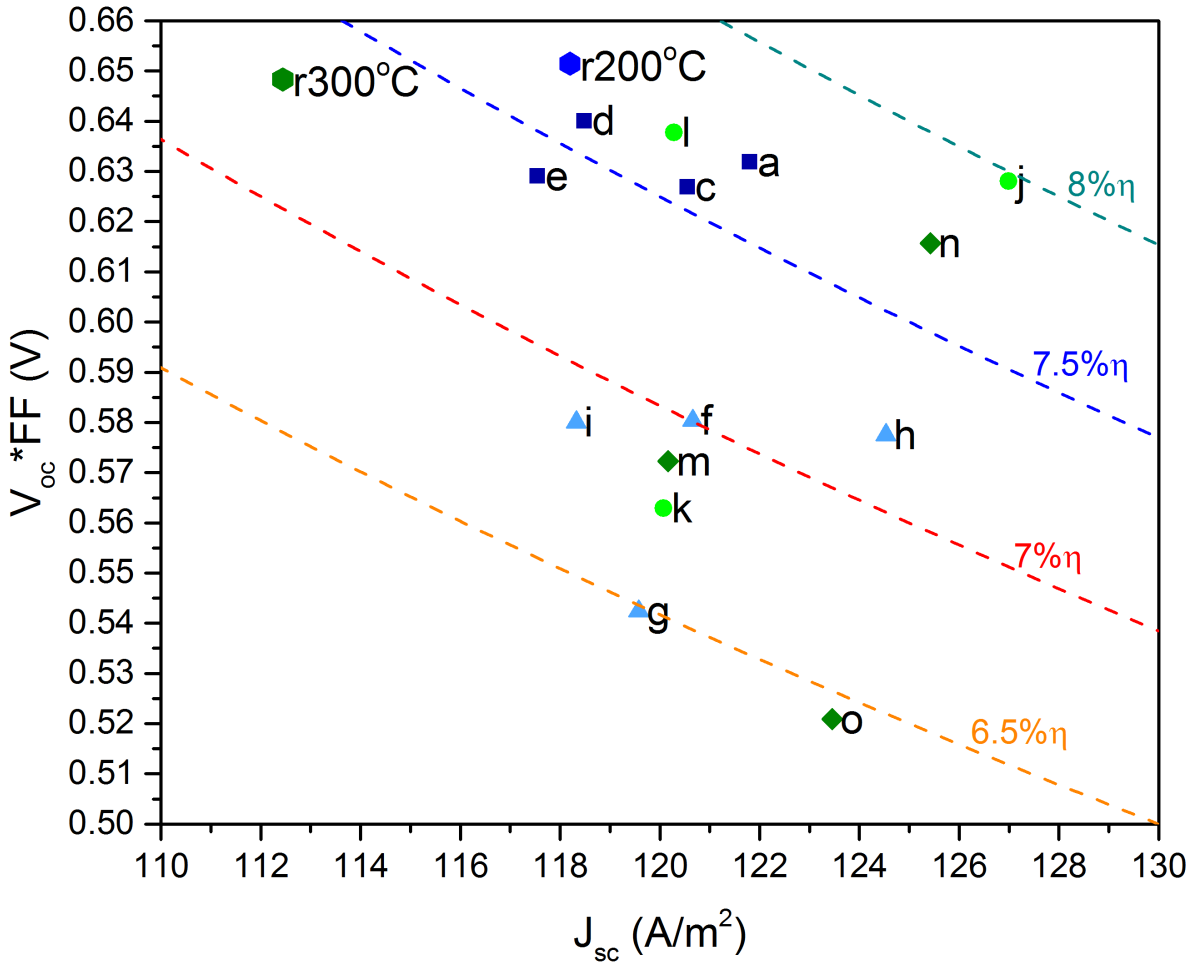


Figure 5.18: Overview of electrical performance for all experimental cells.

- Cells marked with a square in royal blue (a-e) are results for 200°C, varying i-n region width.
- Cells marked with a triangle in light blue (f-i) are results for 200°C, varying p-i region width.
- Cells marked with a circle in light green (j-l) are results for 300°C, varying i-n region width.
- Cells marked with a diamond in dark green (m-o) are results for 300°C, varying p-i region width.

The code letters used in this figure are identifiers for Table B.1, where it is enlisted the electrical performance raw data, for all the experimental cells made.

Some trends seen in Fig. 5.18, are for example that results from 200°C series of experiments are less spread (more grouped together), than the ones from 300°C. Another observation is that the 200°C

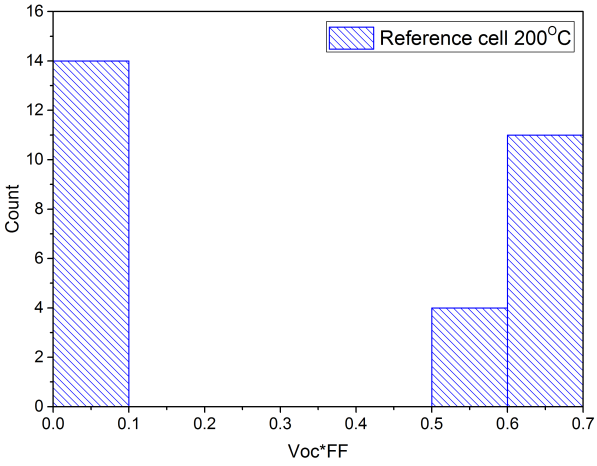


Figure 5.19: 30 cell areas performance distribution of $V_{OC}$×FF for reference cell at 200°C.

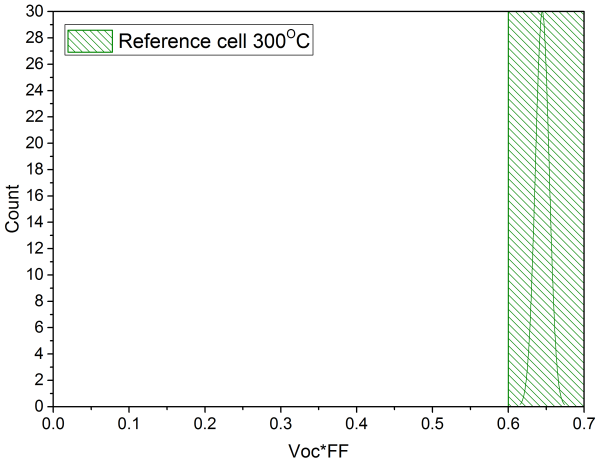


Figure 5.20: 30 cell areas performance distribution of $V_{OC}$×FF for the reference cell deposited at 300°C.

series varying i-n region (royal blue), show that as the grading width, the current density started to decrease. For 200°C experimental cells, 6 samples out of 9 (66%) had a $V_{OC}$ *FF product above 0.58 and an efficiency above 7%. While for 300°C experimental cells, only 3 samples out of 7 (43%), had a $V_{OC}$ *FF product above 0.58 and an efficiency above 7%.

### 5.3.4. Solar-cell yield

As it was explained in Section 3.4.2, the electrical performance was not homogeneous for all the 30 contact areas of each experimental cell. Therefore to give a dimension of the problem, this section presents a comparison, of what proportion of solar cells contact areas were having a yield of solar cells with an acceptable performance.

It was seen the performance of an experimental cell contact area was mostly differentiated by how good the $V_{OC}$ and FF were. In contrast, $J_{SC}$ could remain at high values while the other two parameters dropped sharply, decreasing efficiency as a consequence. Solar cells with a reasonable performance usually have a $V_{OC}$ and FF product above 0.4, below this value the efficiency of the cell is never above 3 percent. For practical reasons the $V_{OC}$ and FF product is used in this section as an indicator of the quality of the solar cell contact area.

The distribution of Voc*FF of the reference cells is shown in Fig. 5.19 and Fig. 5.20, and for a better detailed version of reference at 300°C, Fig. 5.21 is provided. Comparing the 3 figures, it can be seen a big difference in the performance yield across the 30 cell areas. The reference cell at 200°C had 14 cell areas (46% of total) with a $V_{OC}$× FF equal or below 0.1, therefore not having an acceptable performance. In contrast the reference cell at 300°C had all the 30 cells working in a similar range, having a $V_{OC}$×FF product above 0.6. Some of the experimental cells had a yield of performance that concentrated around a specific value, for these cells a normal distribution curve is overlapped on the histogram charts to give a reference around which value the performance yield is dispersed. This difference in the performance yield was also seen in a more severe way in the experimental cells. The results corresponding to the best performing cells in terms of efficiency are shown in Fig. 5.22 and in Fig. 5.23.

Fig. 5.22, has an average efficiency for the best five cell areas of 7.69%, the distribution in the $V_{OC}$×FF shows 11 cell areas having a result above 0.6, and the same number of cells having a result below 0.4. If the average of the efficiency was to be calculated using the best 10 cells areas average of $V_{OC}$×FF the efficiency drops to 7.62%. Same calculation but with the best 20 cells gives an efficiency of 6.17%. Taking a look at Fig. 5.23. This cell has an average efficiency for the best five cell areas of 7.98%, the distribution in the $V_{OC}$×FF shows 7 cell areas having a result above 0.6. But this experimental cell

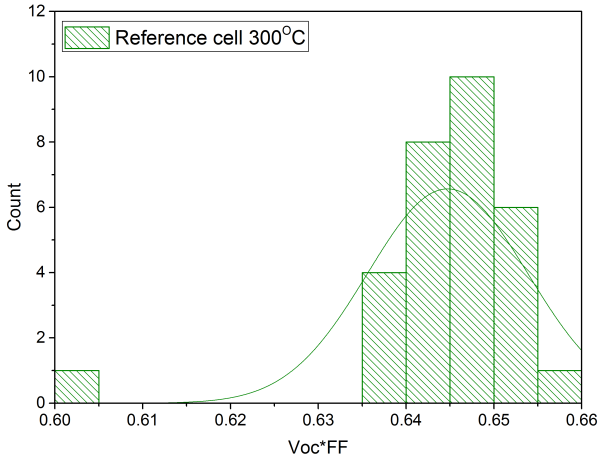


Figure 5.21: The distribution of $V_{OC}$×FF for reference cell at 300°C.

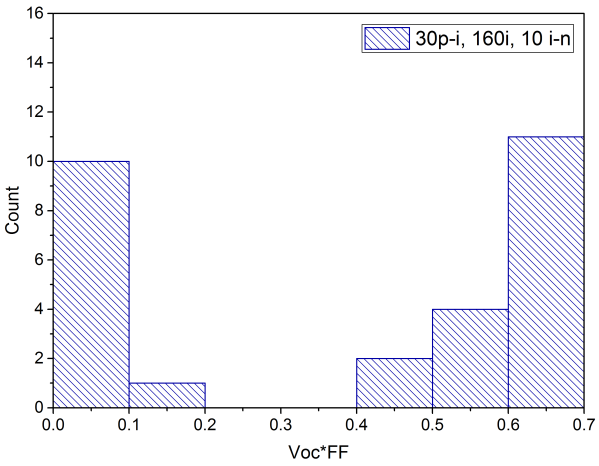


Figure 5.22: Performance distribution of $V_{OC}$×FF for highest efficiency cell at 200°C.

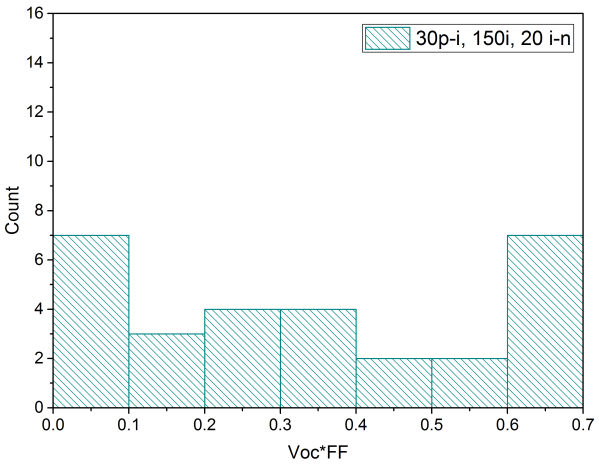


Figure 5.23: Performance distribution of $V_{OC}$×FF for highest efficiency cell at 300°C.

did not show a concentration of values in any specific range. The results were evenly spread from 0 to 0.6. If the average of the efficiency was to be calculated using the best 10 cells areas average of $V_{OC}$×FF the efficiency drops to 7.69%. Same calculation but with the best 20 cells gives an efficiency of 5.8%.

The performance variation in $V_{OC}$×FF for all cells is available in Appendix C. These plots help to recognize that the occurrence of a low yield of acceptable working cells is a common problem. Regardless of the temperature of deposition. There is also a direct correlation between the cells that had a poor electrical average performance, were also the cells having the lowest yield in a $V_{OC}$×FF product in acceptable levels.

Over why the yield of working cells areas is so low, many reasons are possible. But starting the analysis from the reference cell results: Why for the reference sample at 200°C, half of the cell areas were not working? While in comparison all of the cell areas at 300 °C were working. They were made at different dates, so it could be possible that the deposition machine described in Section 3.2.1, was working differently. More tests would need to be conducted to find out if the variability is due to the deposition temperature or the machine setup.

Now looking at the experimental samples, many of them had a spread of performance yield that was similar to the cell in Fig. 5.23. Something that could have happened is that the gas mixture is

not homogeneous across the whole volume of deposition. Meaning that the designed gas mixture flow could not coincide in practical terms to the amount of oxygen present in the deposition chamber. Every 10 nm deposited in a bandgap step, the gas flow would be changed to deposit 10 nm of the next bandgap step. It would be interesting to further experiment if shorter or longer deposition steps. Influence the performance yield in a positive way. This problem is also something not only related to grading, during deposition it was also common that sometimes one section of the cell like for example the outer section outperforms the middle section. Nevertheless it is an already present variation that grading seems to make it higher by yet unknown reasons.

# 6

# Conclusions and Recommendations

Remembering the objective and motivation of this work from Chapter 2 we can say that it has been fulfilled to a certain extent. Band gap grading has shown positive results for increasing the photocurrent density and the efficiency, when comparing the experimental results to those of the reference cell.

It was seen that generally all samples deposited at 300 °C showed a lower $V_{OC}$ than the samples at 200 °C. It was stated in the objective we wanted to maintain the high $V_{OC}$ ×FF previous research had achieved. Therefore the samples at 300 °C are not considered in fulfilling the objectives of this work.

Discussing the impact of the improvement seen for the experimental samples at 200 °C when compared to the reference cell values. The highest $J_{SC}$ and efficiency cell was seen in Fig. 5.11, with a grading width of 30, 160, and 10 nm for the 3 graded regions (p-i, central-i and i-n respectively). In this solar cell $J_{SC}$ was increased from 112.4 A/m$^2$ in the reference cell, to 121.8 A/m$^2$, which represents a relative increase of 8.3%. However both $V_{OC}$ and FF had a small decrease from 0.996 to 0.984 V (minus 1.2%) and 0.654 to 0.642 (minus 1.8%). Nevertheless the decrease in $V_{OC}$ ×FF product did not offset the improvement in $J_{SC}$ . So there was a relative efficiency gain of 5% since the net efficiency increased from 7.3 to 7.7 %. The reason behind this behaviour is thought to be closely related to the composition of the absorber layer in this grading configuration. A big portion of the absorber in the central i-region with 160 nm, had a constant low bandgap at 1.96 eV (pure a–Si:H). This region is believed to be the one contributing the most to the high $J_{SC}$. Only 40 nm, in the front and back (p-i, i-n regions) of the absorber, had varying concentrations of oxygen in its structure (a–$SiO_x$:H ). Going from a bandgap of 1.96 to 2.1 eV, these two region are believed to have contributed the most to stay close in $V_{OC}$ to the value of a pure a–$SiO_x$:H cell. The reason for the drop in FF is not known yet, but it is speculated that it could be related to the deposition process with grading not being controlled enough, introducing areas with heterogeneous oxygen concentrations acting as defects.

The improvements bandgap grading provide can be summarized in the following statement: For an a–$SiO_x$:H solar cell it is possible to increase the photocurrent density and efficiency by applying a gradual decrease in bandgap over a narrow width (10 to 30 nm) for the regions close at the beginning (p-i region) and at the end of the intrinsic layer (i-n region). This will also lead to a slight decrease in $V_{OC}$ and FF.

Outside of the objectives, there were also opportunities for learning from this experience. It was seen for very big grading widths (140 nm of i-n region) that the performance of the graded solar cell closely resembled the reference cell performance in all external parameters like it is seen in Fig. 5.11. This also includes the EQE response, in Fig. 5.13 at 20 nm the EQE response is shifted to the right and at high graded width values it is shifted to the left, almost matching the response of the performance cell. This type of graded cell had a bigger volume of the absorber having a–$SiO_x$:H material with the proportion to the central i region (pure a–Si:H) just being of 30 nm. Therefore it can be stated that

long amounts of graded regions (above 70% of the total thickness of the absorber) effectively negate any change in performance from a pure a–$SiO_x$:H solar cell.

Looking back to comment on what could have been done differently. It would have been interesting to have made different reference cells. The two reference cell produced for this project had a constant $CO_2/SiH_4$ ratio during deposition of 0.25. While during bandgap grading this parameter was varied from 0 till 0.8. This set of references would had been deposited at different $CO_2/SiH_4$ ratios from 0 till 0.8. With the aim to know if varying degrees of oxygen (and different bandgaps) have a similar effect on the performance of the solar cell, compared to what bandgap grading did.

Also during the course of this work it is not known what is the separate effect of bandgap grading when just one of the edges of the absorber is graded, either the p-i or the i-n region but not both. Literature review showed that for a–$SiGe_x$:H research on bandgap grading it was beneficial to perform these types of test samples first in order to optimize the length of the grading width of both regions[27].

Other types of grading are also yet to be explored. The grading performed over the course of this work can be identified as being of the U shape when compared to similar grading design done on [30] for a–$SiGe_x$. Same research applies grading structure that was not explored for a–$SiO_x$:H Like for example the ”V” or the ”UV” shape seen in Fig. 5.6 or the exponential shape seen in Fig. 5.5.

For a closing statement on the promise and usefulness of bandgap grading for a–$SiO_x$:H solar cells. This technique paired with other cutting edge methods to increase photocurrent can lead to a new record for an a–$SiO_x$:H thin film solar cell. For example, the current record of 8.8% in efficiency for single junction a–$SiO_x$:H solar cell [83], could likely be increased to reach 9.1-9.2 % if the same improvement from our reference cell is achieved. Also our reported best cell would give better current matching in a Tandem cell, thanks to the photocurrent of graded bandgap a–$SiO_x$:H being above 120 $A/m^2$.

# A

# Appendix A Grading example

Table A.1: Example of Gas flow and deposition time for configuration of 30p-i. 110 mid-i, 60 i-n

| $E_{04}$ | Thickness (nm) | $CO_2/SiH_4$ ratio | Deposition rate (nm/s) | Deposition time (s) | $SiH_4$ feed (sccm) | $CO_2$ feed (sccm) |
|---|---|---|---|---|---|---|
| 2.100 | 10 | 0.79 | 0.060 | 166 | 5.6 | 4.4 |
| **2.055** | **10** | **0.49** | **0.069** | **145** | **6.7** | **3.3** |
| 2.011 | 10 | 0.24 | 0.078 | 128 | 8.0 | 2.0 |
| 1.966 | 110 | 0.00 | 0.088 | 1254 | 10.0 | 0.0 |
| 1.988 | 10 | 0.14 | 0.082 | 122 | 8.8 | 1.2 |
| 2.011 | 10 | 0.24 | 0.078 | 128 | 8.0 | 2.0 |
| 2.033 | 10 | 0.36 | 0.074 | 136 | 7.3 | 2.7 |
| 2.055 | 10 | 0.49 | 0.069 | 145 | 6.7 | 3.3 |
| 2.078 | 10 | 0.64 | 0.065 | 155 | 6.1 | 3.9 |
| 2.100 | 10 | 0.79 | 0.060 | 166 | 5.6 | 4.4 |

# B

# Appendix B Electrical Performance

Table B.1: Electrical Performance raw data for samples presented in Fig. 5.18

| Code Letter | Amigo serial batch | p-i region length (nm) | central-i region length (nm) | i-n region length (nm) | $J_{SC}$ (A/m2) | $V_{OC}$ (V) | Fill Factor | Efficiency $\eta$ (%) |
|---|---|---|---|---|---|---|---|---|
| r200 | M10440 | | | | 118.197 | 0.945 | 0.686 | 7.66 |
| r300 | M10558 | | | | 112.442 | 0.996 | 0.654 | 7.32 |
| a | M10649 | 30 | 160 | 10 | 121.800 | 0.984 | 0.642 | 7.70 |
| b | M10578 | 30 | 150 | 20 | 117.978 | 0.653 | 0.307 | 2.37 |
| c | M10650 | 30 | 130 | 40 | 120.549 | 0.993 | 0.631 | 7.56 |
| d | M10651 | 30 | 120 | 50 | 118.485 | 0.995 | 0.643 | 7.58 |
| e | M10576 | 30 | 110 | 60 | 117.546 | 0.992 | 0.634 | 7.39 |
| f | M10628 | 10 | 150 | 40 | 120.660 | 0.981 | 0.592 | 7.00 |
| g | M10629 | 20 | 140 | 40 | 119.579 | 0.970 | 0.559 | 6.49 |
| h | M10630 | 40 | 120 | 40 | 124.532 | 0.973 | 0.594 | 7.19 |
| i | M10631 | 50 | 110 | 40 | 118.325 | 0.973 | 0.596 | 6.86 |
| j | M10460 | 30 | 150 | 20 | 126.990 | 0.941 | 0.667 | 7.98 |
| k | M10459 | 30 | 110 | 60 | 120.072 | 0.926 | 0.608 | 6.76 |
| l | M10458 | 30 | 30 | 140 | 120.278 | 0.939 | 0.679 | 7.67 |
| m | M10441 | 15 | 85 | 100 | 120.169 | 0.942 | 0.607 | 6.88 |
| n | M10442 | 30 | 70 | 100 | 125.423 | 0.954 | 0.645 | 7.72 |
| o | M10443 | 45 | 55 | 100 | 123.460 | 0.926 | 0.562 | 6.43 |
| p | M10444 | 60 | 40 | 100 | 126.786 | 0.548 | 0.499 | 3.47 |
| q | M10726 | 30 | 135 | 10 | 108.647 | 0.990 | 0.610 | 6.56 |
| r | M10727 | 30 | 105 | 40 | 109.293 | 0.792 | 0.343 | 2.96 |
| s | M10725 | 30 | 95 | 50 | 117.432 | 0.858 | 0.384 | 3.87 |
| t | M10652 | 40 | 100 | 60 | 118.059 | 0.993 | 0.620 | 7.27 |

# C

# Solar-cell Yield for all Experimental Cell

This appendix contains all the results comparing the performance yield measured in $V_{OC}\times$ F for the experimental and reference cells.

The plots are grouped in two sections first the results for 300 °C deposited cells. And later for 200 °C deposited cells. The order for the plotting also follows the logic of first placing the reference cell. Followed by the cells with a common p-i grading length. And lastly the cells with a common i-n grading length. Accompanying each plot there is a code letter (cell "j" for example) this code letter is the same as the one used in Table B.1 and in Fig. 5.18.

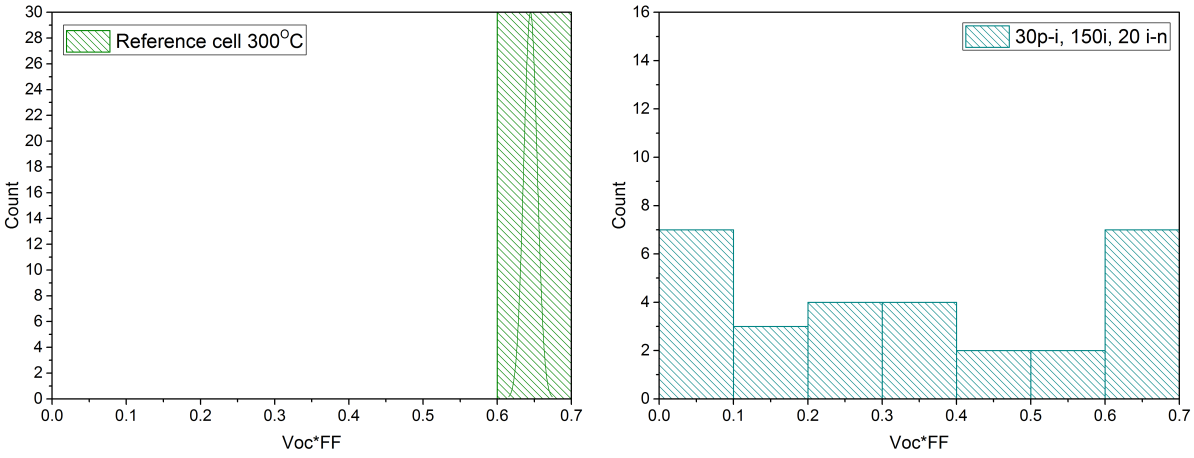


(a) Detailed view of distribution of $V_{oc}$×FF cell r300




(b) Detailed view of distribution of $V_{oc}$×FF cell j

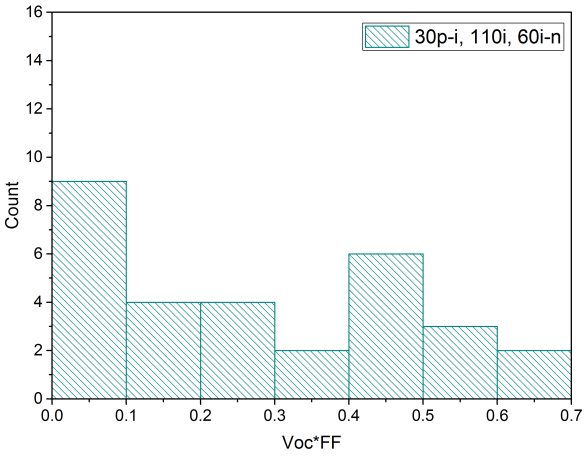


(c) Detailed view of distribution of $V_{oc}$×FF cell k

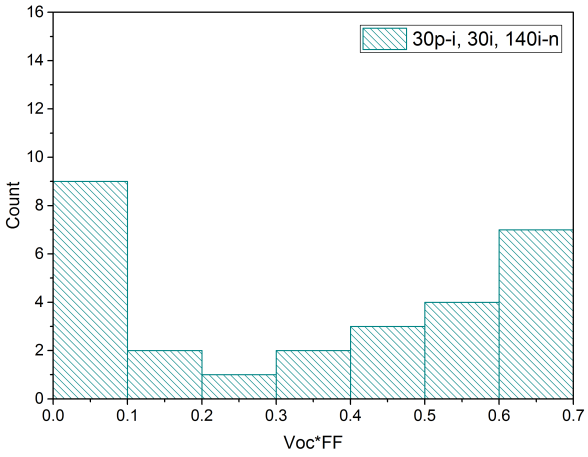


(d) Detailed view of distribution of $V_{oc}$×FF cell l

Figure C.1: Yield of performance for solar cells deposited at 300°C. Part 1)

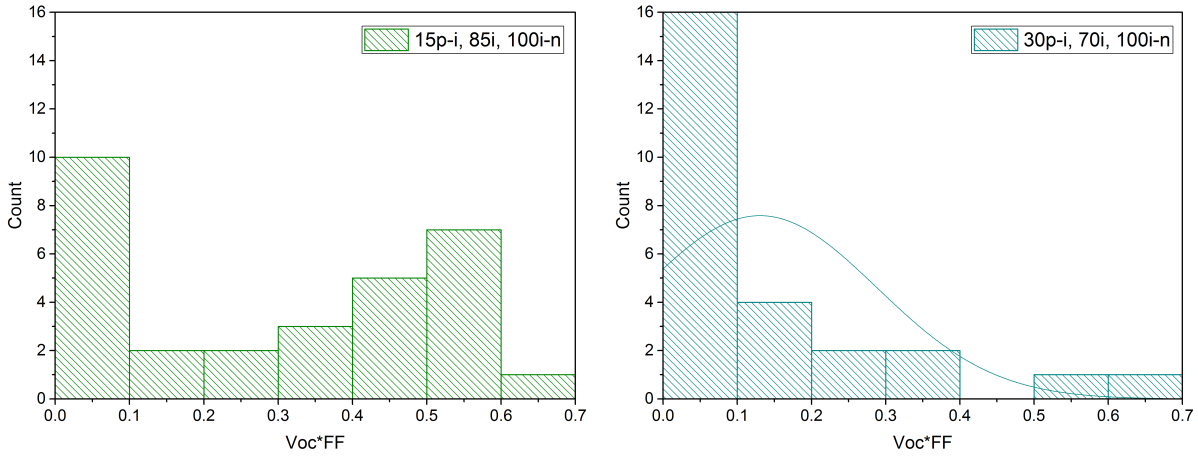


(a) Detailed view of distribution of $V_{oc}$×FF cell m




(b) Detailed view of distribution of $V_{oc}$×FF cell n

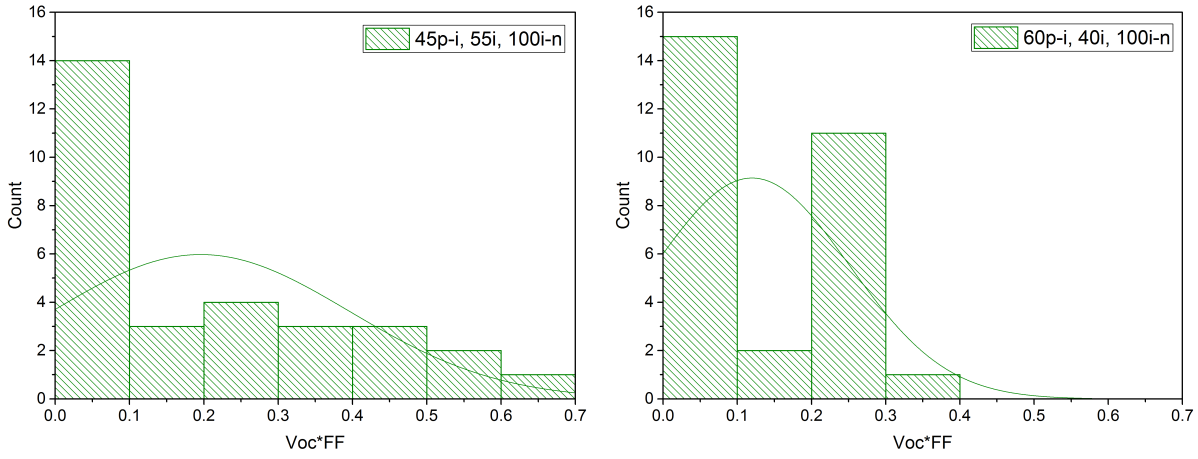


(c) Detailed view of distribution of $V_{oc}$×FF cell o




(d) Detailed view of distribution of $V_{oc}$×FF cell p

Figure C.2: Yield of performance for solar cells deposited at 300°C. Part 2)

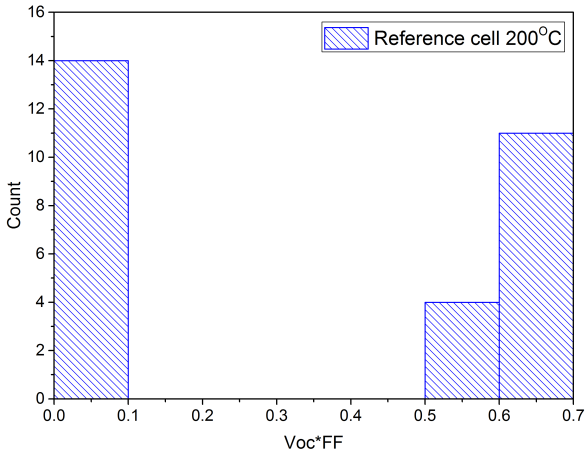


(a) Detailed view of distribution of $V_{oc}$×FF cell r200

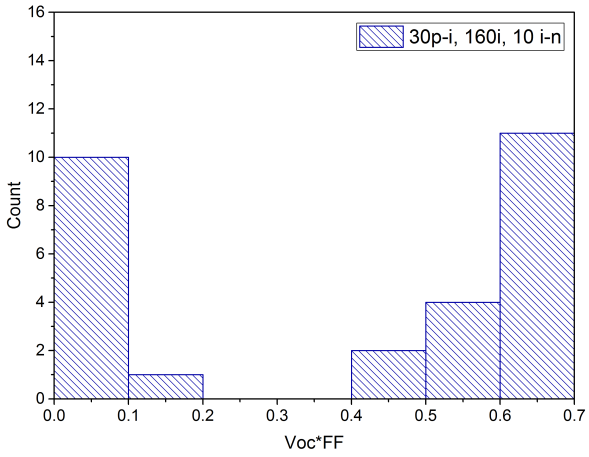


(b) Detailed view of distribution of $V_{oc}$×FF cell a

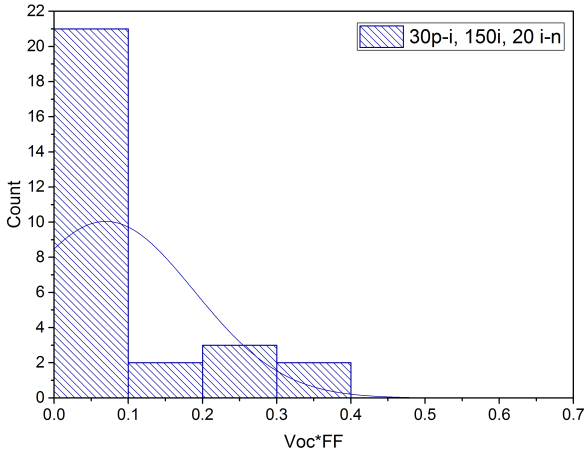


(c) Detailed view of distribution of $V_{oc}$×FF cell b

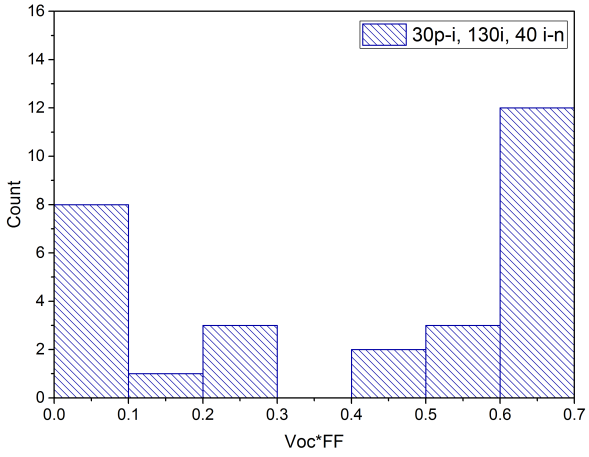


(d) Detailed view of distribution of $V_{oc}$×FF cell c

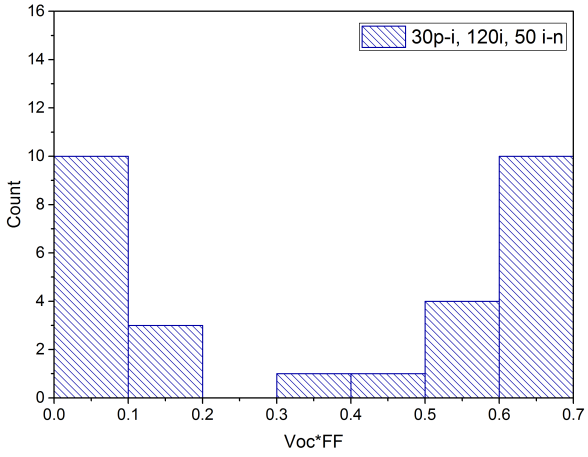


(e) Detailed view of distribution of $V_{oc}$×FF cell d

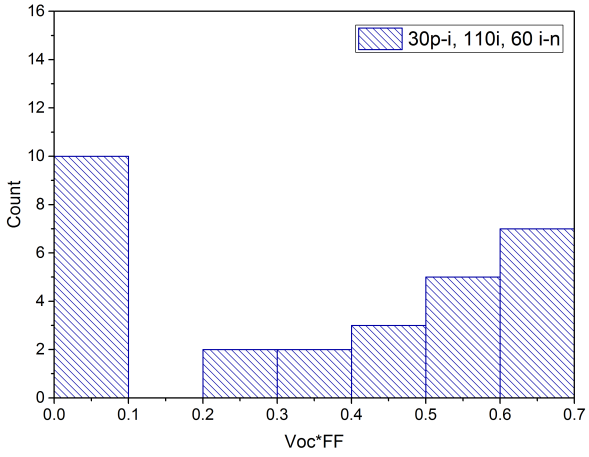


(f) Detailed view of distribution of $V_{oc}$×FF cell e

Figure C.3: Yield of performance for solar cells deposited at 200°C. Part 1)

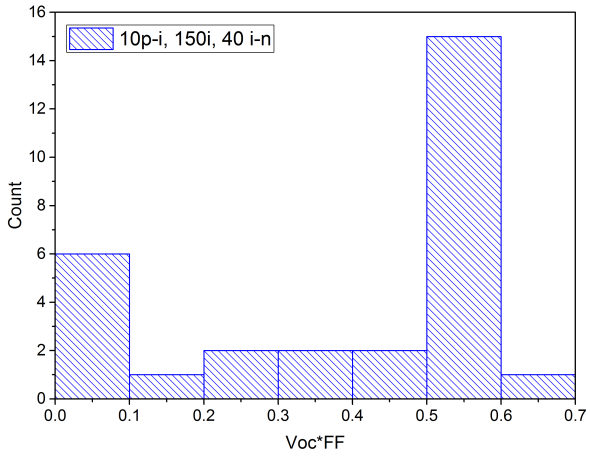


(a) Detailed view of distribution of $V_{oc}$×FF cell f

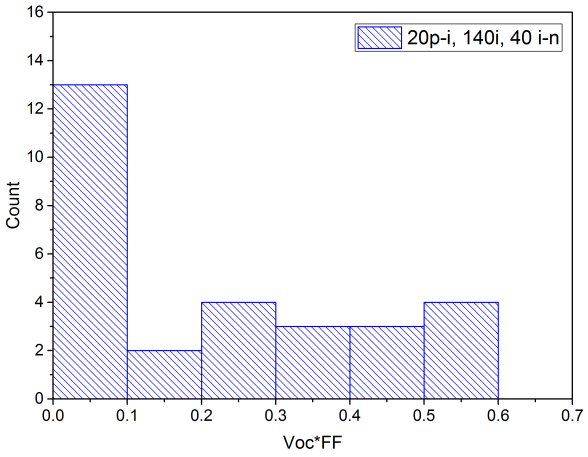


(b) Detailed view of distribution of $V_{oc}$×FF cell g

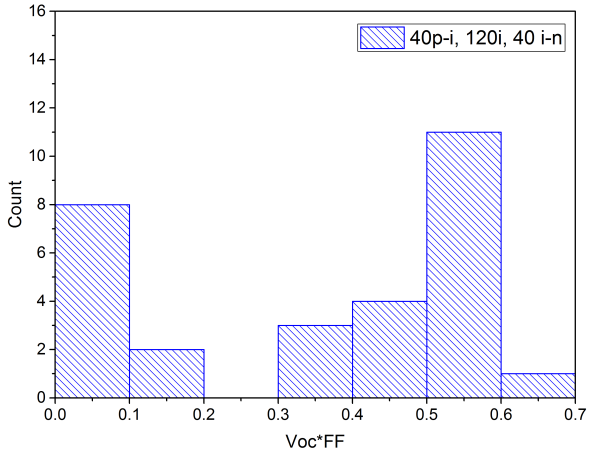


(c) Detailed view of distribution of $V_{oc}$×FF cell h

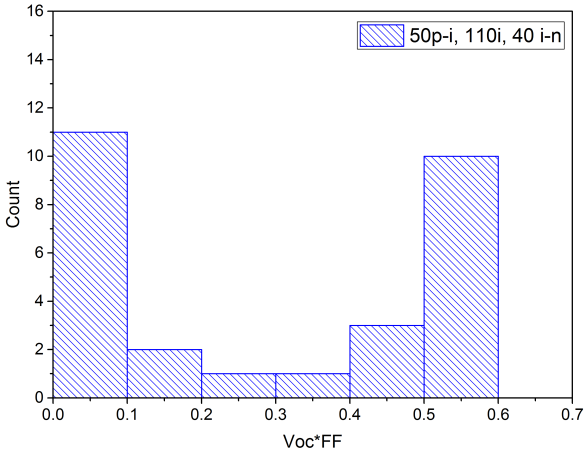


(d) Detailed view of distribution of $V_{oc}$×FF cell i

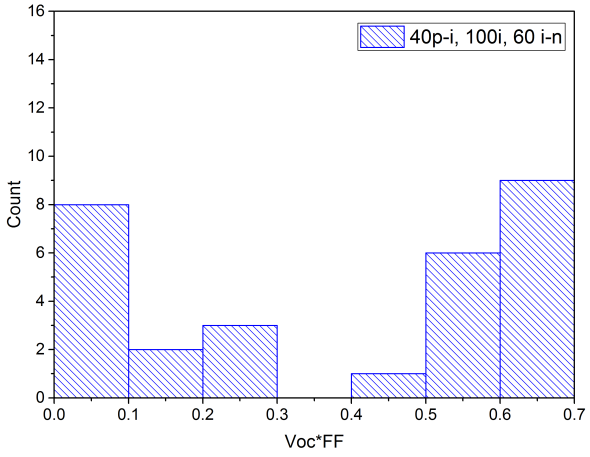


(e) Detailed view of distribution of $V_{oc}$×FF cell t

Figure C.4: Yield of performance for solar cells deposited at 200°C. Part 2)

# D

# Appendix D External Quantum efficiency extended plots

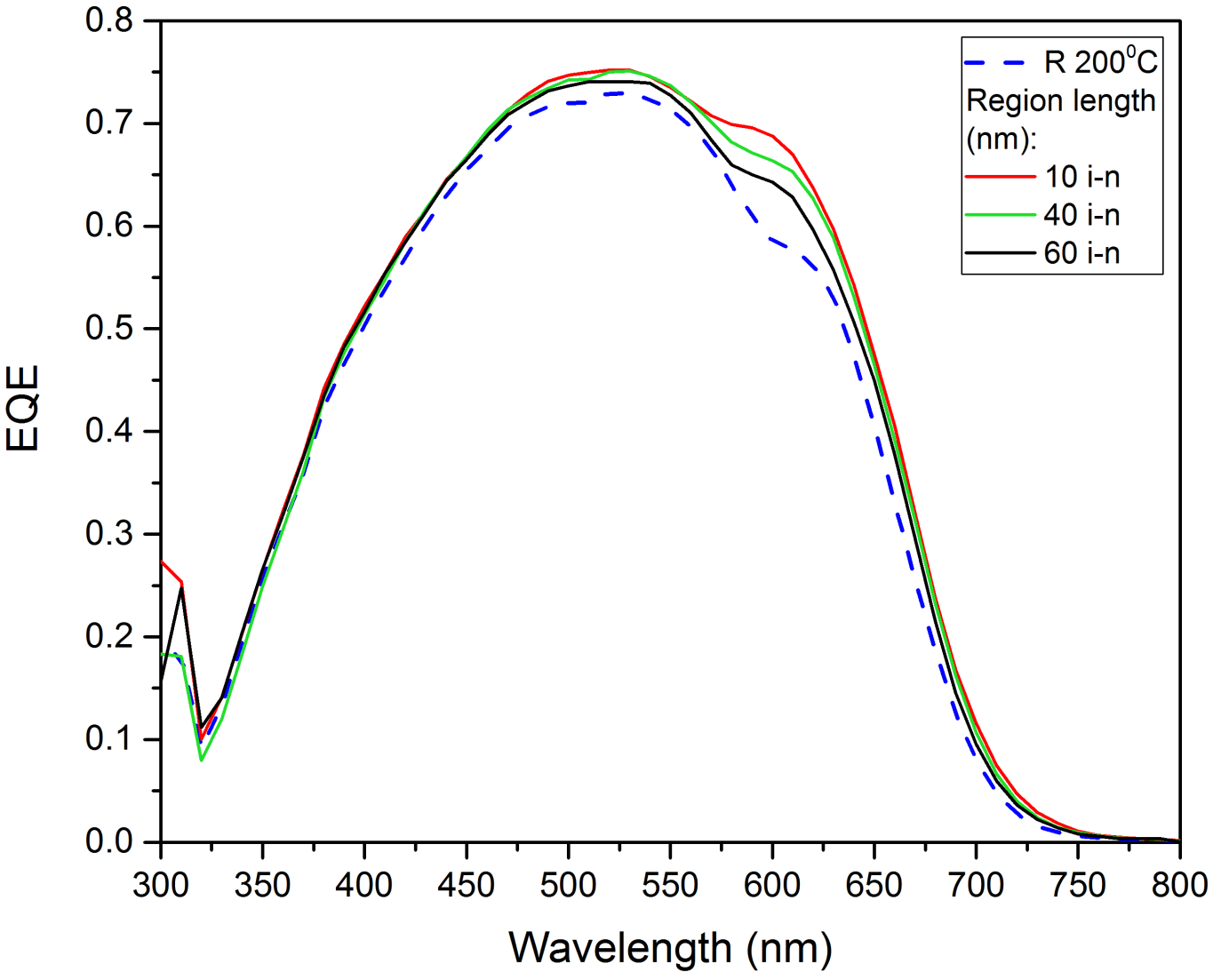


Figure D.1: Extended version of comparison of EQE for samples deposited at 200 °C. Sharing in common a p-i region grading length of 30 nm; and varying the i-n region length.

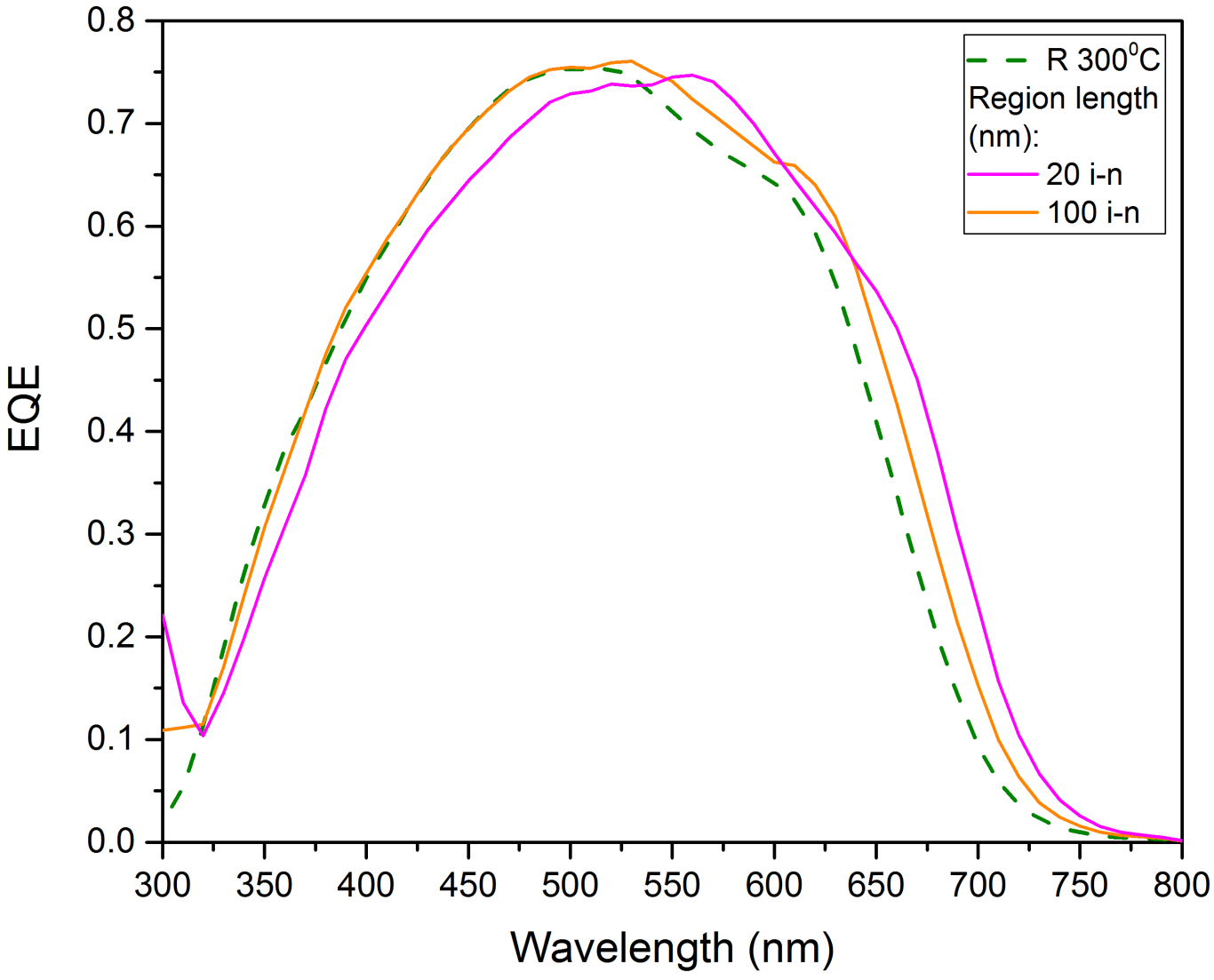


Figure D.2: Extended version of comparison of EQE for samples deposited at 300 °C. Sharing in common a p-i region grading length of 30 nm; and varying the i-n region length.

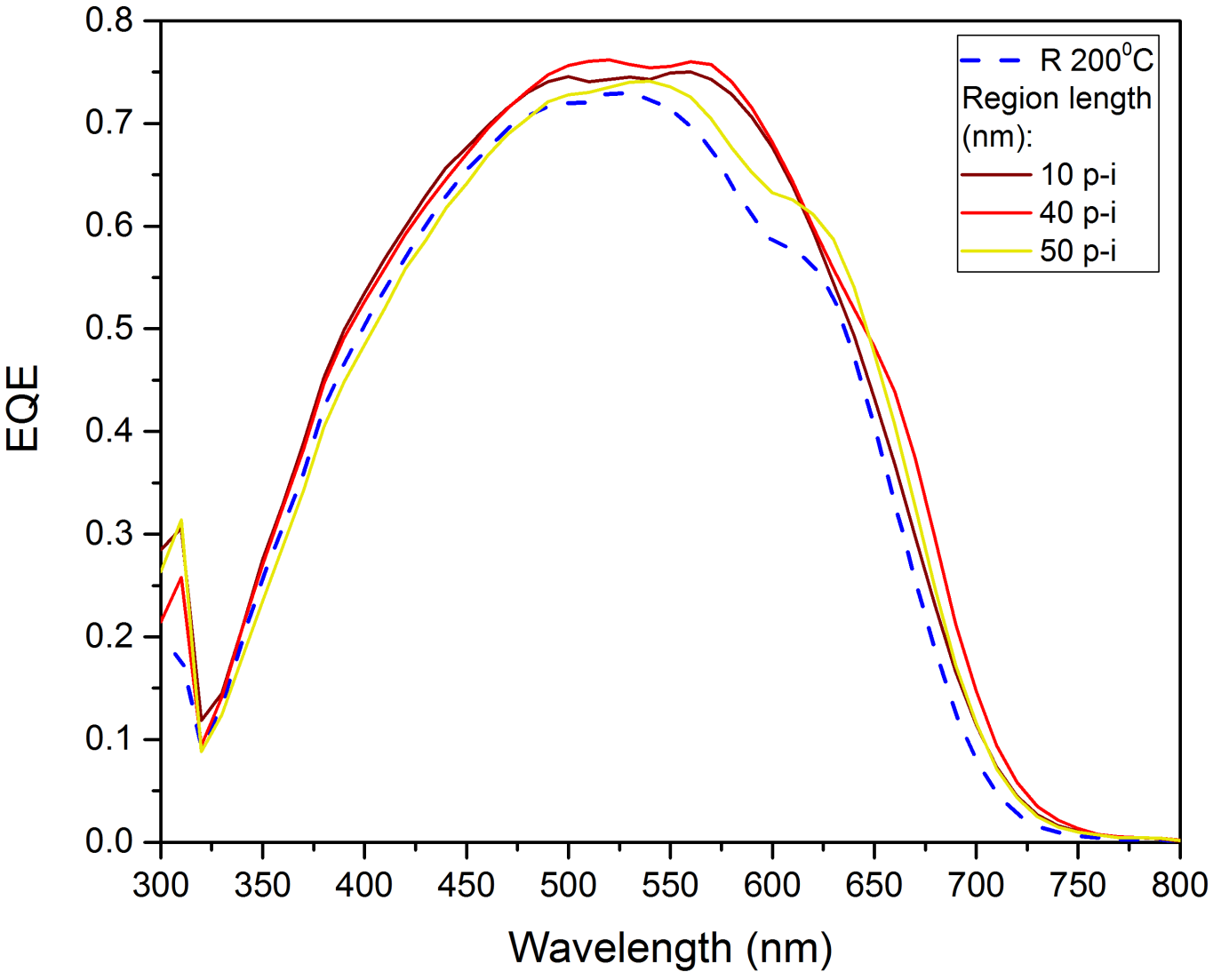


Figure D.3: Extended version of comparison of EQE for samples deposited at 200 °C. Sharing in common a i-n region grading length of 40 nm; and varying the p-i region length.

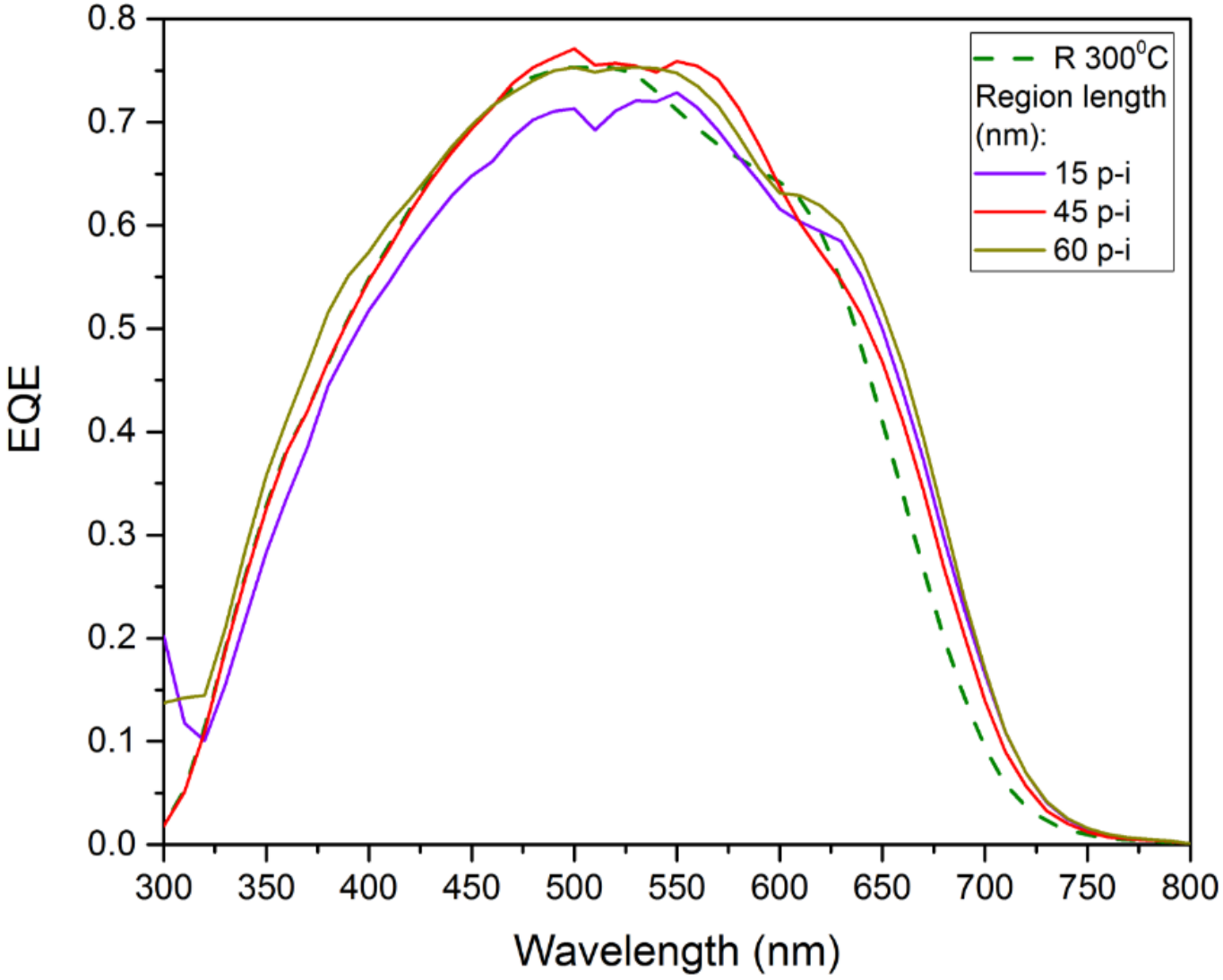


Figure D.4: Extended version of comparison of EQE for samples deposited at 200 °C. Sharing in common a i-n region grading length of 100 nm; and varying the p-i region length.

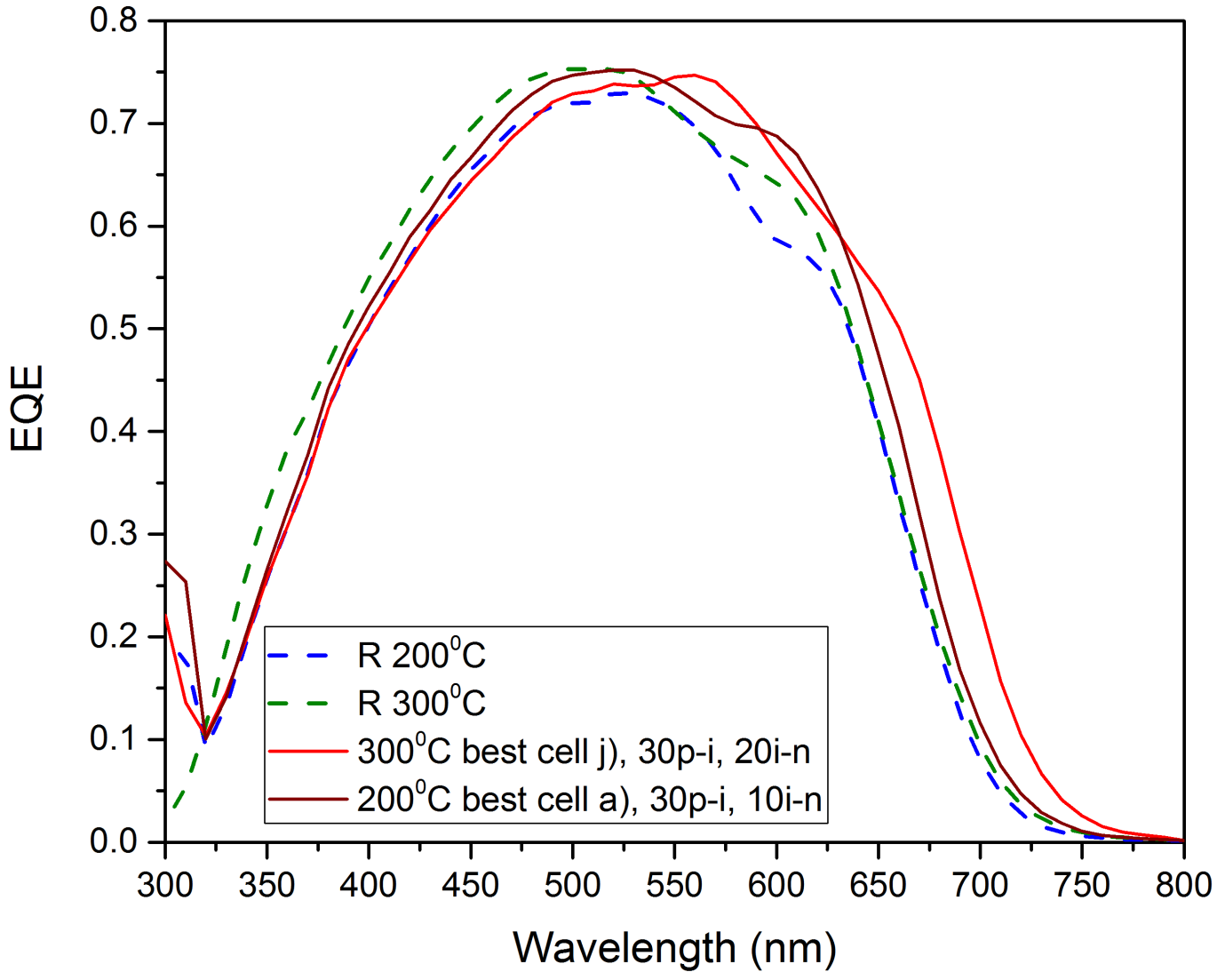


Figure D.5: Extended version of comparison of EQE for Reference cells and best performing in terms of highest efficiency experimental cells deposited at 200 °C and 300 °C.

# Bibliography


[1] United Nations Department of Economic and Social Affairs/Population Division UN DESA, *World Population Prospects: The 2017 Revision, Key Findings and Advance Tables*, Tech. Rep. (UN DESA, 2017).

[2] M. R. Hannah Ritchie, *Energy production & changing energy sources,* https://ourworldindata.org/energy-production-and-changing-energy-sources/ (2017), [Accessed on: 2017-15-10].

[3] The World Bank, *Energy use (kg of oil equivalent per capita),* https://data.worldbank.org/indicator/EG.USE.PCAP.KG.OE (2014), [Accessed on: 2017-10-17].

[4] World Energy Council, *World Energy Resources Full Report 2016*, Tech. Rep. (World Energy Council, 2016).

[5] U.S. Energy Information Administration EIA, *What drives crude oil prices?* https://www.eia.gov/finance/markets/crudeoil/spot_prices.php (2017), [Accessed on: 2017-10-19].

[6] National Aeronautics and Space Agency (NASA), *Scientific consensus: Earth's climate is warming,* https://climate.nasa.gov/scientific-consensus/ (2017), [Accessed on: 2017-10-18].

[7] M. Perez and R. Perez, *Update 2015–a fundamental look at supply side energy reserves for the planet,* Natural Gas **2**, 215 (2015).

[8] Land Art Generator Initiative, *Total surface area required to fuel the world with solar,* http://landartgenerator.org/blagi/archives/127 (2015), accessed on 2017-08-18.

[9] N. Amin, S. A. Shahahmadi, P. Chelvanathan, K. S. Rahman, M. I. Hossain, and M. Akhtaruzzaman, *Solar photovoltaic technologies: From inception toward the most reliable energy resource,* in *Encyclopedia of Sustainable Technologies*, edited by M. A. Abraham (Elsevier, Oxford, 2017) pp. 11–26, doi:10.1016/B978-0-12-409548-9.10092-2.

[10] M. A. Green, *Photovoltaics: coming of age,* in *Photovoltaic Specialists Conference, 1990., Conference Record of the Twenty First IEEE* (IEEE, 1990) pp. 1–8, doi:10.1109/PVSC.1990.111582.

[11] W. W. Simon Phillips, *Photovoltaics report 2016,* https://www.ise.fraunhofer.de/content/dam/ise/de/documents/publications/studies/Photovoltaics-Report.pdf (2017), [Accessed on: 2017-11-07].

[12] S. B. Christiana Honsberg, *Detailed balance on efficiency,* http://www.pveducation.org/pvcdrom/detailed-balance (2017), accessed on 2017-09-12.

[13] F. T. Si, O. Isabella, H. Tan, and M. Zeman, *Quadruple-junction thin-film silicon solar cells using four different absorber materials,* Solar RRL **1** (2017), doi:10.1002/solr.201700036.

[14] H. Tan, A. Furlan, W. Li, K. Arapov, R. Santbergen, M. M. Wienk, M. Zeman, A. H. M. Smets, and R. A. J. Janssen, *Highly efficient hybrid polymer and amorphous silicon multi-junction solar cells with effective optical management,* Advanced Materials **28**, 2170 (2016), doi:10.1002/adma.201504483.

[15] D. Y. Kim, E. Guijt, F. Si, R. Santbergen, J. Holovský, O. Isabella, R. A. van Swaaij, and M. Zeman, *Fabrication of double- and triple-junction solar cells with hydrogenated amorphous silicon oxide (a-siox:h) top cell,* Solar Energy Materials and Solar Cells **141**, 148 (2015), doi:https://doi.org/10.1016/j.solmat.2015.05.033.

[16] D. Subramanyam, *Rvce unit 2,* https://rvcethinfilms.wordpress.com/2016/08/09/unit-2/ (2016), accessed on 2017-08-27.

[17] K. Seshan, *Handbook of Thin Film Deposition Processes and Techniques*, 2nd ed. (Noyes Publications, 2002).

[18] J. S. Sanjeev Kumar Gupta and J. Akhtar, *Physics and Technology of Silicon Carbide Devices* (INTECH, 2013) Chap. 8, Materials and Processing for Gate Dielectrics on Silicon Carbide (SiC) Surface, doi:10.5772/52553.

[19] JA. Wollam Co., *Polarized light,* https://www.jawoollam.com/resources/ellipsometry-tutorial/polarized-light (2017), accessed on 2017-09-04.

[20] M. A. Green, *Self-consistent optical parameters of intrinsic silicon at 300k including temperature coefficients,* Solar Energy Materials and Solar Cells **92**, 1305 (2008), doi:10.1016/j.solmat.2008.06.009.

[21] B. J. Horn, *Extraterrestrial irradiance,* http://bxhorn.com/extraterrestrial-irradiance/ (2017), accessed on 2017-18-11.

[22] S. B. Christiana Honsberg, *Standard solar spectra,* http://www.pveducation.org/pvcdrom/appendices/standard-solar-spectra (2017), accessed on 2017-08-29.

[23] Wacom Electric Co., LTD, *Super solar simulator, continuous type, two lamps system brochure of wxs-156s,* http://www.wacom-ele.co.jp/en/catalog/index.html (2017), accessed on 2017-08-30.

[24] Alternative Energy Tutorials, *Solar cell i-v characteristic,* http://www.alternative-energy-tutorials.com/energy-articles/solar-cell-i-v-characteristic.html (2017), accessed on 2017-08-31.

[25] M. Konagai and K. Takahashi, *Graded-band-gap p ga1- x al x as-n gaas heterojunction solar cells,* Journal of Applied Physics **46**, 3542 (1975), doi:10.1063/1.322083.

[26] R. Arya, A. Catalano, and R. Oswald, *Amorphous silicon p-i-n solar cells with graded interface,* Applied Physics Letters **49**, 1089 (1986), doi:10.1063/1.97430.

[27] S. Guha, J. Yang, A. Pawlikiewicz, T. Glatfelter, R. Ross, and S. Ovshinsky, *Band-gap profiling for improving the efficiency of amorphous silicon alloy solar cells,* Applied Physics Letters **54**, 2330 (1989), doi:10.1063/1.101118.

[28] B. Pieters, M. Zeman, R. Van Swaaij, and W. Metselaar, *Optimization of a-sige: H solar cells with graded intrinsic layers using integrated optical and electrical modeling,* Thin Solid Films **451**, 294 (2004), doi:10.1016/S0022-3093(01)01080-8.

[29] R. J. Zambrano, F. Rubinelli, J. Rath, and R. Schropp, *Improvement in the spectral response at long wavelength of a-sige: H solar cells by exponential band gap design of the i-layer,* Journal of non-crystalline solids **299**, 1131 (2002), doi:10.1016/S0022-3093(01)01080-8.

[30] T. Krajangsang, S. Inthisang, A. Dousse, A. Moollakorn, A. Hongsingthong, S. Kittisontirak, P. Chinnavornrungsee, A. Limmanee, J. Sritharathikhun, and K. Sriprapha, *Band gap profiles of intrinsic amorphous silicon germanium films and their application to amorphous silicon germanium heterojunction solar cells,* Optical Materials **51**, 245 (2016), doi:10.1016/j.optmat.2015.11.012.

[31] European Comission, *Europe 2020 indicators - climate change and energy,* http://ec.europa.eu/eurostat/statistics-explained/index.php/Europe_2020_indicators_-_climate_change_and_energy (2017), [Accessed on: 2017-10-17].

[32] European Comission, *People in the eu – population projections,* http://ec.europa.eu/eurostat/statistics-explained/index.php/People_in_the_EU_%E2%80%93_population_projections (2015), [Accessed on: 2017-10-17].

[33] R. C. John Hawksworth, Hannah Audino, *The world in 2050,* https://www.pwc.com/gx/en/issues/economy/the-world-in-2050.html (2017), [Accessed on: 2017-17-10].

[34] International Energy Agency (IEA), *Key World Energy Trends excerpt from World Energy Balances 2016*, Tech. Rep. (International Energy Agency, 2016).

[35] IEA, *World Energy Outlook 2016*, Tech. Rep. (International Energy Agency, 2016).

[36] British Petroleum BP, *BP Statistical Review of World Energy June 2017*, Tech. Rep. (British Petroleum BP, 2017).

[37] C. Winzer, *Conceptualizing energy security,* Energy policy **46**, 36 (2012), doi:10.1016/j.enpol.2012.02.067.

[38] M. A. Botello, *Pemex, cronologia, expropiacion y estadisticas,* http://www.mexicomaxico.org/Voto/pemex.htm (2017), [Accessed on: 2017-10-19].

[39] M. A. Botello, *Las crisis economicas en mexico, 1929-2012,* http://mexicomaxico.org/Voto/CrisisMex.htm (2017), [Accessed on: 2017-10-19].

[40] International Energy Agency IEA, *Costa rica: Electricity and heat for 2015,* https://www.iea.org/statistics/statisticssearch/report/?country=COSTARICA&product=electricityandheat&year=2015 (2015), [Accessed on: 2017-10-25].

[41] D. E. Agency, *Energy Statistics 2015*, Tech. Rep. (Danish Ministry of Energy, Utilities and Climate, 2017).

[42] B. Burger, *Power generation in germany – assessment of 2016,* https://www.energy-charts.de/downloads.htm (2017), [Accessed on: 2017-10-25].

[43] J. Lelieveld, J. Evans, M. Fnais, D. Giannadaki, and A. Pozzer, *The contribution of outdoor air pollution sources to premature mortality on a global scale,* Nature **525**, 367 (2015), doi:10.1038/nature15371.

[44] National Aeronautics and Space Agency (NASA), *Vital signs - carbon dioxide,* https://climate.nasa.gov/vital-signs/carbon-dioxide/ (2017), [Accessed on: 2017-10-18].

[45] Ed Dlugokencky and Pieter Tans, *Trends in atmospheric carbon dioxide - global,* https://www.esrl.noaa.gov/gmd/ccgg/trends/global.html (2017), [Accessed on: 2017-10-18].

[46] J. L. Powell, *The consensus on anthropogenic global warming matters,* Bulletin of Science, Technology & Society **36**, 157 (2016), doi:10.1177/0270467617707079.

[47] Intergovernmental Panel on Climate Change (IPCC), *Climate Change 2014: Synthesis Report. Contribution of Working Groups I, II and III to the Fifth Assessment Report of the Intergovernmental Panel on Climate Change*, Tech. Rep. (IPCC Core Writing Team, R.K. Pachauri and L.A. Meyer (eds.), 2014).

[48] European Commission, *Intended Nationally Determined Contribution of the EU and its Member States*, Tech. Rep. (European Commission, 2015).

[49] European Commission, *Communication from the European Parliament and the Council Energy Efficiency and its contribution to energy security and the 2030 Framework for climate and energy policy*, Tech. Rep. (European Comission, 2014).

[50] Climate Focus, *The paris agreement: Summary,* Climate Focus Client Brief on the Paris Agreement III. Retrieved March **31**, 2017 (2015).

[51] B. Stephan, S. Schurig, and A. Leidreiter, *What place for renewables in the indcs?* https://www.worldfuturecouncil.org/inc/uploads/2016/03/WFC_2016_What_Place_for_Renewables_in_the_INDCs.pdf (2016), [Accessed on: 2017-08-10].

[52] Global Wind Energy Council, *Global Wind Statistics 2016*, Tech. Rep. (Global Wind Energy Council, 2017).

[53] M. Djordjevic, *India's renewable energy capacity reaches 57.472 gw,* https://www.pv-magazine.com/2017/06/12/indias-renewable-energy-capacity-reaches-57472-gw/ (2016), [Accessed on: 2017-08-10].

[54] U.S. Energy Information Administration (EIA), *Table 4.3. existing capacity by energy source, 2015 (megawatts),* https://www.eia.gov/electricity/annual/html/epa_04_03.html (2015), [Accessed on: 2017-09-01].

[55] R. Bertani, *Geothermal power generation in the world 2010–2014 update report,* Geothermics **60**, 31 (2016), doi:10.1016/j.geothermics.2011.10.001.

[56] W.-D. Huang and Y. P. Zhang, *Energy efficiency analysis: biomass-to-wheel efficiency related with biofuels production, fuel distribution, and powertrain systems,* PLoS One **6**, e22113 (2011), doi:10.1371/journal.pone.0022113.

[57] A. H. Smets, K. Jäger, O. Isabella, R. A. van Swaaij, and M. Zeman, *Solar Energy: The physics and engineering of photovoltaic conversion, technologies and systems* (UIT Cambridge Limited, 2016).

[58] E. K. K. Samar, *Timeline and Future of Solar Cells*, Magazine on Renewable Energy Akshay Urja (Government of India Ministry of New and Renewable Energy, 2016).

[59] A. Einstein, *Concerning an heuristic point of view toward the emission and transformation of light,* Annalen der Physik , 132 (1905), translation into English by American Journal of Physics, v. 33, n. 5, May 1965.

[60] A. Luque and S. Hegedus, *Handbook of photovoltaic science and engineering* (John Wiley & Sons, 2011).

[61] J. J. Loferski, *Theoretical considerations governing the choice of the optimum semiconductor for photovoltaic solar energy conversion,* Journal of Applied Physics **27**, 777 (1956), doi:10.1016/B978-0-12-409548-9.10092-2.

[62] W. Shockley and H. J. Queisser, *Detailed balance limit of efficiency of p-n junction solar cells,* Journal of applied physics **32**, 510 (1961), doi:10.1063/1.1736034.

[63] D. Cusano, *Cdte solar cells and photovoltaic heterojunctions in ii-vi compounds,* Solid State Electronics **6**, 217 (1963), doi:10.1016/0038-1101(63)90078-9.

[64] S. Wagner, J. Shay, and H. Kasper, *The p-cuinse2/n-cds heterodiode: photovoltaic detector, solar cell and light emitting diode,* Le Journal de Physique Colloques **36**, C3 (1975), doi:10.1051/jphyscol:1975319.

[65] D. E. Carlson and C. R. Wronski, *Amorphous silicon solar cell,* Applied Physics Letters **28**, 671 (1976), doi:10.1063/1.88617.

[66] J. S. Lacerda and J. C. van den Bergh, *Diversity in solar photovoltaic energy: Implications for innovation and policy,* Renewable and Sustainable Energy Reviews **54**, 331 (2016), doi:10.1016/j.rser.2015.10.032.

[67] K. Yoshikawa, H. Kawasaki, W. Yoshida, T. Irie, K. Konishi, K. Nakano, T. Uto, D. Adachi, M. Kanematsu, H. Uzu, *et al.*, *Silicon heterojunction solar cell with interdigitated back contacts for a photoconversion efficiency over 26%,* Nature Energy **2**, 17032 (2017), doi:10.1038/nenergy.2017.32.

[68] A. McEvoy, T. Markvart, L. Castañer, and K. Soteris A., *Practical handbook of photovoltaics: fundamentals and applications*, 3rd ed. (Elsevier, 2017).

[69] L. S. Mattos, S. R. Scully, M. Syfu, E. Olson, L. Yang, C. Ling, B. M. Kayes, and G. He, *New module efficiency record: 23.5% under 1-sun illumination using thin-film single-junction gaas solar cells,* in *2012 38th IEEE Photovoltaic Specialists Conference* (2012) pp. 003187–003190, doi:10.1109/PVSC.2012.6318255.

[70] M. A. Green, Y. Hishikawa, W. Warta, E. D. Dunlop, D. H. Levi, J. Hohl-Ebinger, and A. W. Ho-Baillie, *Solar cell efficiency tables (version 50),* Progress in Photovoltaics: Research and Applications **25**, 668 (2017), doi:10.1016/S1369-7021(07)70278-X.

[71] Solar Frontier's Atsugi Research Centre (ARC) and the National Research and Development Agency's New Energy and Industrial Technology Development Organization (NEDO), *Solar frontier's cis thin-film submodule achieves highest efficiency world record of 19.2%,* http://www.solar-frontier.com/eng/news/2017/0227_press.html (2017), [Accessed on: 2017-12-10].

[72] First Solar, Inc., *First solar achieves world record 18.6% thin film module conversion efficiency,* http://investor.firstsolar.com/news-releases/news-release-details/first-solar-achieves-world-record-186-thin-film-module (2015), [Accessed on: 2017-12-10].

[73] J. Cashmore, M. Apolloni, A. Braga, O. Caglar, V. Cervetto, Y. Fenner, S. Goldbach-Aschemann, C. Goury, J. Hötzel, T. Iwahashi, J. Kalas, M. Kitamura, M. Klindworth, M. Kupich, G.-F. Leu, J. Lin, M.-H. Lindic, P. Losio, T. Mates, D. Matsunaga, B. Mereu, X.-V. Nguyen, I. Psimoulis, S. Ristau, T. Roschek, A. Salabas, E. Salabas, and I. Sinicco, *Improved conversion efficiencies of thin-film silicon tandem (micromorph™) photovoltaic modules,* Solar Energy Materials and Solar Cells **144**, 84 (2016), doi:10.1016/j.solmat.2015.08.022.

[74] National Renewable Energy Laboratory (NREL), *Research cell record efficiency chart,* https://www.nrel.gov/pv/assets/images/efficiency-chart.png (2017), [Accessed on: 2017-12-10].

[75] S. Rühle, *Tabulated values of the shockley–queisser limit for single junction solar cells,* Solar Energy **130**, 139 (2016), doi:10.1016/j.solener.2016.02.015.

[76] T. Tiedje, E. Yablonovitch, G. D. Cody, and B. G. Brooks, *Limiting efficiency of silicon solar cells,* IEEE Transactions on electron devices **31**, 711 (1984), doi:10.1109/T-ED.1984.21594.

[77] X. Huang, J. Wang, D. Yu, S. Ye, Q. Zhang, and X. Sun, *Spectral conversion for solar cell efficiency enhancement using yvo4: Bi3+, ln3+ (ln= dy, er, ho, eu, sm, and yb) phosphors,* Journal of Applied Physics **109**, 113526 (2011), doi:10.1063/1.3592889.

[78] Y. Shang, S. Hao, C. Yang, and G. Chen, *Enhancing solar cell efficiency using photon upconversion materials,* Nanomaterials **5**, 1782 (2015), doi:10.3390/nano5041782.

[79] A. Mojiri, R. Taylor, E. Thomsen, and G. Rosengarten, *Spectral beam splitting for efficient conversion of solar energy—a review,* Renewable and Sustainable Energy Reviews **28**, 654 (2013), doi:10.1016/j.rser.2013.08.026.

[80] A. Lenert, D. M. Bierman, Y. Nam, W. R. Chan, I. Celanović, M. Soljačić, and E. N. Wang, *A nanophotonic solar thermophotovoltaic device,* Nature nanotechnology **9**, 126 (2014), doi:10.1038/nnano.2013.286.

[81] A. De Vos, *Detailed balance limit of the efficiency of tandem solar cells,* Journal of Physics D: Applied Physics **13**, 839 (1980), doi:10.1088/0022-3727/13/5/018/meta.

[82] F. T. Si, O. Isabella, and M. Zeman, *Too many junctions? a case study of multijunction thin-film silicon solar cells,* Advanced Sustainable Systems **1** (2017), doi:10.1002/adsu.201700077.

[83] D. Y. Kim, E. Guijt, R. A. van Swaaij, and M. Zeman, *Hydrogenated amorphous silicon oxide (a-sio x: H) single junction solar cell with 8.8% initial efficiency by reducing parasitic absorptions,* Journal of Applied Physics **121**, 133103 (2017), doi:10.1063/1.4979690.

[84] P. R, R. S, M. , and M. , *Review of physical vapour deposition (pvd) techniques,* Proceedings of the International Conference on "Sustainable Manufacturing", At Coimbatore Institute of Technology, Coimbatore (2013), doi:10.13140/RG.2.1.5063.4964.

[85] J. J. et al., *Ellipsometry*, Tech. Rep. (AALBORG UNIVERSITY, Institute of Physics and Nanotechnology, 2004).

[86] G. Benno and K. Joachim, *Optical properties of thin semiconductor films,* October, 31st (2003).

[87] H. H. Ku, *Notes on the use of propagation of error formulas,* Journal of Research of the National Bureau of Standards **70** (1966).

[88] D. Y. Kim, E. Guijt, R. A. C. M. M. van Swaaij, and M. Zeman, *Development of a-siox:h solar cells with very high voc × ff product,* Progress in Photovoltaics: Research and Applications **23**, 671 (2015), doi:10.1002/pip.2581.

[89] E. J. Guijt, *Application of intrinsic amorphous silicon oxide in multi-junction solar cells*, Master's thesis, Delft University of Technology, Delft, Netherlands (2014).

[90] A. H. Pawlikiewicz and S. Guha, *Numerical modeling of an amorphous-silicon-based pin solar cell,* IEEE Transactions on Electron Devices **37**, 403 (1990), doi:10.1109/16.46374.

[91] R. van Swaaij, M. Zeman, S. Arnoult, and J. Metselaar, *Performance dependence on grading width of a-sige: H component solar cells,* in *Photovoltaic Specialists Conference, 2000. Conference Record of the Twenty-Eighth IEEE* (IEEE, 2000) pp. 869–872, doi:10.1109/PVSC.2000.916021.

[92] N. Bernhard, G. Bauer, and W. Bloss, *Bandgap engineering of amorphous semiconductors for solar cell applications,* Progress in Photovoltaics: Research and Applications **3**, 149 (1995), doi:10.1002/pip.4670030301.

[93] D. Lundszien, F. Finger, and H. Wagner, *A-si: H buffer in a-sige: H solar cells,* Solar energy materials and solar cells **74**, 365 (2002), doi:10.1016/S0927-0248(02)00096-X.

[94] D. Lundszien, F. Finger, and H. Wagner, *Band-gap profiling in amorphous silicon–germanium solar cells,* Applied physics letters **80**, 1655 (2002), doi:10.1063/1.1456548.

[95] T. Dullweber, U. Rau, H. Schock, *et al.*, *A new approach to high-efficiency solar cells by band gap grading in cu (in, ga) se 2 chalcopyrite semiconductors,* Solar Energy Materials and Solar Cells **67**, 145 (2001), doi:10.1016/S0927-0248(00)00274-9.

[96] M. A. Contreras, J. Tuttle, A. Gabor, A. Tennant, K. Ramanathan, S. Asher, A. Franz, J. Keane, L. Wang, and R. Noufi, *High efficiency graded bandgap thin-film polycrystalline cu (in, ga) se2-based solar cells,* Solar energy materials and solar cells **41**, 231 (1996), doi:10.1016/0927-0248(95)00145-X.

[97] K. Decock, J. Lauwaert, and M. Burgelman, *Characterization of graded cigs solar cells,* Energy Procedia **2**, 49 (2010).

[98] S. Inthisang, K. Sriprapha, S. Miyajima, A. Yamada, and M. Konagai, *Hydrogenated amorphous silicon oxide solar cells fabricated near the phase transition between amorphous and microcrystalline structures,* Japanese journal of applied physics **48**, 122402 (2009), doi:10.1143/JJAP.48.122402.